UNIVERSITEIT UTRECHT

Neutral Mesons & Direct Photon Flow

by

Mike Sas

A thesis submitted in partial fulfillment for the
degree of Master of Science

in the
Faculty of Science
Subatomic Physics

August 2016

"Nobody ever figures out what life is all about, and it doesn't matter. Explore the world. Nearly everything is really interesting if you go into it deeply enough."

Richard Feynman

UNIVERSITEIT UTRECHT

Abstract

Faculty of Science
Subatomic Physics

Master of Science

by Mike Sas

Ultra-relativistic collisions of protons and heavy-ions reveal the structure of matter at the smallest scales and help us to complete the picture of the universe. Transverse momentum dependent particle production spectra are expected to change for pp, p-A and A-A collisions because of the change in energy densities and temperature of the created system. The modification with respect to pp collisions is quantified by the nuclear modification factor that is able to give insight into low and high p_T particle production mechanisms. In A-A collisions at LHC energies it is expected that a Quark Gluon Plasma is formed. This strongly interacting state of matter can be studied by measuring the elliptic flow of direct photons. Direct photons, i.e. all photons excluding the ones from hadronic decays, are produced during every stage of the heavy-ion collision. Direct photon flow is measured by subtracting the contribution of decay photon flow from the measured inclusive photon flow via the double ratio R_γ , which defines the excess of direct photons over decay photons. This thesis presents the results of two analyses using the data recorded with the ALICE detector at the LHC.

The neutral meson measurement is done using the Electro-Magnetic Calorimeter of the ALICE detector in p-Pb collisions at $\sqrt{s_{NN}} = 5.023$ TeV. The invariant cross sections of the π^0 and η is extracted using the invariant mass method. In addition, the η/π^0 ratio and the neutral pion R_{p-Pb} is presented where the latter is compared to state of the art theoretical predictions.

The direct photon flow measurement is performed using the photon conversion method in ALICE in Pb-Pb collisions at $\sqrt{s_{NN}} = 2.76$ TeV. The purity of the inclusive photon sample has been studied to identify the conversion photon background sources. In addition, a method has been developed to correct the inclusive photon flow for background flow. The direct photon flow is measured for collision centralities 0-20%, 20-40% and 40-80%. The results show a slight tension with being consistent with zero.

Contents

Chapter 1

Introduction

1.1 Quantum Chromodynamics

Nature at the smallest scales is described by the standard model of particle physics, a quantum field theory based on symmetries. It formulates that the universe is made of fundamental particles governed by four fundamental forces. One of the fundamental forces, the strong force, is responsible for the existence of hadrons such as pions, protons and kaons. The constituents of hadrons are quarks, which are confined into hadrons via the exchange of gluons, the force carrier of the strong force. The interactions between quarks and gluons can be described by the theory of Quantum Chromodynamics(QCD).

QCD is invariant under local SU(3) phase transformations,

$$\psi(x) \rightarrow \psi'(x) = \left[ig_s\alpha(x)\cdot\hat{\mathbf{T}}\right]\psi(x), \tag{1.1}$$

where g_s is the strength of the strong interaction and $\alpha(x)$ are arbitrary functions of space-time. $\hat{\mathbf{T}} = \{T^a\}$ are the eight generators of the SU(3) symmetry group and are represented by 3×3 matrices. The three additional degrees of freedom are referred to as the color charges red, blue and green. Local gauge invariance is obtained by introducing eight gluon fields $G^a_\mu(x)$, with $a = 1, ..., 8$, corresponding to the generators of the SU(3) symmetry group. The Dirac equation

$$i\gamma^\mu\left[\partial_\mu + ig_sG^a_\mu T^a\right]\psi - m\psi = 0 \tag{1.2}$$

is invariant under local SU(3) phase transformations if G^k_μ transforms as

$$G^k_\mu \rightarrow G^{k\ \prime}_\mu = G^k_\mu - \partial_\mu\alpha_k - g_sf_{ijk}\alpha_iG^j_\mu. \tag{1.3}$$

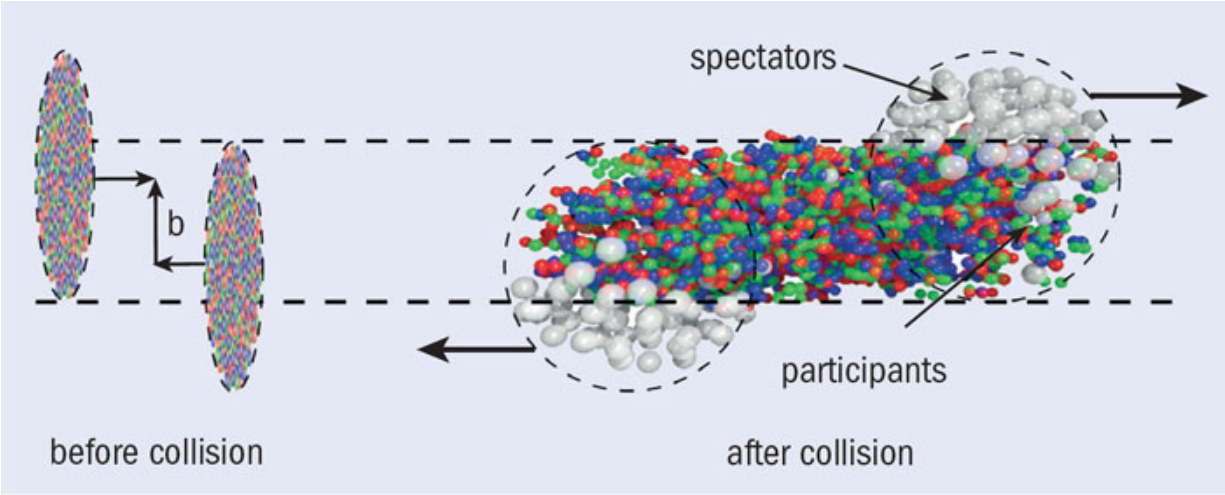

FIGURE 1.1: Overview of a collisions between two heavy-ions. Two impacting nuclei are displaced by an impact parameter b, creating participants and spectators of the collision.

f_{ijk} are the structure constants of the SU(3) group. One of the main features of this theory is that the generators of SU(3) do not commute. This makes QCD a non-Abelian gauge theory in which the gluon couples not only to quarks but also to itself. The gluon-gluon interactions add an infinite amount of loop diagrams, leading to anti-screening of color charge and an increasing strong coupling constant α_s for increasing resolution. The evolution of α_s as function of momentum transfer Q is

$$\alpha_s(Q^2) = \frac{12\pi}{(33 - 2N_f)ln(Q^2/\Lambda^2_{QCD})}, \tag{1.4}$$

where N_f is the number of quarks and Λ_{QCD} is the QCD energy scale parameter. It can be seen that α_s decreases for increasing Q^2. This means that for sufficiently high energies the theory can be treated perturbatively and the quarks are essentially free particles. This is known as *asymptotic freedom*. For low energies α_s becomes large and the quarks are confined in colorless objects. This is known as *confinement*.

For extremely high temperatures and energy densities, numerical solutions of Quantum Chromodynamics predict a state of hot dense matter where quarks and gluons are deconfined [1]. This state of matter is the so-called Quark Gluon Plasma (QGP). The phase transition at which the hadronic system dissolves is estimated to be at a temperature of $T_c \sim 200$MeV and an energy density of $\epsilon \sim 1$GeV/fm^3. A QGP is believed to be produced in ultra-relativistic heavy ion collision at the Super Proton Synchrotron (SPS), Relativistic Heavy Ion Collider (RHIC) and the Large Hadron Collider (LHC).

1.2 Heavy-ion collisions

Our picture of the universe, encapsulated in the standard model of particle physics, is continuously tested by collider experiments. Collisions between two heavy-ions are used to study the QCD sector under extreme

conditions. Compared to the more common pp collisions, central Pb-Pb collisions produce on average ∼200 times more particles. This is because the multiplicity scales with the atomic mass number A. Figure 1.1 shows a schematic picture of a heavy-ion collision. Heavy-ions are extended objects that are Lorentz contracted in longitudinal direction. Central collisions have a high number of participants and few spectators, increasing the energy density of the produced medium and final state multiplicity. Peripheral collisions have a lower number of participants and more spectators. The space-time evolution of the collision, as shown in figure 1.2, goes as follows:

- pre-equilibrium: $0 < \tau < \tau_0$
- QGP phase: $\tau_0 < \tau < \tau_m$
- mixed phase: $\tau_m < \tau < \tau_h$
- hadron gas: $\tau_h < \tau < \tau_f$
- freeze-out: $\tau > \tau_f$

The pre-equilibrium stage of the collision is dominated by hard processes of high momentum partons. Heavy quarks, jets and prompt photons are produced in this stage. Thermal equilibrium is reached at $\tau = \tau_0$ and this defines the formation time of the QGP. Thermal photons are emitted from the QGP. If the phase transition is first order, there is a mixed QGP and hadron gas phase, starting at $\tau = \tau_m$. When the temperature drops below the critical temperature T_c, the quarks are no longer deconfined and hadrons are formed out of the quark soup. The system can be described as a hadron gas, starting at $\tau = \tau_h$. Thermal photons are continued to be emitted in the hadron gas phase. The system continues to expand until the freeze-out happens at $\tau = \tau_f$. Hadrons now stop interacting with each other and the final state of the collision is reached.

1.3 Anisotropic flow

Heavy-ions experience length contraction when approaching the speed of light, making them Lorentz boosted "pancakes" in the laboratory frame. In the collisions of such ions the collision geometry is mostly defined by the impact parameter b, which is the distance between the two centers of the colliding nuclei. The impact parameter is a measure for the centrality of the collision, which is commonly estimated by the event multiplicity. For an impact parameter $b \approx 0$ the collision geometry becomes azimuthally symmetric, while for larger impact parameters it becomes azimuthally asymmetric, as shown in figure 1.3.

The spatial anisotropy of the system translates into a momentum anisotropy more commonly called flow. Measuring this observable gives insight into the physical properties of the QGP. Particle distributions as function of the azimuthal angle can be described by the Fourier expansion:

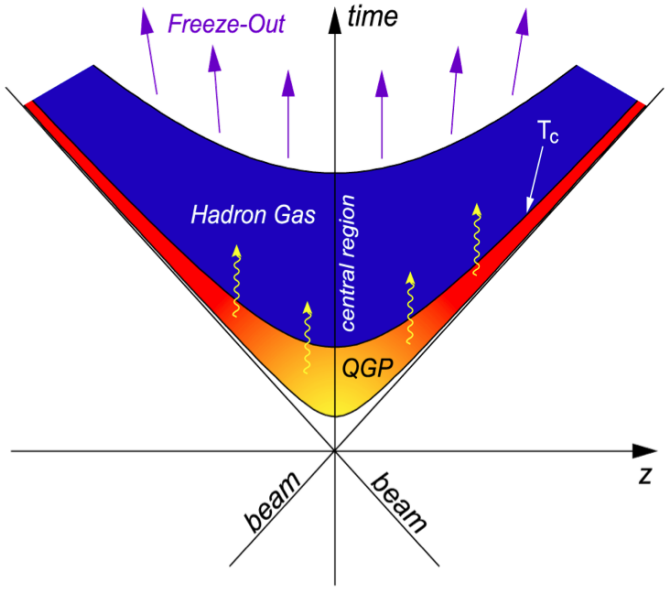

FIGURE 1.2: Space-time evolution of a heavy-ion collision. The primary interaction happens at time $\tau = 0$ after which the produced matter goes through various stages.

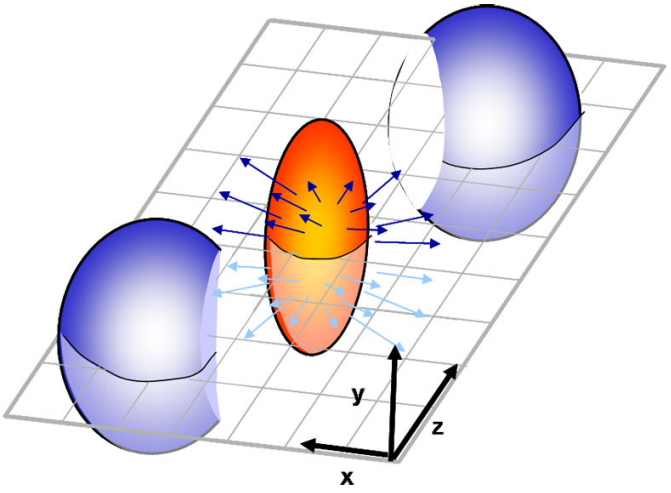

FIGURE 1.3: The collision geometry of a heavy-ion collision where the two nuclei are displaced, creating a azimuthally asymmetric medium.

$$E\frac{d^3N}{d^3p} = \frac{1}{2\pi}\frac{d^2N}{p_t dp_t dy}\left(1 + \sum_{n=1}^{\infty} 2v_n cos(n(\varphi - \Psi_R))\right), \tag{1.5}$$

where φ is the azimuthal angle of the particle and Ψ_R the angle of the reaction plane in the laboratory frame. The Fourier coefficients v_n are given by:

$$v_n = \langle cos(n(\varphi - \Psi_R))\rangle, \tag{1.6}$$

where $\langle ... \rangle$ denotes the average over particles and events. The fourier coefficients v_n are more commonly called radial flow(v_1), elliptic flow(v_2) and triangular flow(v_3).

1.4 Nuclear modification factor

Another way to study the properties of the predicted QGP is to measure the transverse momentum dependent particle production spectrum in Pb-Pb collisions and compare it to pp collisions. In this approach, the initial wave functions of the colliding nuclei are not taken into account. The measurements in p-Pb collisions are used to study cold nuclear matter effects, such as gluon saturation and dynamical shadowing, and help to disentangle the effects coming from the initial state of the collision. It is expected that the spectra in Pb-Pb collisions gets a modification with respect to the spectra in pp collisions. At low p_{T} there might be a modification which can not be fully explained by participant scaling. At higher p_{T} the main production mechanism of hadrons is through hard-scattering of quarks and gluons from jet fragmentation. If the jet happens to penetrate the QGP it loses energy, which results in spectra modifications at high p_{T} . This effect is known as "jet quenching". The modification compared to pp is quantified by the nuclear modification factor

$$R_{AA}(p_T) = \frac{d^2N/dp_T dy \mid_{AA}}{\langle T_{AA} \rangle \, d^2\sigma/dp_T dy \mid_{pp}}, \tag{1.7}$$

with the nuclear overlap function $\langle T_{AA} \rangle$ defined as

$$\langle T_{AA} \rangle = \frac{\langle N_{coll} \rangle}{\sigma_{inel}^{pp}}. \tag{1.8}$$

T_{AA} basically scales up the spectra of pp collisions to A-A collisions by the assumption that a A-A collisions are multiple pp collisions. A clear modification of the particle spectra in Pb-Pb with respect to p-Pb or pp collisions can hint the existence of hot QCD matter. The R_{AA} can be measured for charged and neutral particles. For R_{AA} measurement of a neutral mesons the π^0 is a good choice since it is abundant and experimentally easy to reconstruct via invariant mass methods using the $\pi^0 \to \gamma\gamma$ decay channel.

1.5 Direct photons

One way to study the properties of the QGP is by measuring direct photons. Direct photons, i.e. all photons excluding those from hadronic decays, are produced during every stage of the collision evolution. They can be categorized in two regimes governed by different production mechanisms, which to a large extent coincide with specific transverse momentum ranges [2]. Prompt photons are produced in hard scatterings of incoming partons, dominating the direct photon spectrum at higher transverse momenta ($p_{\mathrm{T}} > 4$ GeV/c). Thermal

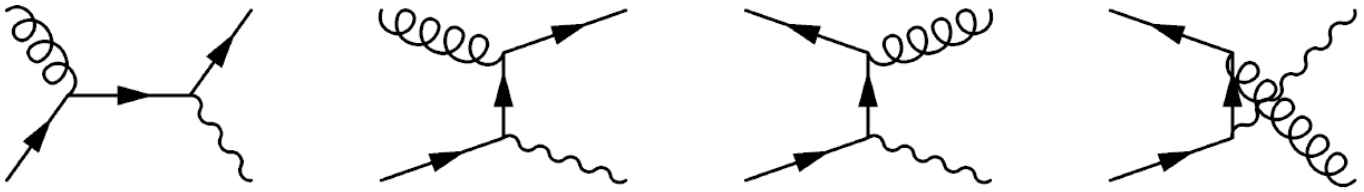

FIGURE 1.4: Leading order Feynman diagrams for direct photon production. The first two are s and u channel quark-gluon Compton scattering, respectively. The last two are t and u channel quark anti-quark annihilation, respectively.

photons are emitted during the hot QGP and hadron gas phases and dominate at lower transverse momenta ($p_{\mathrm{T}} < 4$ GeV/c). The yield of thermal direct photons is proportional to the temperature of the system via

$$E\frac{d^3N}{dp^3} \propto e^{-E_\gamma/T}. \tag{1.9}$$

Where T is an effective temperature. The fireball expands and cools down, emitting photons with decreasing energy which are increasingly blue shifted by the increasing expansion velocity of the QGP. Since photons interact only weakly with the strongly coupled medium they provide unique information of the produced system allowing one to deduce the initial temperature of the QGP from calculations. The leading order Feynman diagrams for direct photon production are shown in figure 1.4.

WA98 [3], PHENIX [4–6], STAR [7] and ALICE [8] measured the direct photon transverse momentum spectrum. The result from ALICE is shown in figure 1.5, for Pb-Pb collisions at $\sqrt{s_{NN}}$ = 2.76TeV in three collision centralities. An exponential fit for low p_{T} is used to fit the excess of direct photon yield to obtain an effective temperature of $T = 304 \pm 51$MeV for most central collisions. PHENIX and STAR both measure an excess of direct photons at low p_{T} and the tension between theory and experiment is stronger for PHENIX, as it reports a spectrum measurement much above the theory expectation.

A surprisingly large azimuthal anisotropy (a.k.a. elliptic flow) of direct photons is measured by PHENIX [9, 10] and ALICE [11] collaborations, comparable to that of hadrons. These observations suggest that the photon production occurs at later stages of the collision when the collective flow of the system is fully developed, while the temperature and, hence, the corresponding thermal photon rates are already reduced. It is a challenge for models to simultaneously describe the observed direct photon yields and azimuthal anisotropy at low p_{T} , which is referred to as "the direct photon puzzle" [12–23]. Figure 1.6 shows the elliptic flow coefficient $v_2^{\gamma,\mathrm{dir}}$ as function of transverse momentum, measured by the PHENIX collaboration and is compared to the hydrodynamics model prediction.

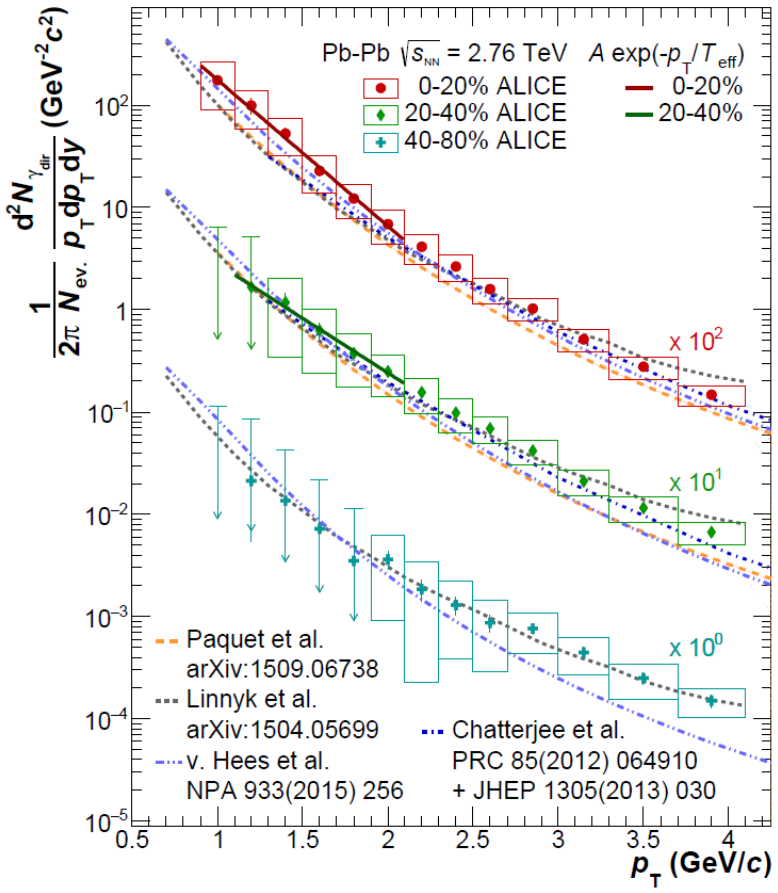

FIGURE 1.5: Yield of direct photons measured by ALICE.

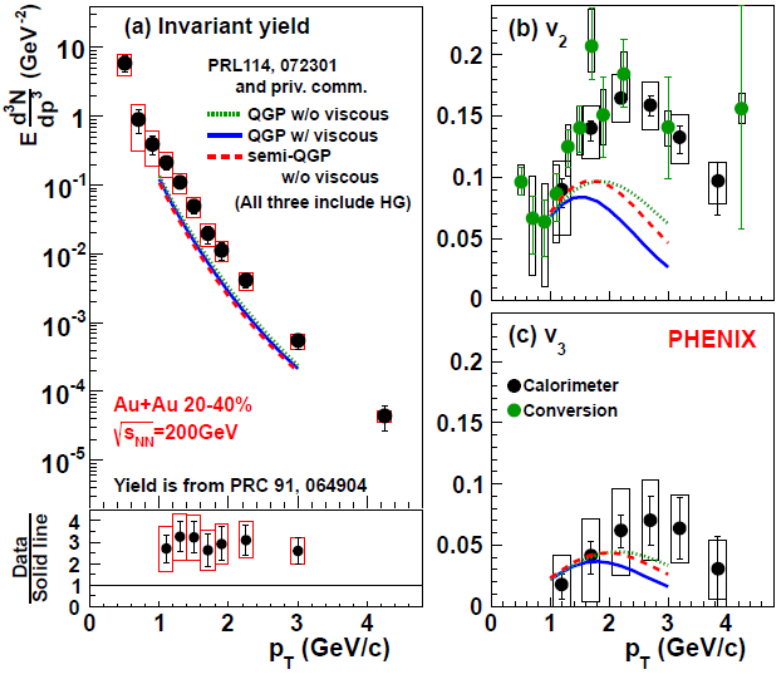

FIGURE 1.6: Yield and flow of direct photons measured by the PHENIX collaboration.

Chapter 2

The ALICE detector

The ALICE detector is located at interaction point 2 of the LHC at CERN and is optimized for studying heavy-ion(Pb-Pb) collisions. It is approximately 16 meters high, 16 meters wide, 26 meters long and weighs about 10.000 tons. Many detector systems complement each other to identify all particles produced in heavy-ion collisions by measuring their charge, momentum and mass. Two of the main detector systems are the Inner Tracker System and Time Projection Chamber, which reconstructs the trajectory of the particle and adds information on the identity of the particle. Calorimeters are used to absorb the total energy of an impending particle, such as photons and electrons. Figure 2.1 presents an overview of the detector. The sub-systems relevant to the analyses presented in this thesis will be described in more detail.

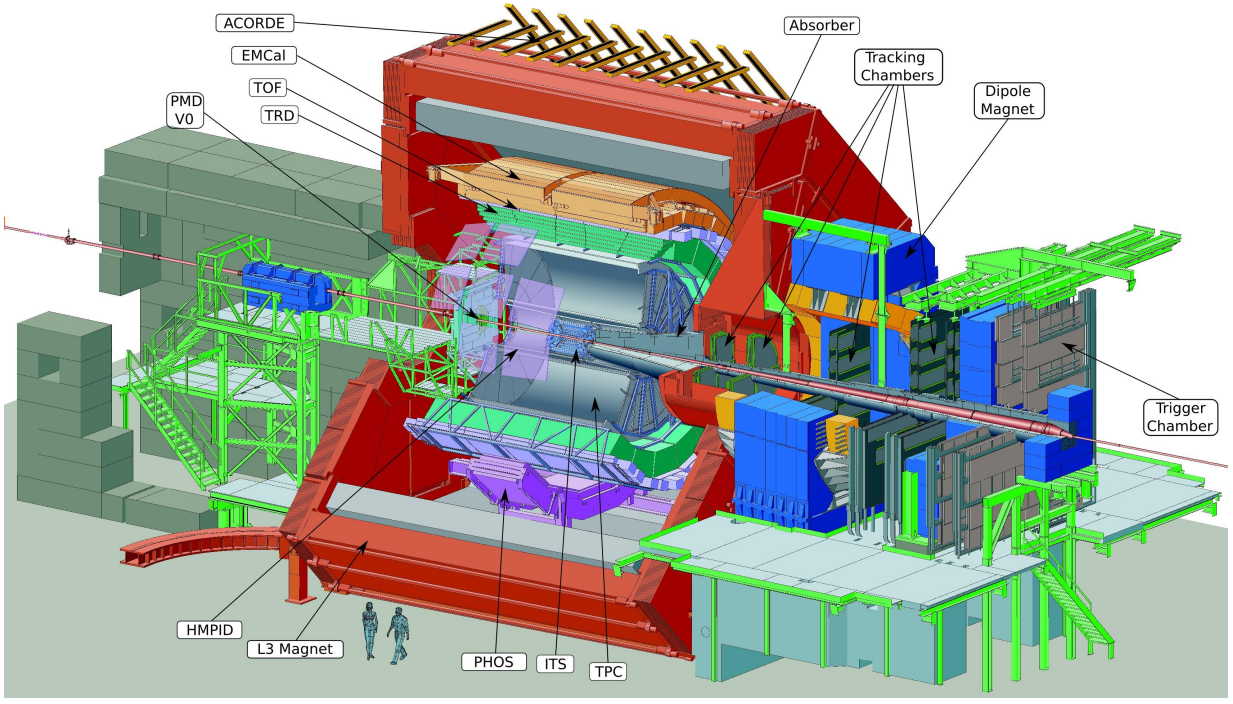

FIGURE 2.1: The ALICE detector.

2.1 Detector systems

2.1.1 Inner Tracking System

The inner most detector system of the ALICE detector, the ITS, is a six-layer silicon detector positioned close to the collision point(figure 2.2). Its main purpose is to provide charged particle track information by measuring hits in silicon sensors. The inner two layers consists of Silicon Pixel Detectors (SPD). The next two layers are Silicon Drift Detectors (SDD) and the outer two layers are Silicon Strip Detectors (SSD). Besides the technology, the main difference in the different layers is the tracking precision. The SPD, having a pseudorapidity coverage of $|\eta| < 1.95$, is able to achieve a track impact parameter resolution better than 50μm for $p_{\mathrm{T}} > 1.3$GeV/c. It can cope with charged particle multiplicities of ~ 8000 per unit rapidity due to its high granularity and resolution.

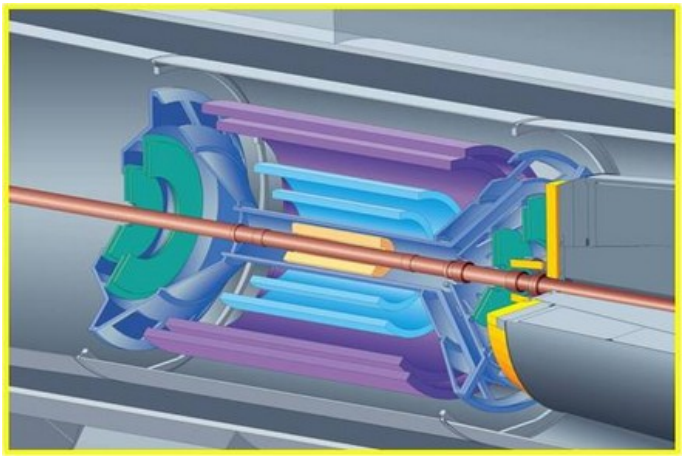

FIGURE 2.2: The ALICE Inner Tracking System(ITS). It consists of six layers of silicon detectors.

2.1.2 Time Projection Chamber

The TPC(figure 2.3) is a cylindrical drift detector covering the full azimuthal angle with a pseudorapidity range of $|\eta| < 0.9$. Till the end of 2010 it was filled with a gas mixture of Ne-CO_2-N_2 (90-10-5) after which the N_2 got removed. It provides particle identification using the specific energy loss (dE/dx). Charged particles traversing the TPC lose energy by ionising the gas. The liberated electrons drift to the end plates by an applied electric field of 100kV. The hit location in the end plates is combined with the drift time to reconstruct the three dimensional tracks. Photons converting to electron positron pairs when interacting with the detector material can be reconstructed with the TPC and can be reconstructed down to a transverse momentum of 50 MeV/c.

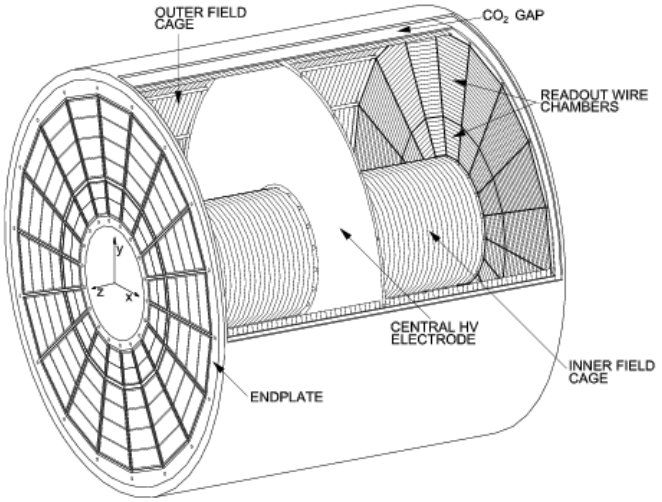

FIGURE 2.3: The ALICE Time Projection Chamber(TPC).

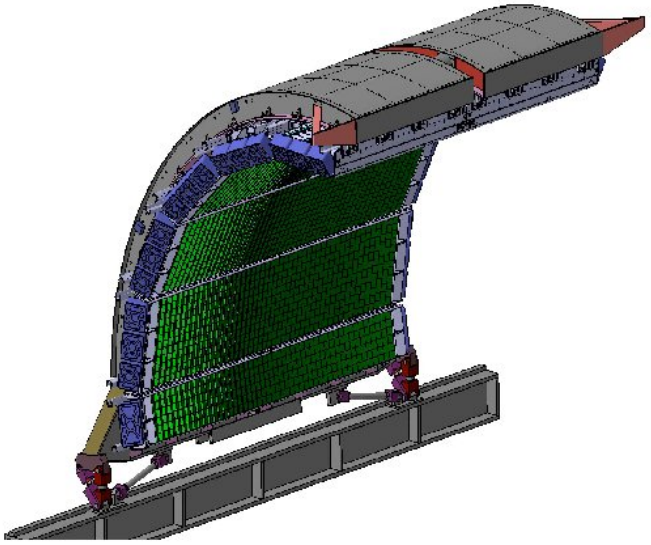

FIGURE 2.4: The ALICE Electro-Magnetic Calorimeter(EMCal).

2.1.3 Electromagnetic Calorimeter

The EMCal is an electromagnetic calorimeter consisting of stacks of alternating layers of absorber and scintillating material penetrated by wavelength shifting fibers. Each of these stacks are referred to as a cell. The EMCal is made up of more than $12,000$ cells grouped in arrays of super modules all pointing to the beam axis. The coverage of the EMCal is $1.4 < \phi < 3.1$ in azimuthal angle with a pseudorapidity range of $|\eta| < 0.7$. Particles produce an electromagnetic shower in the EMCal, depositing energy in multiple cells which forms a cluster. The particles that develop showers in the EMCal are reconstructed by using clusterizer algorithms, making it suitable for photon reconstruction in a wide transverse momentum range.

System	$\sqrt{s_{NN}}(TeV)$	**Data set**	**Centrality**	$\mathbf{N}_{events}$
Pb-Pb	2.76	LHC10h	0-20%	$3.29 \cdot 10^6$
			20-40%	$3.30 \cdot 10^6$
			40-80%	$6.60 \cdot 10^6$
Pb-Pb	2.76	LHC13d2	0-20%	$1.17 \cdot 10^6$
			20-40%	$6.28 \cdot 10^5$
			40-80%	$4.16 \cdot 10^6$
p-Pb	5.023	LHC13b+c	0-100%	$8.78 \cdot 10^7$
p-Pb	5.023	LHC13b2_efix	0-100%	$1.06 \cdot 10^8$
p-Pb	5.023	LHC13e7	0-100%	$4.24 \cdot 10^7$

TABLE 2.1

2.2 Data sets

In 2010 ALICE recorded Pb-Pb data during the heavy-ion run at a collision energy of $\sqrt{s_{NN}}$ = 2.76TeV. In January and February 2013 data was taken for a p-Pb run at a collision energy of $\sqrt{s_{NN}}$ = 5.02TeV. The analyses presented in this thesis uses the Pb-Pb data set LHC10h and the p-Pb datasets LHC13b and LHC13c, each with anchored Monte Carlo(MC) data sets. The MC data sets are produced by the event generators HIJING and DMPJET, which simulate pp, p-Pb and Pb-Pb collisions. The particles in each event are propagated through the ALICE detector with GEANT3 to simulate the full detector response.

In data, only events that pass the offline event selection are accepted. Events that are labelled as "non-physical" are rejected, which are for example calibration events and noise or beam-gas interactions. The event selection uses the standard *Physics Selection*(PS) with the offline trigger kINT7, which requires a signal in the V0A and V0C detectors. Assuming a monotonous relation between impact parameter b and V0 signals, intervals of V0 signal correspond to percentages of the cross section. This is defined as the centrality of the collision and is measured using the sum of the amplitudes in the V0-A and V0-C scintillator detectors. where V0-A covers $2.8 < \eta < 5.1$ and V0-C covers $-3.7 < \eta < -1.7$ in pseudorapidity range. The direct photon analysis is done for three collision centrality classes; 0-20%, 20-40% and 40-80%. The number of events that passed event selection for each of the data sets are listed in table 2.1.

Chapter 3

Photon detection in ALICE

The ALICE detector can reconstruct photons using many different detection techniques. Two main techniques are the Photon Conversion Method(PCM) and the calorimetric method. Photons in PCM can be reconstructed with $p_{\mathrm{T}} > 50$ MeV, but suffers from the low photon conversion probability. The calorimetric method has its strength at higher energies and can reconstruct photons with $E > 500$ MeV while having high reconstruction efficiency and acceptance. These two methods will be explained in detail.

3.1 Photon Conversion Method

Photons can convert into electron positron pairs when interacting with material of the detector. This means that a converted photon can be reconstructed by using the track information of the electron positron pair. In ALICE this is done with the Inner Tracking System (ITS) and the Time Projection Chamber (TPC).

3.1.1 Photon reconstruction

With the Photon Conversion Method(PCM), the photon is reconstructed using the conversion point and track information of the electron positron pair. The signal selection is split into three categories: track and V^0 selection, electron positron selection and photon selection.

3.1.1.1 Track and V^0 selection

In this analysis the V^0-finder "On-the-Fly" is used to obtain conversion photon candidates. The V^0-finder is a secondary vertex finder optimized to find vertices where two particles originate from a single point in space without a charged track coming in to the vertex. The selected V^0 have the requirement that the secondary tracks are opposite in charge and have a minimum transverse momentum of 50 MeV/c. In addition, the

Track & V0 cuts	
V0-finder	On-the-Fly
minimum track p_{T} cut	$p_{T,track} > 0.05$ GeV/c
Cut on $N_{\text{cluster TPC}}/N_{\text{findable clusters}}$	$> 60\%$
η-cut for tracks & V0	$\lvert\eta\rvert < 0.9$
Cut on R_{conv}	0 cm $< R_{\text{conv}} <$ 180 cm
Cut on Z_{conv}	$\lvert Z_{\text{conv}}\rvert <$ 240 cm

TABLE 3.1

secondary vertex(conversion point) is recalculated using the track information of the conversion daughters. The full list of cuts is given in table 3.1.

3.1.1.2 Electron positron selection

The selected V^0's can be any neutral particle decaying into two charged particles. To further select conversion photons the two daughter tracks need to match an electron positron pair. This is done using the dE/dx information of the TPC. As shown in figure 3.1, charged particles have a characteristic response depending on the type of particle and its momentum. This can thus be used to select electrons and positrons and reject background. The response for each particle species is fitted and defines the average response for a given transverse momentum. The electron selection is then based on the following quantity:

$$n\sigma_e = \frac{\frac{dE}{dx}\mid_{candidate} - \langle \frac{dE}{dx}\mid_{electron} \rangle}{\sigma_{\langle \frac{dE}{dx}|_{electron} \rangle}} \tag{3.1}$$

Where $\langle ... \rangle$ denotes the average response and is extracted from the fit. In short, $n\sigma_e$ is the number of standard deviations between the response of the electron candidate and the mean response of the electron for the given momentum. The mean response of each particle species can be well described by Bethe-Bloch parametrisations.

3.1.1.3 Photon selection

After the track, V^0 and electron positron selection we have candidates that most likely decay as $V^0 \rightarrow e^+e^-$. To further improve the purity of the photon sample a set of topological cuts is applied. Figure 3.2 shows the V^0 topology with the parameter definitions. The three-vector sum of the momentum of the positive and negative tracks equal the three-vector $\vec{p}$. The distance between the primary vertex and secondary vertex is defined as the conversion radius R. The positive and negative tracks are both propagated to the primary vertex. Further photon selection is done using the following four quantities:

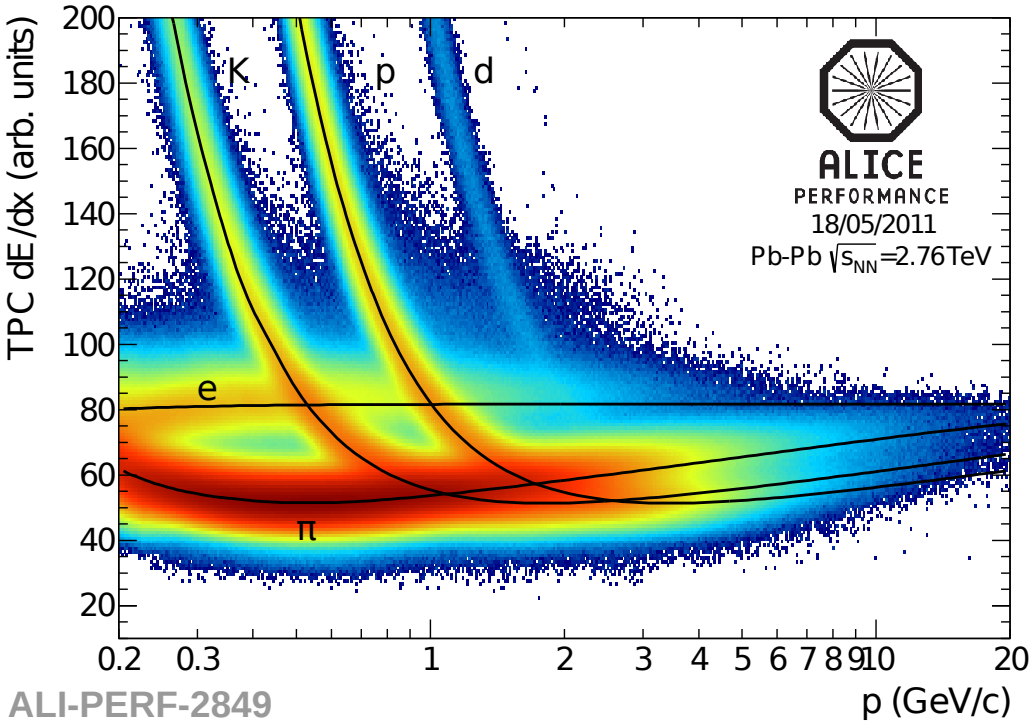

FIGURE 3.1: The specific energy loss (dE/dx) versus particle momentum for charged particles in the TPC.

1. Armenteros-Podolanski

Photon selection from the V^0 candidates can be further enhanced by selecting a region in the Armenteros-Podolanski plot. This combines two kinematic variables, q_T and α, such that photons can be discriminated from the K^0_S and $\Lambda(\bar{\Lambda})$. q_T is the relative momentum of the daughters with respect to the V^0. α is the longitudinal momentum asymmetry of the oppositely charged daughters and is defined as:

$$\alpha = \frac{p_L^+ - p_L^-}{p_L^+ + p_L^-} \tag{3.2}$$

Where p_L^+ is the longitudinal momentum of the positively charged daughter, and p_L^- is the longitudinal momentum of the negatively charged daughter. As shown in figure 3.3[24], the photon, K^0_S and $\Lambda(\bar{\Lambda})$ each have a characteristic band. For this analysis a two dimensional cut is applied to reject background:

$$\left(\frac{\alpha}{0.95}\right)^2 + \left(\frac{q_T}{q_{T,max}}\right)^2 > 1 \tag{3.3}$$

With $q_{T,max} = 0.05$ GeV/c.

2. Angle Ψ_{pair}

A photon selection cut can be made using the angles of the conversion daughters with respect to the magnetic

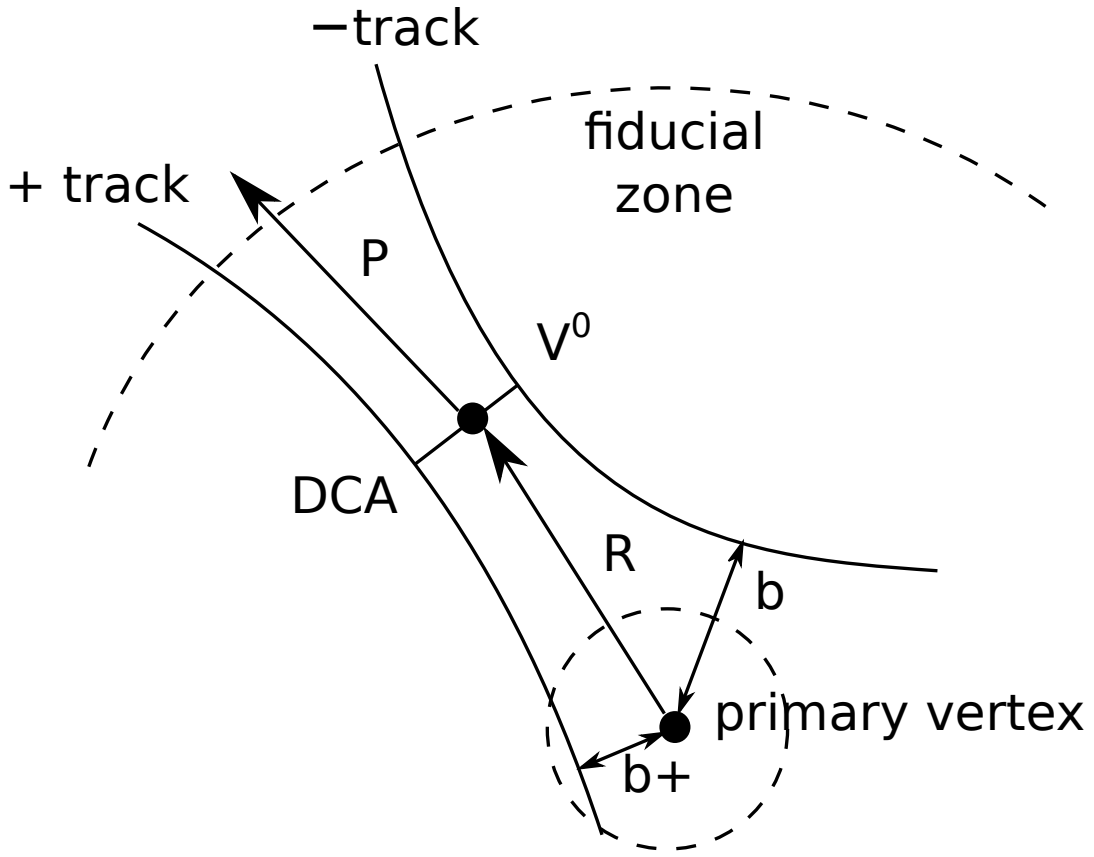

FIGURE 3.2: Topology of a V^0 candidate decaying to two oppositely charges particles.

field. First the angle ζ_{pair} is defined as:

$$\zeta_{pair} = \arccos\left(\frac{\vec{p^-} \cdot \vec{p^+}}{|| \vec{p^-} || \cdot || \vec{p^+} ||}\right) \tag{3.4}$$

With $p^{\pm}$ again the momentum of the positively and negatively charged daughter particles. Then Ψ_{pair} is the angle between the plane spanned by the opening angle of the daughters and the plane orthogonal to the magnetic field. It is calculated with:

$$\Psi_{pair} = \arcsin\left(\frac{\Delta\varphi}{\zeta_{pair}}\right) \tag{3.5}$$

With:

$$\Delta\varphi = \varphi^+ - \varphi^- \tag{3.6}$$

where φ^+ and φ^- are the angles between the positively and negatively charged conversion daughter and the transverse plane of the magnetic field. A cut in Ψ_{pair} is able to remove most of the combinatoric background.

3. Goodness of fit χ^2/ndf

A χ^2 test is done to evaluate the probability that the conversion particles have indeed a photon as mother particle. The number of degrees of freedom (ndf) is the amount of parameters included in the hypothesis.

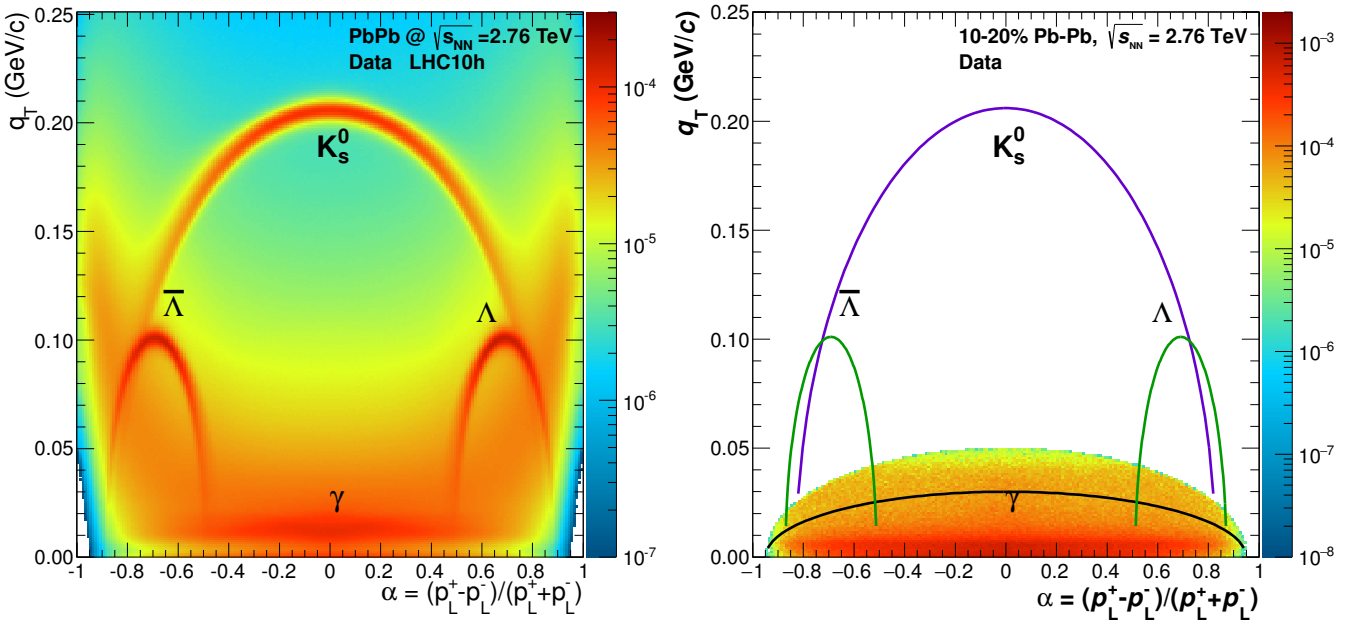

FIGURE 3.3: Armenteros-Podolanski plot before(left) and after(right) the applied cut in equation 3.3.

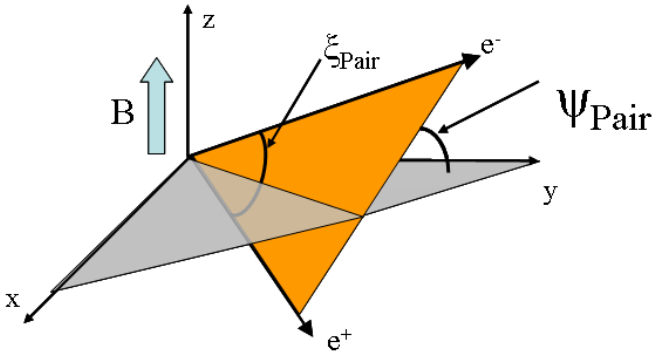

FIGURE 3.4: Ψ_{pair} is defined as the angle between the plane spanned by the conversion daughters and the plane transverse to the magnetic field.

χ^2/ndf can discriminate between signal and background and by default candidates with $\chi^2/ndf < 30$ are selected.

4. Cosine of pointing angle

The pointing angle, $\theta_{P.A.}$, is the angle between the total momentum vector of the conversion daughters ($\vec{p}$) and the vector that points from the primary vertex to the conversion point (R). Signal-like candidates have $\theta_{P.A.} \simeq 0$ while combinatorial background can have larger values. Only photons with $\cos(\theta_{P.A.}) > 0.85$ are considered in this analysis.

Photon cuts	
$q_{\mathrm{T,max}}$ (2D cut, $(\frac{\alpha}{0.95})^2 + (\frac{q_T}{q_{T,max}})^2 > 1$)	$< 0.05\ GeV/c$
χ^2_γ/ndf	< 30
ψ_{pair} (2D cut, $\lvert\psi_{pair}\rvert < \frac{-\psi^{cut}_{pair}}{\chi^2_{\gamma,cut}\cdot\chi^2_\gamma} + \psi_{pair,cut}$)	< 0.1
$cos(\theta_{P.A.})$ cut	> 0.85

TABLE 3.2: Conversion photon selection cuts.

3.2 Calorimetric method

With the calorimetric method in ALICE, the photons are reconstructed using either the EMCal or PHOS. For the neutral meson analysis presented in this thesis the EMCal is used. Photons hitting a calorimeter create a cascade of secondary particles, via the dominant processes bremsstrahlung and pair production. This is called an electromagnetic shower. The energy of the shower is deposited in multiple cells of the EMCal. The clusterizer algorithm V2 is used to reconstruct the clusters.
The clusterization process begins with a "seed" cell above the energy threshold of $E_{seed} = 0.5$ GeV. All clusters with a common side to the seed tower are aggregated as long as their energy is above the minimum energy $E_{min} = 0.1$ GeV and lower than the reference cell. This procedure is continued as long as there are valid clusters found for the aggregation step and each cell can belong to only one single cluster.

To characterize the shape of the found clusters, the shower shape parameters M02 and M20 are used. These moments are calculated in general by:

$$M_{mn} = \sum_k (x_1^{(k)})^m (x_2^{(k)})^n E_k; \quad m, n = 0, 1, 2... \tag{3.7}$$

Where k runs over all cells in the cluster, x_1 and x_2 are the cell coordinates in the cluster coordinate system and E_k is the cell energy. M02 and M20 characterize both axis of the shower surface ellipse. M02 can be identified with the long axis of the ellipse while M20 stands for the short axis. Additionally, there is another shower shape parameter called dispersion. The dispersion is a classical measure of the shower width which is calculated by weighting the single contributing cells by the deposited energy with respect to their position.

3.2.1 Cluster energy correction

The total energy of the cluster is the sum of the energies of the cells belonging to the cluster. Usually, an absolute energy calibration is performed using test-beam data in order to have data match with MC. However, the team-beam conditions don't necessarily correspond to the ALICE data taking conditions. Alternatively, the energy correction can be done by using the peak position of the π^0 in data and MC.

The new cluster energy correction is applied on MC with the purpose of matching the MC cluster energies to data cluster energies. The correction ensures that the peak position of reconstructed neutral mesons in

both MC and data is the same, which is needed to correctly extract the raw yield and calculate the efficiency corrections. The cluster energy correction is calculated in the following steps:

1) Fit the π^0 peaks in data and MC to obtain the mass positions as function of cluster energy.

2) Calculate the ratios of mass positions in data and Monte Carlo.

3) Obtain the correction function by parametrizing the ratio of mass positions.

This correction scheme can be done by reconstructing $\pi^0 \rightarrow \gamma\gamma$ with both photons in the EMCal, or by the hybrid method where one photon is reconstructed with the photon conversion method. Both methods lead to similar correction factors, but the hybrid method has the advantage that it benefits from the resolution of the tracking detectors. Since the energy of the cluster is calculated from the p_{T} of the meson, only photons of similar energies are paired for the EMCal-EMCal method. This constraint is applied by a cut in the energy asymmetry of the photon pair. For the PCM-EMCal this is the energy of the conversion photon is known and the EMCal photon is not constrained. The ratio of the mass positions is fitted by:

$$f(E_{\mathrm{Cluster}}) = p_0 + \exp\left(p_1 + p_2 \cdot E_{\mathrm{Cluster}}\right), \tag{3.8}$$

with three free parameters p_0, p_1 and p_2. The results for the energy corrections using this method are shown in figure 3.5. The left plots show the reconstructed π^0 mass positions divided by the PDG π^0 mass, as function of cluster energy, for data and MC. As can be seen, the reconstructed mass for data is higher, which means that the cluster energy in MC needs to be corrected upwards. The correction function is shown in the right plots. The black line is obtained from a direct ratio of the π^0 mass positions and the green line from the ratio of the fits of the π^0 mass positions. The PCM-EMCal cluster energy correction is used by default and the EMCal-EMCal cluster energy correction will be used in the determination of the systematic uncertainty.

3.2.2 Cluster selection

EMCal cell cuts	
cell threshold	100MeV
seed threshold	500MeV
minimum cell time	-500ns
maximum cell time	+500ns

TABLE 3.3: Standard cuts for the EMCal cell selection.

The list of cuts applied on EMCal cells and clusters can be found in table 3.3 and table 3.4. The applied cuts are kept loose so that most photon-like candidates are accepted. This is appropriate for neutral meson analyses because the background can be subtracted using invariant mass methods, which is explained in a later chapter.

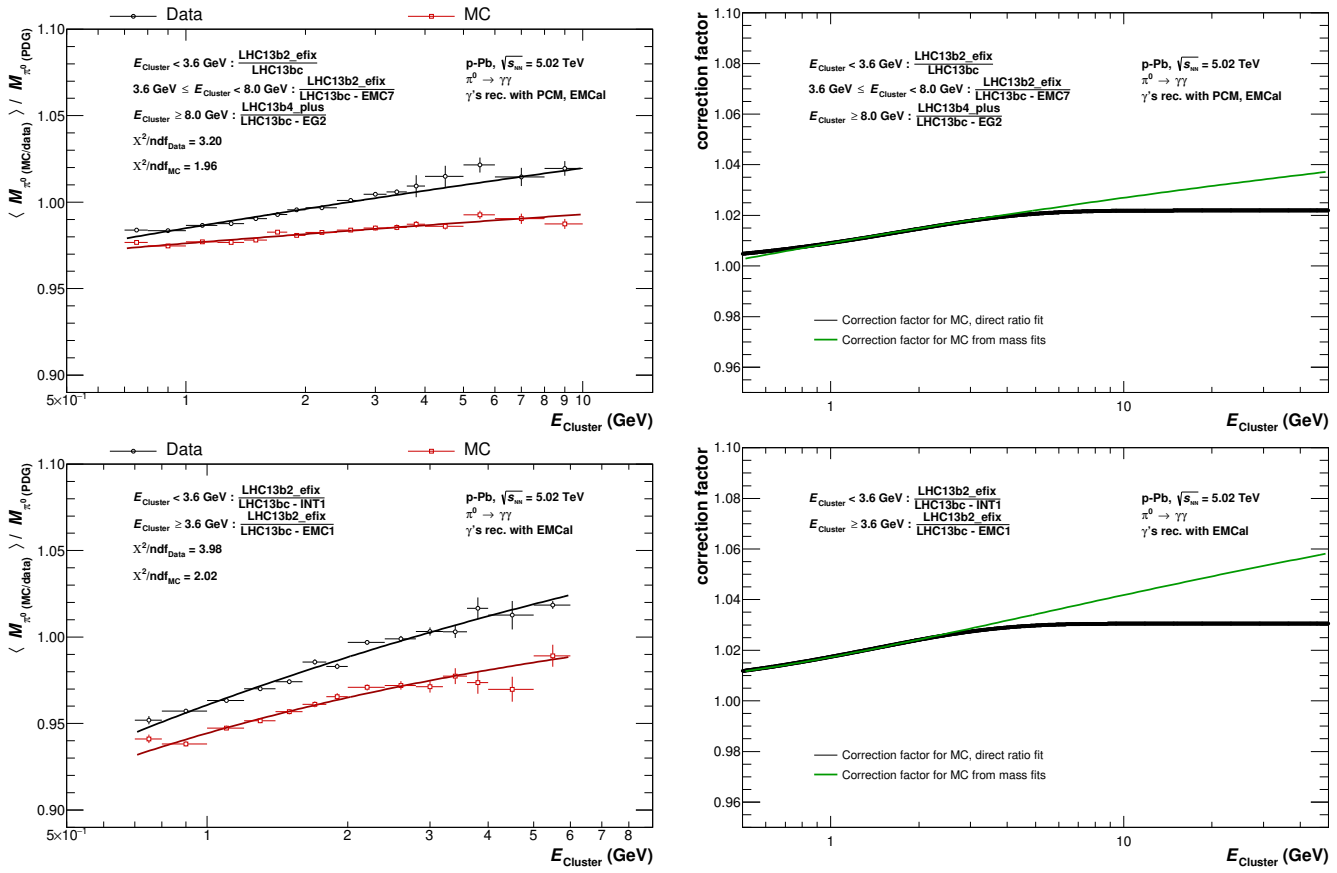

FIGURE 3.5: The left figures show the obtained mass positions for PCM-EMCal(top) and EMCal-EMCal(bottom) case. For both plots, the black/red lines display the fits to the mass positions. The right side shows the correction factor that is applied to the cluster energy in MC for PCM-EMCal(top) and EMCal-EMCal(bottom) case.

EMCal cluster cuts	
cluster type	EMCal
clusterizer	V2
minimum cluster energy	$E_{\text{cluster}} > 0.7$ GeV
minimum number of $N_{\text{cluster}}^{\text{cells}}$	≥ 2
shape parameter M02	$0.1 \leq \text{M02} \leq 0.5$
TOF	≤ 50 ns

TABLE 3.4: Standard cuts for the EMCal cluster selection.

The first set of cuts are applied on cell level. There is a cell energy threshold of 100 MeV, removing most of the noise and lowering the background. The seed threshold of the V2-clusterizer is set to 500 MeV. There is a possibility of a time cut on cell level, but is not applied such that all candidates are included. In addition, these variations on cell timing and thresholds are included in the systematic uncertainty studies.

The second set of cuts are applied on cluster level. The minimum number of cells to form a cluster is set to 2. This means that the bare minimum energy of a reconstructed cluster is 600 MeV(500 MeV seed threshold and 100 MeV cell theshold) and it is therefore chosen to have 0.7 GeV as minimum energy for a cluster. The seed of the cluster defines the cell time, and a TOF cut of $|t_{cluster}| \leq 50$ns is applied to select the clusters

of the main bunch crossing. The energy of the leading cell is well above the cell threshold of 100MeV and has a well defined cell time. Additionally, there is a cut applied on the shape parameter M02, in order to further select photon-like candidates.

In figure 3.6, the η-ϕ distributions of selected EMCal clusters after applying the full set of cluster cuts are shown for data and MC. They show that the modules are reasonably uniform in the amount of reconstructed clusters and that the dead areas are correctly taken into account in the MC production. The histograms are scaled by the number of events which are available for the respective production. Furthermore, every distribution is normalized to the global average number of clusters per bin.

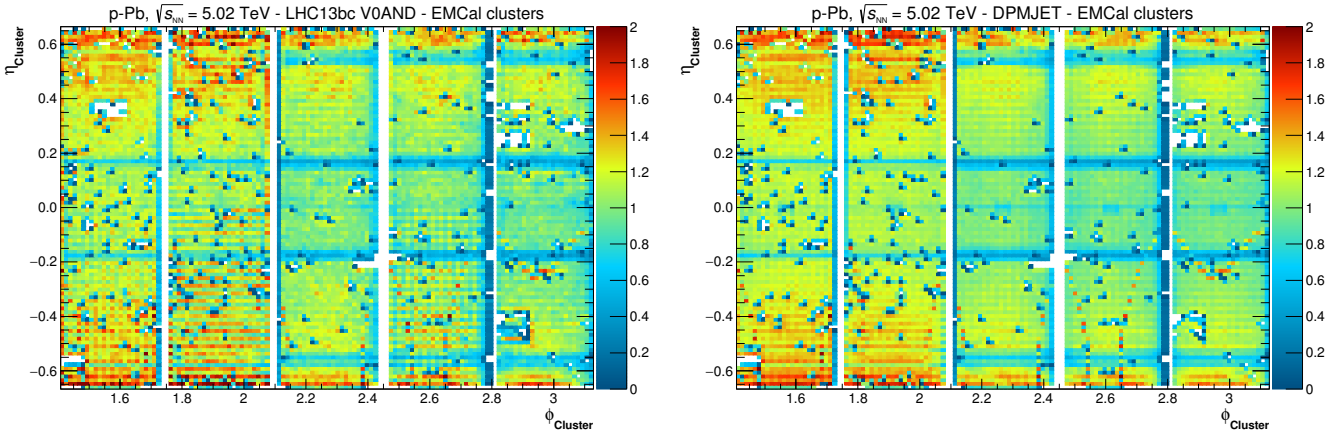

FIGURE 3.6: EMCal cluster in η and ϕ for Data(left) and MC(right).

Part I

Neutral mesons

Chapter 4

Neutral meson reconstruction

The corrected invariant cross sections of two neutral mesons, the π^0 and η, is measured using the EMCal in p-Pb collisions at $\sqrt{s_{NN}} = 5.023$ TeV. This chapter describes how the neutral mesons are reconstructed and how the raw yield is extracted.

4.1 Invariant mass method

Both neutral mesons are reconstructed using their decay channel into two photons, $\pi^0 \to \gamma\gamma$ and $\eta \to \gamma\gamma$. The rest masses are 0.135 GeV/c^2 and 0.548 GeV/c^2 for the π^0 and η meson, respectively. The decay photons are obtained using the clusterizer algorithms and additional selection is done using the EMCal cell and cluster cuts. Every photon candidate is combined to calculate the invariant mass of the pair, which is given by

$$M_{\gamma\gamma} = \sqrt{2E_{\gamma_1}E_{\gamma_2}(1-\cos\theta_{12})}. \tag{4.1}$$

$E_{\gamma_{1,2}}$ represent the energies of the two photons and θ_{12} is the opening angle between the two photons, where the angle is calculated with respect to the collision vertex.

The π^0 and η mesons are reconstructed as an excess yield on top of combinatorial background. The background has a particular shape and can be calculated with the Event Mixing technique, in order to subtract it from the combined signal and background. With the Event Mixing technique photons from different events are combined, such that there are no correlations coming from decays. This is done in bins of event multiplicity and primary vertex position.

4.2 Signal extraction

The transverse momentum binned invariant mass distributions, obtained with equation 4.1, are used to extract the signal. First, the combinatorial background is scaled to match the background of the combined signal and background distribution, using the left side of the distribution. Then, the combinatorial background subtracted invariant mass distributions is fitted with:

$$y = A\left(G(M_{\gamma\gamma}) + \exp\left(\frac{M_{\gamma\gamma} - M_{\pi^0(\eta)}}{\lambda}\right)(1 - G(M_{\gamma\gamma}))\theta(M_{\gamma\gamma} - M_{\pi^0,\eta})\right) + B + C \cdot M_{\gamma\gamma} \tag{4.2}$$

$$\text{, with } G = \exp\left(-0.5\left(\frac{M_{\gamma\gamma} - M_{\pi^0,\eta}}{\sigma_{M_{\gamma\gamma}}}\right)^2\right). \tag{4.3}$$

Here G is a Gaussian with width σ and mean $M_{\pi^0(\eta)}$, which can be identified with the reconstructed mass width and position of the corresponding meson. The parameter λ represents the inverse slope of the exponential function. The contribution of the exponential function above $M_{\pi^0(\eta)}$ is switched off by the Heavyside function $\theta(M_{\gamma\gamma} - M_{\pi^0,\eta})$. B and C are the parameters of a linear function that takes care of remaining background after mixed background subtraction. Figure 4.1 and figure 4.2 show examples of invariant mass distributions for the π^0 and η meson, and show that this fit describes to total signal well. Figure 4.3 shows the reconstructed mass positions and widths for the π^0 and η meson, as function of transverse momentum. The mass positions and widths in data and MC are in reasonable agreement, as they are corrected by the cluster energy correction previously described.

The raw meson yield is extracted by bin counting the background subtracted invariant mass distributions around the fitted meson mass:

$$N^{\pi^0}_{\text{raw}} = \int_{M_{\pi^0}-0.032\ \text{GeV}/c^2}^{M_{\pi^0}+0.022\ \text{GeV}/c^2} (N^{\gamma\gamma} - N^{\text{comb. BG}})dM_{\gamma\gamma} - \int_{M_{\pi^0}-0.032\ \text{GeV}/c^2}^{M_{\pi^0}+0.022\ \text{GeV}/c^2} (B + C \cdot M_{\gamma\gamma})dM_{\gamma\gamma}. \tag{4.4}$$

The standard integration range for π^0 meson is (M_{π^0} - 0.032 GeV/c^2, M_{π^0} + 0.022 GeV/c^2), while for the η the integration range is (M_η - 0.060 GeV/c^2, M_η + 0.050 GeV/c^2), taking into account the larger reconstructed width of the η meson.

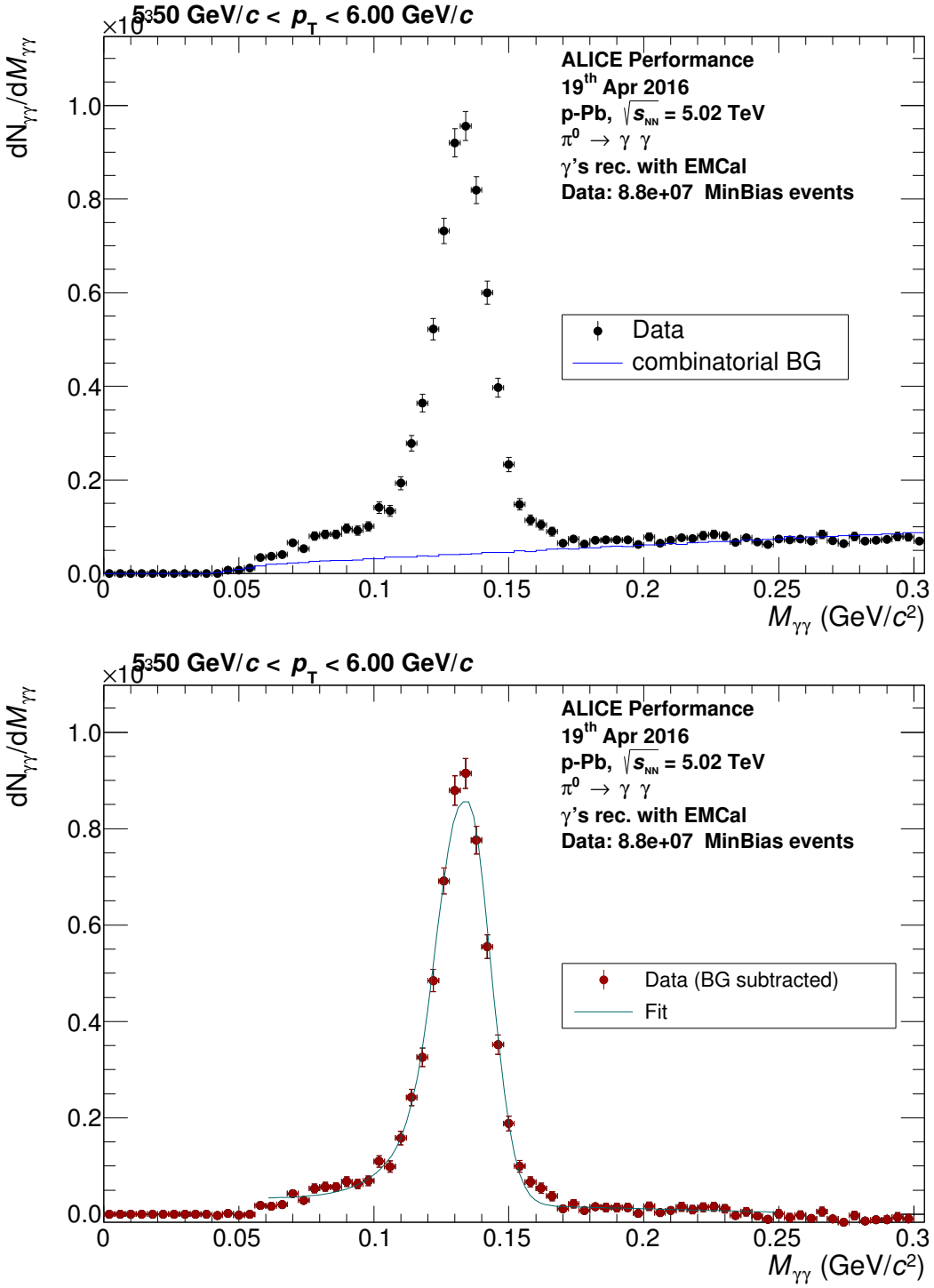

FIGURE 4.1: The π^0 mass distribution for 5.5GeV/c $< p_T <$ 6.0GeV/c. Top: The combined signal and background together with the scaled combinatoric background. Bottom: Fitted invariant mass distribution from which the raw yield is extracted.

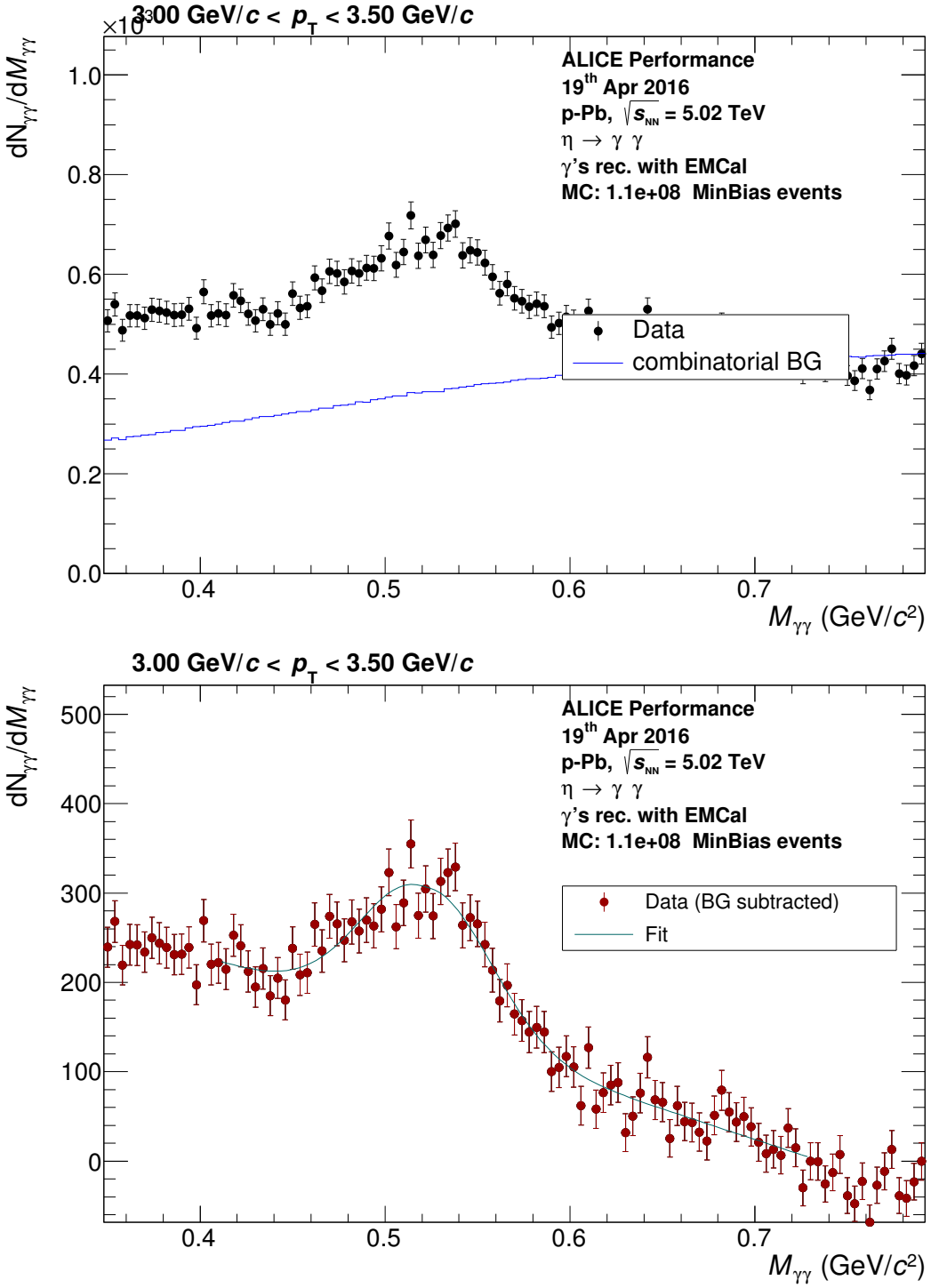

FIGURE 4.2: The η mass distribution for 3.0GeV/c $< p_T <$ 3.5GeV/c. Top: The combined signal and background together with the scaled combinatoric background. Bottom: Fitted invariant mass distribution from which the raw yield is obtained.

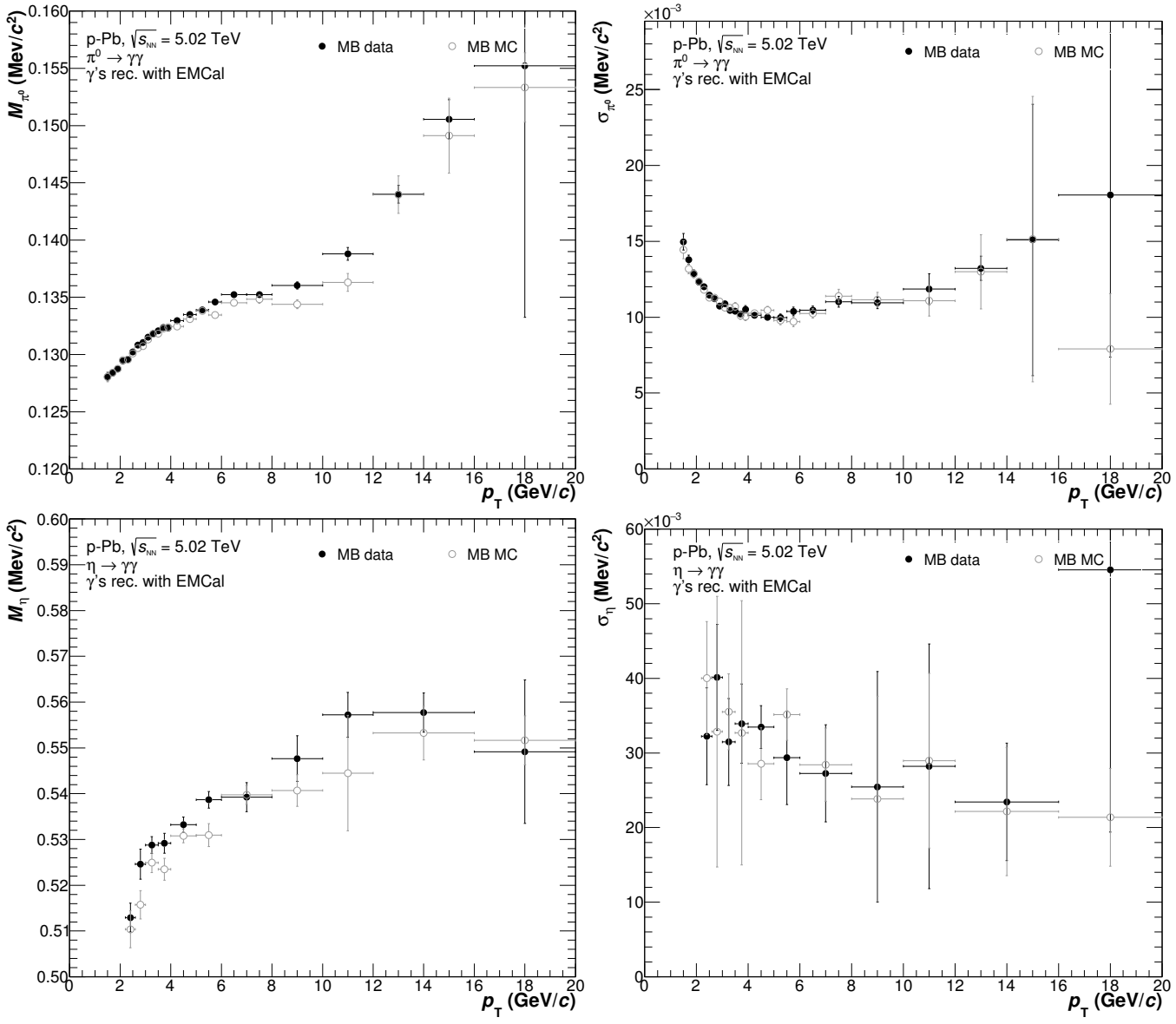

FIGURE 4.3: The reconstructed mass positions and widths of the π^0 and η meson as function of transverse momentum, for data and MC.

Chapter 5

Neutral meson corrections

The raw π^0 yield needs to be corrected for secondary π^0's from different sources, such as weak decays and hadronic interactions. Furthermore, both the π^0 and η needs to be corrected for acceptance and reconstruction efficiency of the EMCal detector.

5.1 Secondary neutral pion correction

Monte Carlo simulations are used to simulate the contribution of secondary π^0's to the raw yield of the π^0 meson. The largest source of secondary π^0's comes from $K^0_s \to \pi^0\pi^0$ with a branching ratio of 30.7%. Figure 5.1 shows the fraction of secondary π^0's to the raw yield of the reconstructed π^0. For high p_T the total contribution is of the order of 2%, while it grows for lower p_T. The raw yield is multiplied with the secondary correction ratio such that the number of secondary π^0's can be subtracted from the uncorrected raw yield.

5.2 Acceptance and efficiency correction

The remaining raw yield of the π^0 and η meson needs to be corrected for detector acceptance and reconstruction efficiency. Both quantities are calculated using Monte Carlo simulations.

The geometrical acceptance $A_{\pi^0(\eta)}$ is defined as the ratio of π^0 (η) mesons within $|y| < 0.5$, whose daughter particles are within the fiducial acceptance ($-0.6687 < \eta_\gamma < 0.66465$), over all π^0 (η) mesons generated in the same rapidity window.

$$A_{\pi^0(\eta)} = \frac{N_{\pi^0(\eta),|y|<y_{\max},\eta_\gamma}}{N_{\pi^0(\eta),|y|<y_{\max}}} \tag{5.1}$$

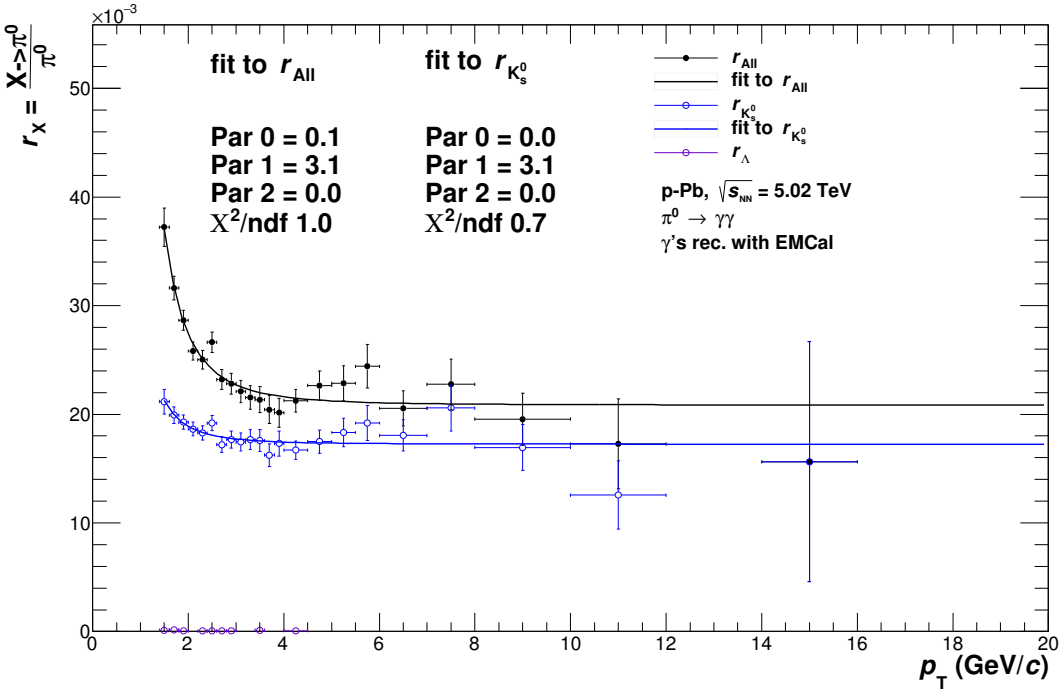

FIGURE 5.1: Ratio r_X of reconstructed secondary π^0 mesons from K^0_s mesons (blue) or all secondary π^0 mesons (black) to reconstructed π^0's. The blue and black line represent the fit to the corresponding fractions with $f(x) = \frac{a}{x^b} + c$.

Figure 5.2 shows the resulting geometrical acceptance for π^0 (left) and η (right) mesons. The acceptance goes down for lower transverse momentum as the opening angle of the decay photons becomes larger, meaning that one of the photons is more likely to escape the detection region. As the mass of the η meson is larger than the mass of the π^0 meson the opening angle between the daughter particles is wider and thus the acceptance rises more slowly.

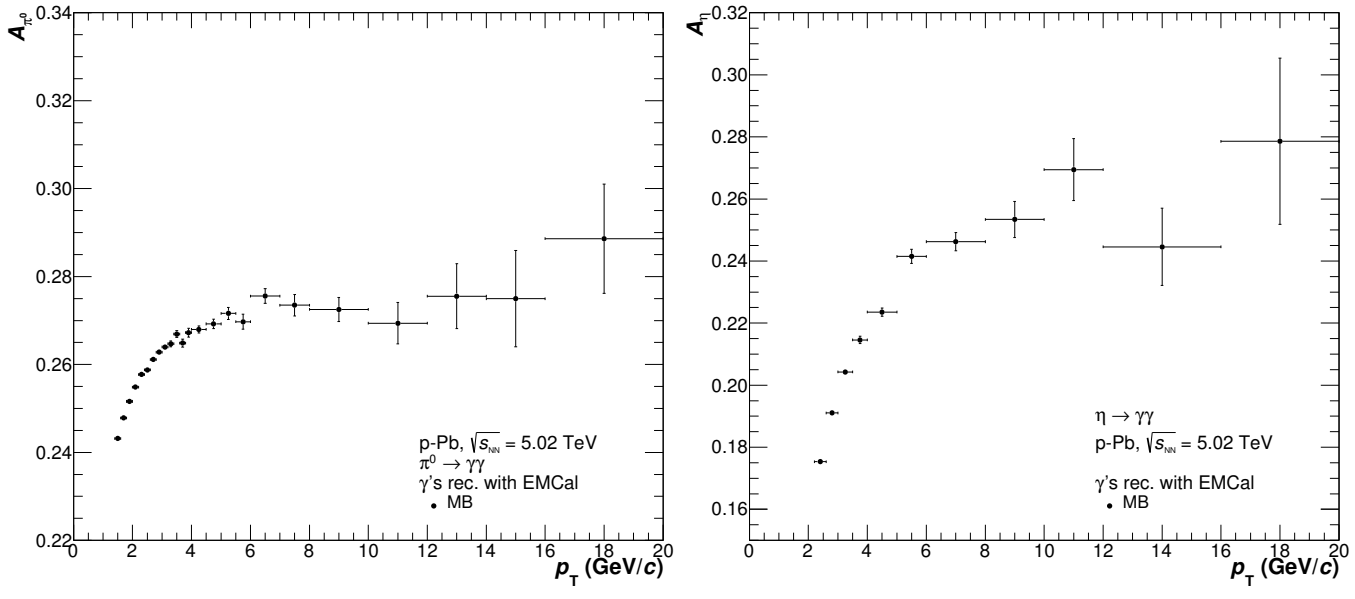

FIGURE 5.2: Acceptance correction for the π^0 (left) and η (right) mesons.

In order to estimate the reconstruction efficiency the same analysis as in real data has been performed on simulated data. A second efficiency has been calculated, where each photon is verified using the Monte Carlo information and it has been checked that they originate from the same particle (π^0 or η meson). This is called validated efficiency. Those two efficiencies have been compared and it has been found that they are in reasonable agreement.

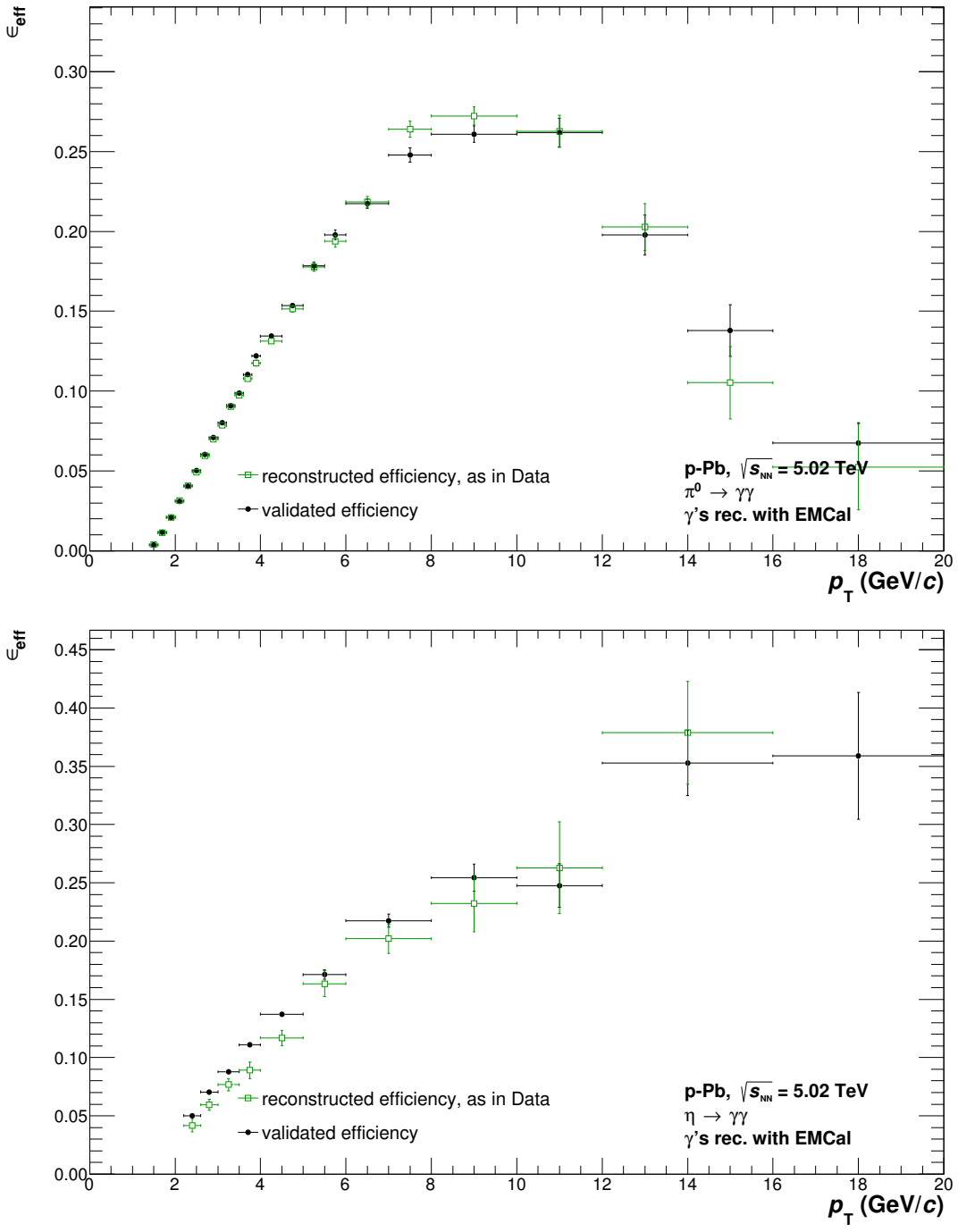

FIGURE 5.3: Efficiency correction for the π^0 (top) and η (bottom) mesons.

The reconstruction efficiency $\epsilon_{\text{reco, }\pi^0(\eta)}$ is shown in 5.3 for the π^0 and η meson. It is defined as follows:

$$\epsilon_{\text{reco, }\pi^0(\eta)} = \frac{N_{\pi^0(\eta),\text{MC rec}}}{N_{\pi^0(\eta),|y|<y_{\max},\eta_\gamma}} \tag{5.2}$$

Where $N_{\pi^0(\eta),\text{MC rec}}$ is the number of $\pi^0(\eta)$ mesons reconstructed in the MC and $N_{\pi^0(\eta),|y|<y_{\max},\eta_\gamma}$ is the number of $\pi^0(\eta)$ mesons generated within $|y| < 0.5$, whose daughter particles are within the fiducial acceptance ($-0.6687 < \eta_\gamma < 0.66465$). The shape of the reconstruction efficiency is determined by the photon reconstruction efficiency of the EMCal together with the decay kinematics of the meson. The efficiency to reconstruct a cluster becomes larger for increasing p_T , explaining the trend for low p_T . For higher p_T the meson is more boosted and the clusters begin to merge because of the decreasing opening angle of the decay photons, explaining the trend for higher p_T . For the η meson this effect is less pronounced because the cluster merging starts much later compared to the π^0 meson.

Chapter 6

Neutral meson results

This chapter presents the result of the neutral meson analysis measured with the EMCal for p-Pb collisions at $\sqrt{s_{NN}}$ = 5.023 TeV. First the systematic error evaluation is described. Then the corrected invariant cross sections of the π^0 and η is given where the comparison is made to different analysis methods. Finally, the nuclear modification factor $R^{\pi^0}_{p-Pb}$ of the combined measurement will be presented and compared to state of the art theoretical models.

6.1 Systematic error evaluation

In order to estimate the systematic error for the π^0 and η meson in p-Pb, each cut which has been used to select the photons, clusters and mesons is varied. These variations are chosen such that a reasonable deviation can be accessed. To calculate the contribution of every cut variation only one cut is varied at a time and the differences to the fully corrected spectra are calculated bin by bin in p_{T} by:

$$\Delta(p_{\mathrm{T}}) = \left(\frac{\mathrm{d}^2N}{\mathrm{d}y\mathrm{d}p_{\mathrm{T}}}\right)_{\text{modified}}(p_{\mathrm{T}}) - \left(\frac{\mathrm{d}^2N}{\mathrm{d}y\mathrm{d}p_{\mathrm{T}}}\right)_{\text{standard}}(p_{\mathrm{T}}) \tag{6.1}$$

Fluctuations in p_T are reduced by smoothing the systematic errors. The smoothing is done by fitting the p_{T} dependent systematic error with an n-order polynomial where n is kept as low as possible while describing the trend. The total systematic error is obtained by calculating the quadratic sum. Figure 6.1 shows the results of all sources of systematic errors for the corrected π^0 and η invariant cross sections and the η/π^0 ratio. Most systematic errors are not heavily p_{T} dependent, such as the material budget in front of the EMCal, minimum energy of the cluster and reconstruction efficiency. Other sources of systematic errors, like the yield extraction, cluster shape parameter M_{02} and $\theta_{\gamma\gamma}$ are p_{T} dependent as the variations affect the

high p_{T} mesons more than the low p_{T} mesons. The tables listing the full set of systematic variations can be found in appendix A.

6.2 Invariant cross sections

The corrected π^0 and η invariant cross section can be calculated by applying the corrections for acceptance and efficiency. In the case of the π^0 meson, the raw yield is already corrected for secondaries. The invariant cross section is given by:

$$E\frac{\mathrm{d}^3N}{dp^3} = \frac{\mathrm{d}^3N}{p_{\mathrm{T}}\mathrm{d}p_{\mathrm{T}}\mathrm{d}y d\varphi} = \frac{1}{2\pi}\frac{1}{p_{\mathrm{T}}}\frac{\mathrm{d}^2N}{\mathrm{d}y\mathrm{d}p_{\mathrm{T}}} = \frac{1}{2\pi}\frac{1}{N_{\mathrm{evt.}}}\frac{1}{p_T}\frac{1}{\epsilon_{\mathrm{reco},\,\pi^0(\eta)}}\frac{1}{A_{\pi^0(\eta)}}\frac{1}{\mathrm{BR}}\frac{N^{\pi^0(\eta)}}{\Delta y \Delta p_{\mathrm{T}}} \tag{6.2}$$

Here $N_{\mathrm{evt.}}$ is the number of events passing event selection, BR the branching ratio of the decay $\pi^0(\eta) \to \gamma\gamma$ and $N^{\pi^0(\eta)}$ the reconstructed raw yield for the π^0 or η meson within the rapidity range y in [-0.5,0.5] and the transverse momentum bin Δp_{T}. Figure 6.2 shows the result for the corrected π^0 and η invariant cross section in p-Pb collisions at $\sqrt{s_{NN}} = 5.023$TeV. The result of three additional neutral meson reconstruction methods are shown to compare with the EMCal measurement. A PCM, Dalitz, EMCal and PHOS combined spectra is obtained by averaging the yield per p_{T} bin, using the total uncertainty as weight. The combined measurement, as shown in figure 6.3, is fitted with the Tsallis function:

$$\frac{1}{2\pi N_{ev}}\frac{\mathrm{d}^2N}{p_{\mathrm{T}}\mathrm{d}p_{\mathrm{T}}\mathrm{d}y} = \frac{A}{2\pi}\cdot\frac{(n-1)\cdot(n-2)}{nT\cdot(nT+m\cdot(n-2))}\cdot\left(1+\frac{m_T-m}{nT}\right)^{-n}, \tag{6.3}$$

where A, n and T are the free parameters of the Tsallis fit. m and m_T are the mass and transverse mass of the fitted meson. The Tsallis fit is able to describe the invariant cross section of both the π^0 and η meson for the full tranverse momentum range with good agreement. The individual neutral meson reconstruction methods are compared to the combined fit and the result is shown in figure 6.4.

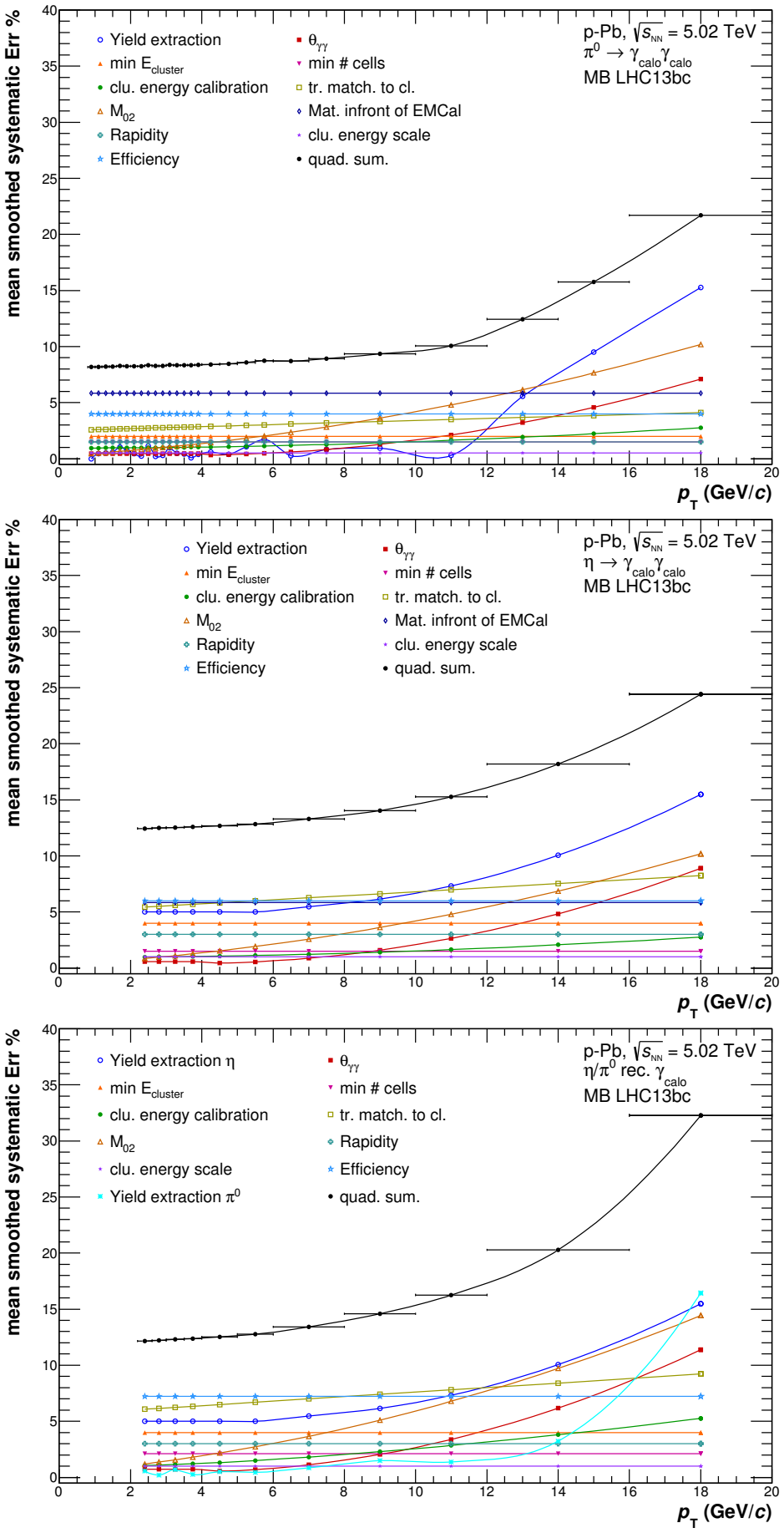

FIGURE 6.1: Transverse momentum dependent systematic error % for the corrected invariant π^0 and η cross sections and the η/π^0 ratio.

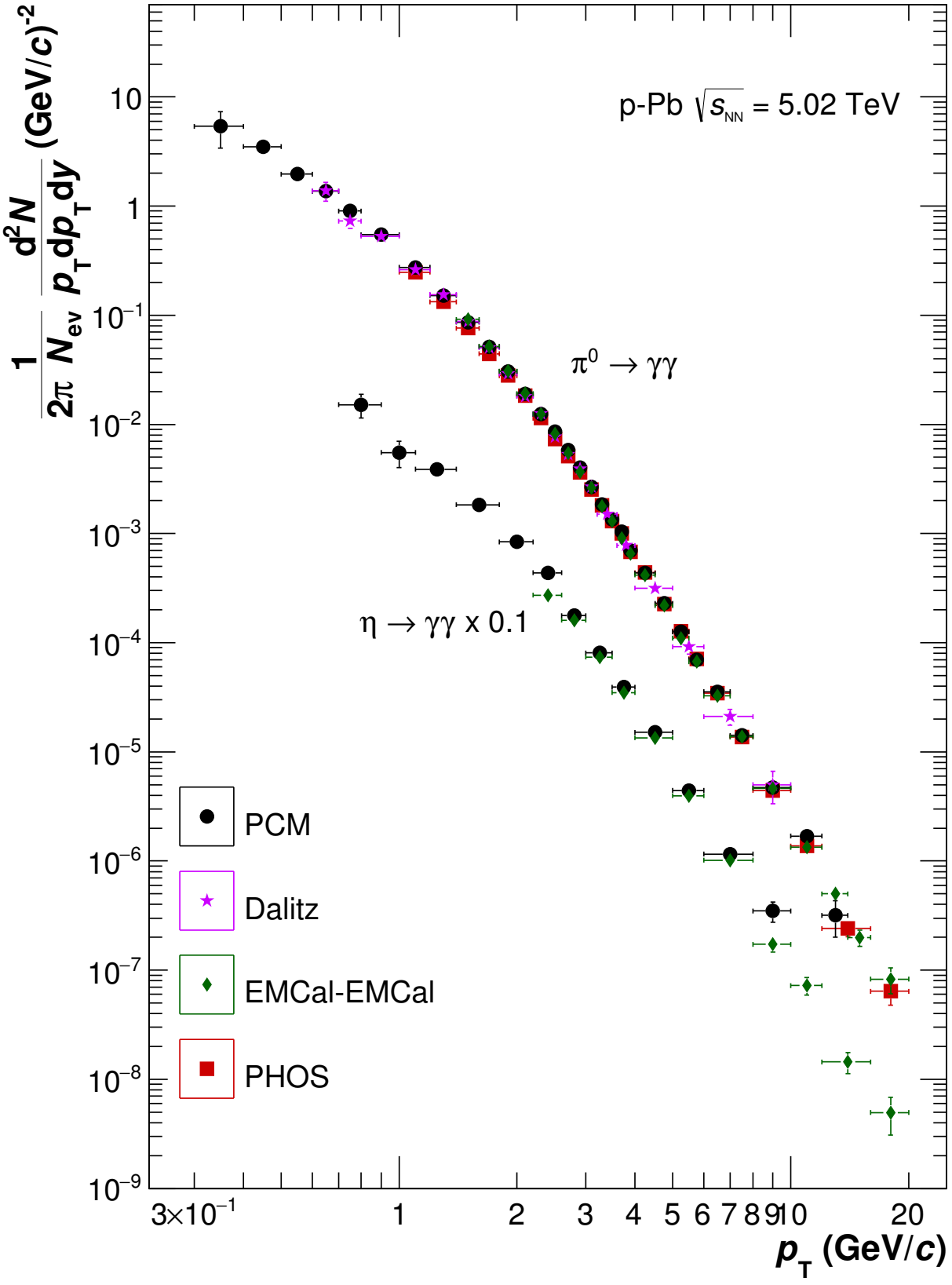

FIGURE 6.2: The π^0 and η invariant cross sections for four different reconstruction methods.

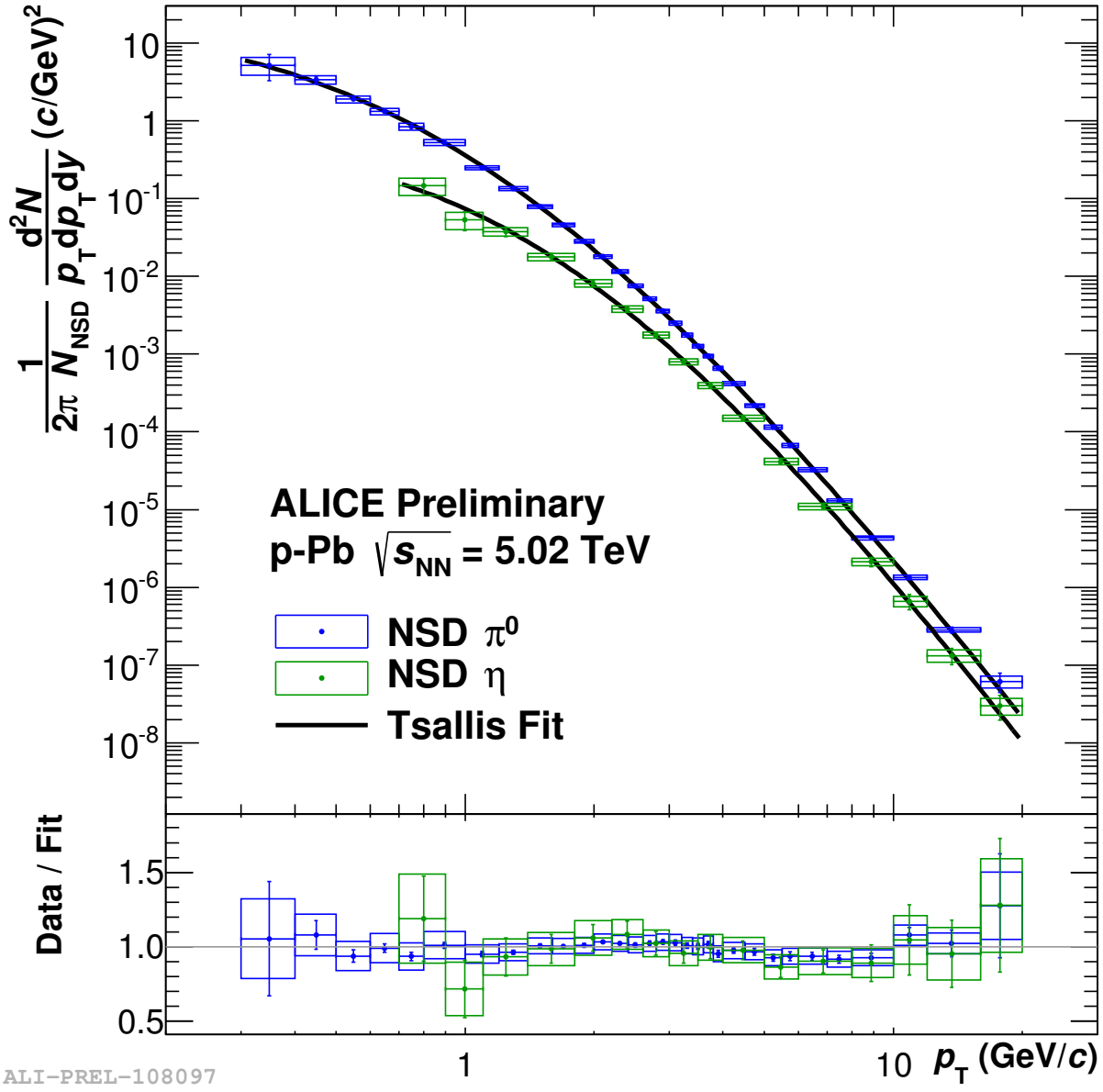

FIGURE 6.3: The combined π^0 and η invariant cross sections using the PCM, Dalitz, EMCal and PHOS reconstruction methods. It is fitted using the Tsallis function.

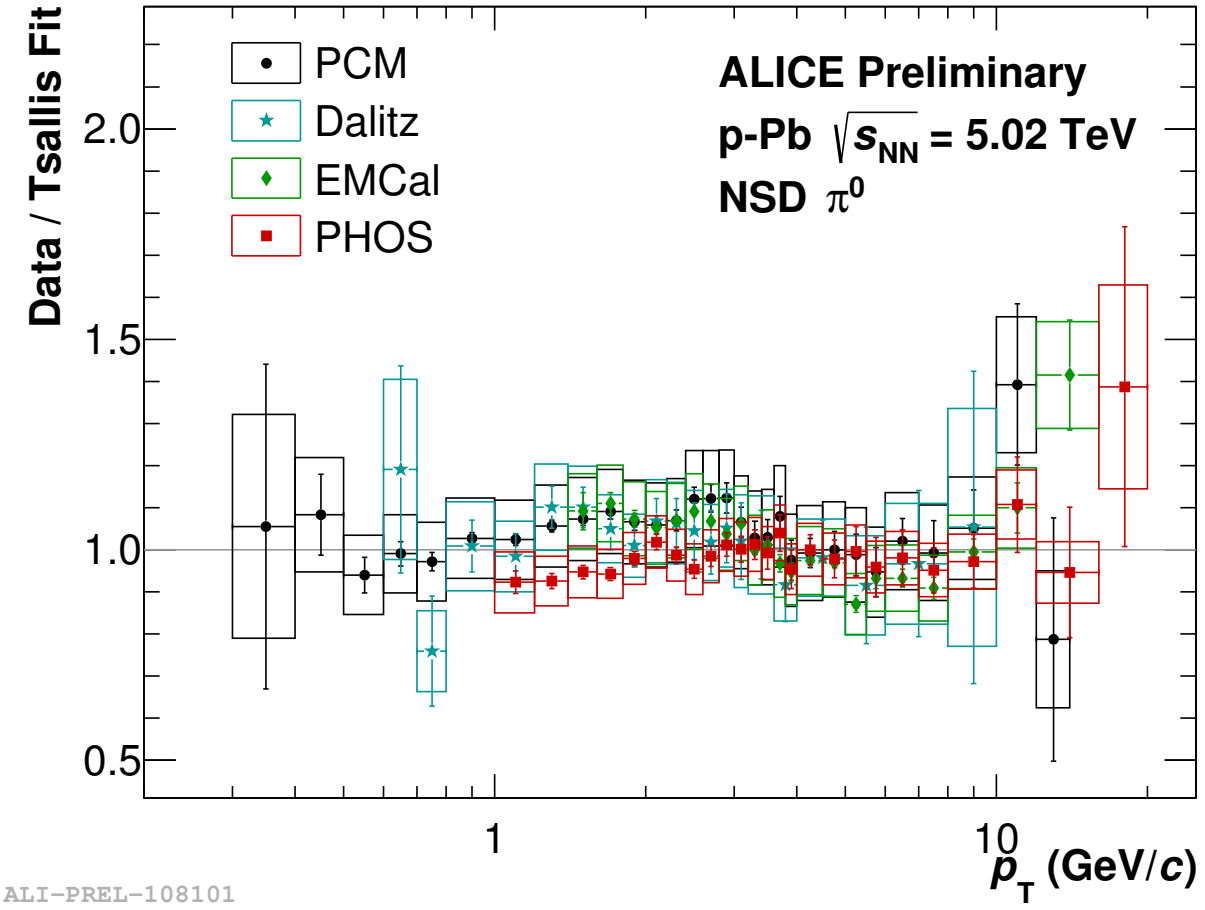

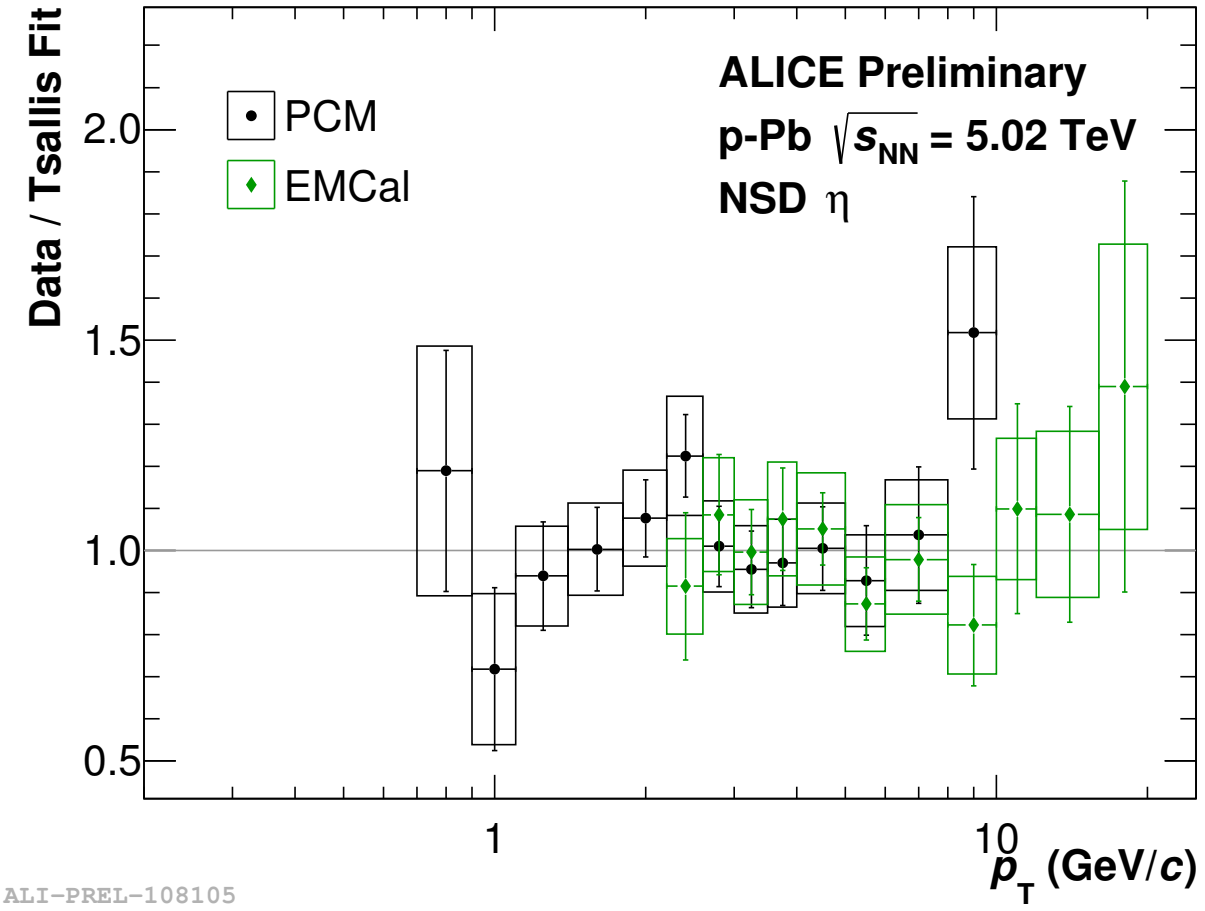

FIGURE 6.4: Comparison of the π^0(top) and η(bottom) invariant cross sections of the four different reconstruction methods to the Tsallis fit of the combined measurement.

6.3 η/π^0 ratio

The η/π^0 ratio can be calculated from the π^0 and η invariant cross sections. The result for the EMCal method and PCM is shown in figure 6.5(top). It shows that both methods are consistent in the given p_{T} range. PCM extends to lower p_{T} while the EMCal method extends to higher p_{T} .

The combined measurement is shown in figure 6.5(bottom) and is compared to the pp $\sqrt{s} = 7$ TeV and m_T scaled result. The combined measurement is consistent with the pp $\sqrt{s} = 7$ TeV measurement, which indicates that there is no additional η production mechanism in p-Pb collisions compared to pp collisions. Howerver, there is a tension between the combined η/π^0 ratio and the η/π^0 ratio where the η is m_T scaled from the π^0. m_T scaling assumes:

$$\frac{Y^1(m_T)}{Y^2(m_T)} = \text{constant}. \tag{6.4}$$

Which means the yields of two particles are the same, up to a constant, as function of transverse mass. At low p_{T} m_T scaling seems to be broken, as the red dashed line is above the measured data points, while being consistent for higher p_{T} . An explanation for the tension at low p_{T} could be that the π^0 spectrum contains feed down from the η, which is currently not corrected for.

6.4 Neutral pion R_{p-Pb}

The R_{pPb} is calculated using the EMCal π^0 spectrum in p-Pb collisions at $\sqrt{s_{NN}}$ = 5.023 TeV using

$$R_{p-Pb}(p_T) = \frac{d^2N/dp_T dy\,|_{p-Pb}}{\langle T_{p-Pb}\rangle\, d^2\sigma/dp_T dy\,|_{pp}}, \tag{6.5}$$

with $\langle T_{p-Pb}\rangle = \langle N_{coll}\rangle / \sigma_{NN} = 0.0983 \pm 0.0035\mathrm{mb}^{-1}$. For the pp reference an interpolation between 2.76 TeV and 7 TeV spectrum has been made to get an estimate of the π^0 spectrum at 5.023 TeV, using the PCM and PHOS measurement. The pp references and interpolated pp spectra are shown in figure 6.6. The interpolation is by fitting each p_{T} bin assuming a power law behaviour and the assigned systematic error is obtained from the nearest reference spectrum. The π^0 R_{p-Pb} using the combined R_{pPb} of the different methods(PCM, EMCal, PHOS and Dalitz) is shown in figure 6.7. Comparisons are made to different state of the art theoretical models. The NLO pQCD model uses the EPS09 nuclear PDF with different fragmentation functions and show to be consistent with data. The Color Glass Condensate(CGC) model prediction, assuming gluon saturation, also shows to be consistent with data.

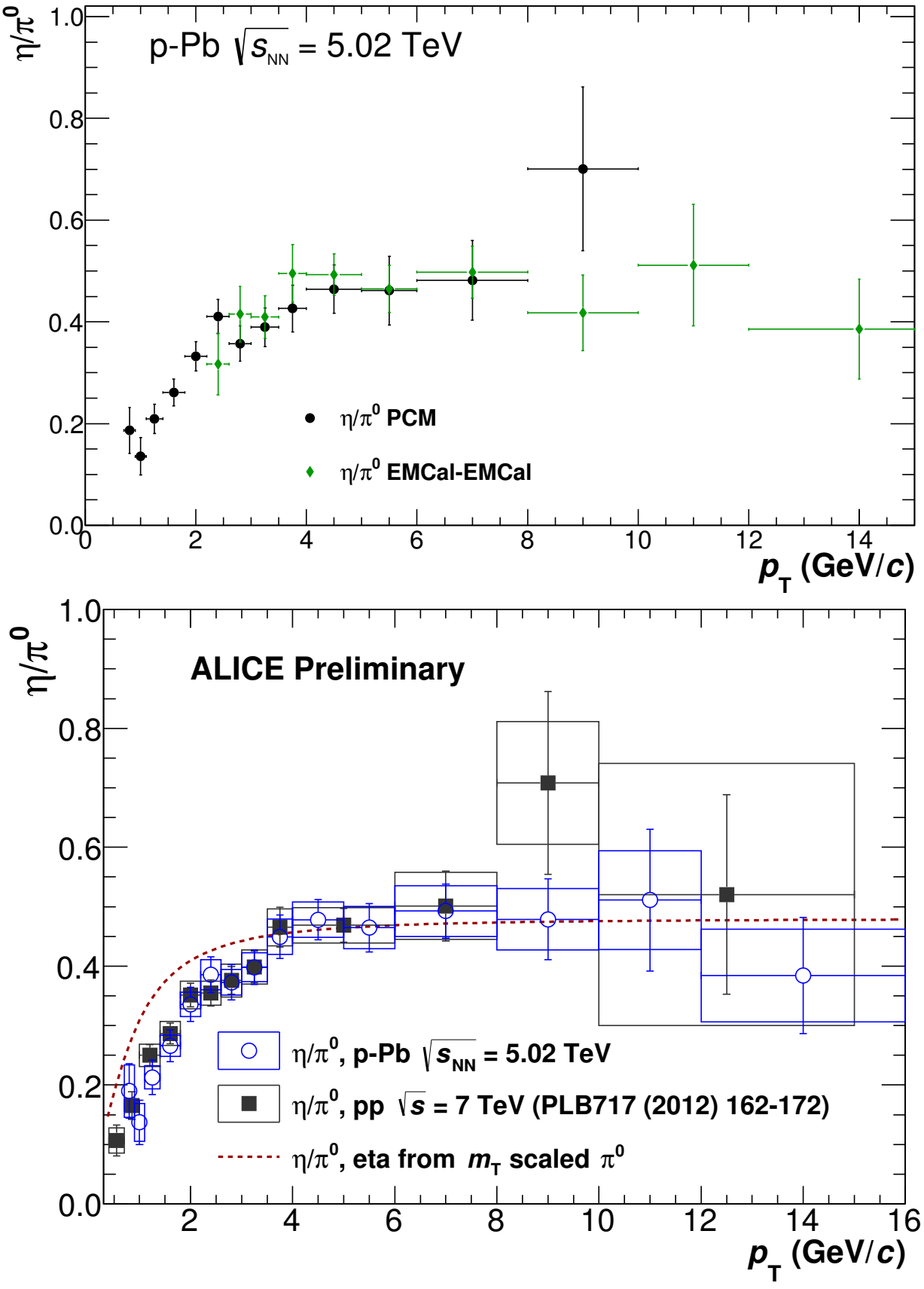

FIGURE 6.5: The η/π^0 ratio obtained from the EMCal and PCM method(top) and the combined measurement compared to the pp $\sqrt{s} = 7$ TeV and m_T scaled result(bottom).

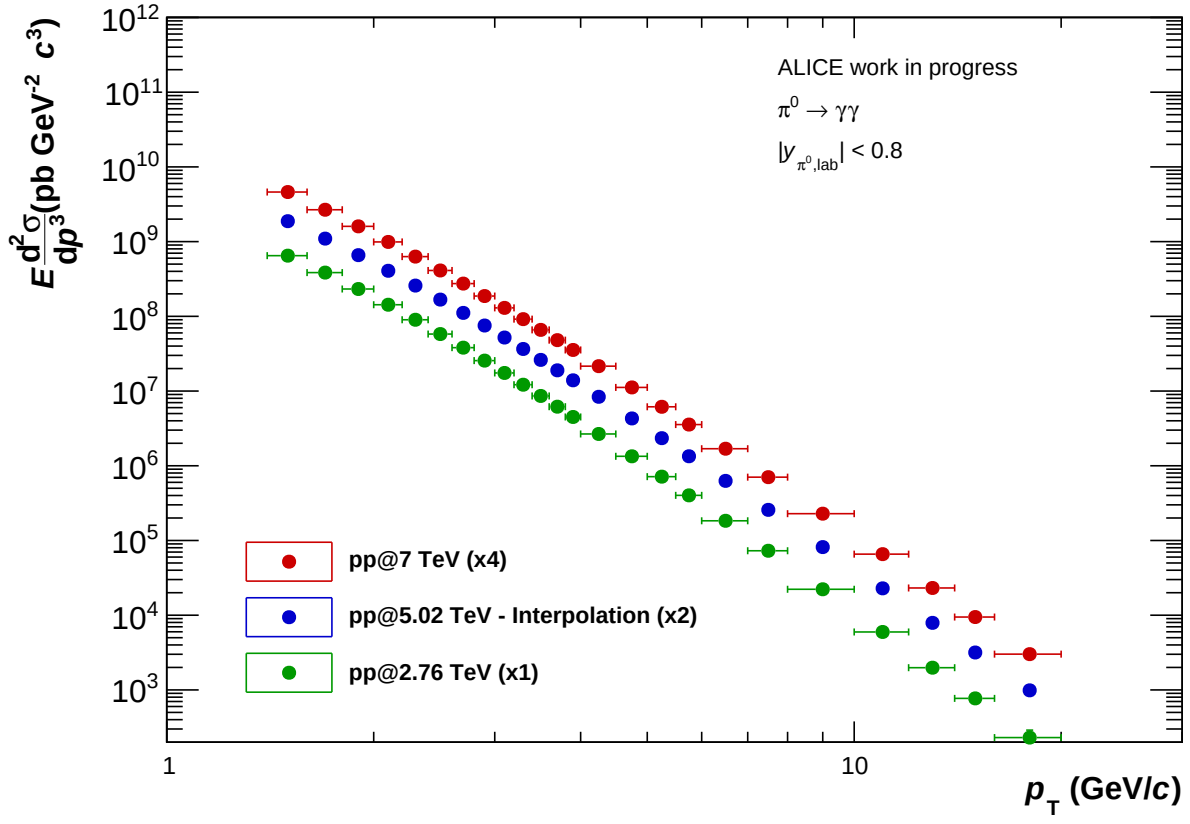

FIGURE 6.6: The pp reference and interpolated π^0 spectrum used to calculate the π^0 R_{p-Pb}.

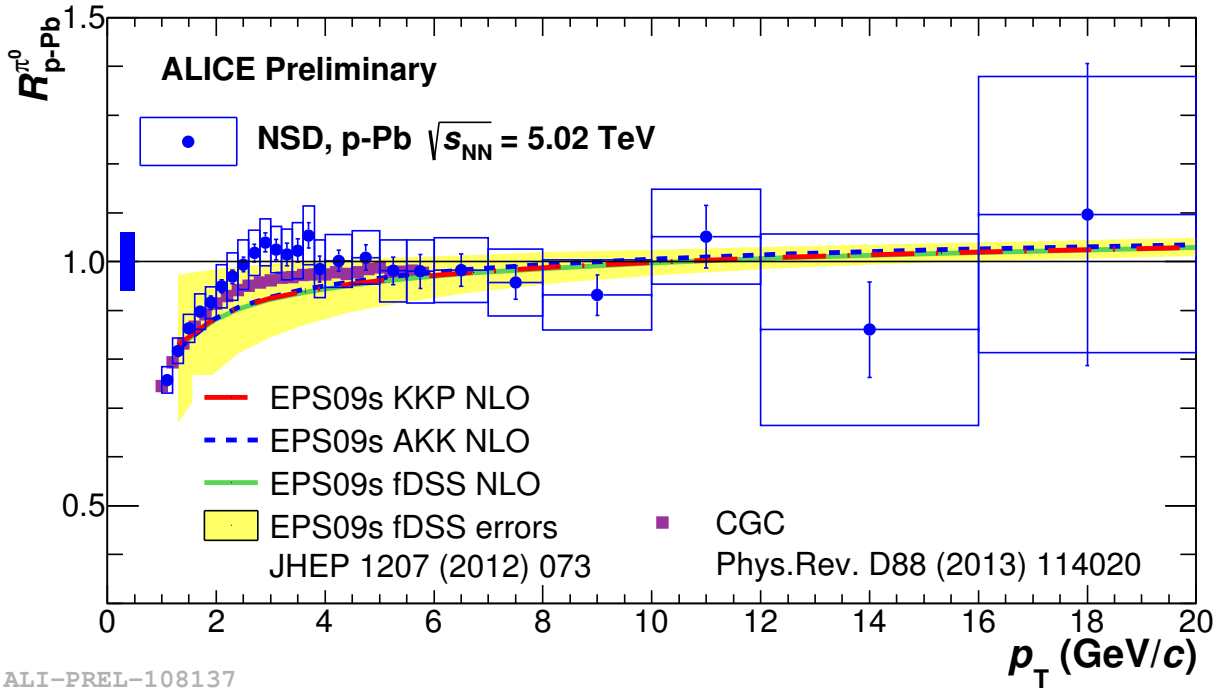

FIGURE 6.7: The π^0 R_{p-Pb} using the combined π^0 invariant cross section and reference spectrum.

Part II

Direct photons

Chapter 7

Impact of inclusive photon contamination

7.1 Sensitivity of the direct photon flow measurement

Direct photon flow is not measured directly, as it is currently impossible to suppress the background of decay photons. Therefore the direct photon flow coefficients are measured by subtracting the contribution of decay photon flow from the inclusive photon flow using R_γ . R_γ defines the excess of direct photons and is quantified by the double ratio:

$$R_\gamma \equiv \frac{\gamma_{inc}}{\pi^0} / \frac{\gamma^{decay}_{cocktail}}{\pi^0_{cocktail}} \approx \frac{\gamma_{inc}}{\gamma^{decay}_{cocktail}} \geq 1, \tag{7.1}$$

where the first term in the double ratio divides the measured inclusive photon spectrum(γ_{inc}) by the measured neutral pion spectrum (π^0). The second term is calculated with a cocktail simulation and divides the decay photon spectrum by the neutral pion spectrum. By construction, an excess of direct photons results in R_γ being greater than unity. The direct photon flow coefficient $v_2^{\gamma,\mathrm{dir}}$ is calculated by:

$$v_2^{\gamma,\mathrm{dir}}(p_\mathrm{T}) = \frac{R_\gamma(p_\mathrm{T}) v_2^{\gamma,\mathrm{inc}}(p_\mathrm{T}) - v_2^{\gamma,\mathrm{dec}}(p_\mathrm{T})}{R_\gamma(p_\mathrm{T}) - 1}. \tag{7.2}$$

This equation is based on the assumption that the inclusive photon sample consists of direct and decay photons, with no background contaminating the sample. However, it is impossible to have an inclusive photon sample which is free of contamination. And because R_γ is close to 1, and the inclusive and decay photon flow are both similar in magnitude, the extracted direct photon flow is extremely sensitive to small corrections to $v_2^{\gamma,\mathrm{inc}}$. A study has been performed to investigate exactly how sensitive the $v_2^{\gamma,\mathrm{dir}}$ measurement is, such that the effects of small inclusive photon contaminations can be estimated. This is done by using the ALICE preliminary results [11, 25]. The preliminary results for $v_2^{\gamma,\mathrm{inc}}$ and $v_2^{\gamma,\mathrm{dec}}$ and R_γ , shown in figure 7.1, have been measured using the photon conversion method in Pb-Pb collisions at $\sqrt{s_{NN}}$ = 2.76 TeV for

0–40% centrality. In order to reduce the effect of fluctuations in the subsequent calculation, the data are parametrized by a 3rd order polynomial for $v_2^{\gamma,\mathrm{inc}}$ and $v_2^{\gamma,\mathrm{dec}}$ and 2nd order polynomial for R_γ , respectively.

To be able to correct for the residual contamination one needs to know the v_2 of the various background sources. The v_2 for different contributions is additive, so one generally has $N^{\gamma,tot}v_2^{\gamma,tot} = N^{\gamma,inc}v_2^{\gamma,\mathrm{inc}} + N^{\gamma,bck}v_2^{\gamma,bck}$. Experimentally, one can not obtain an inclusive photon sample with 100% purity, i.e. 0% contamination (c), which implies that $v_2^{\gamma,tot} \neq v_2^{\gamma,\mathrm{inc}}$. However, if $c = N^{\gamma,bck}/\left(N^{\gamma,inc} + N^{\gamma,bck}\right)$ and $v_2^{\gamma,bck}$ are known, the $v_2^{\gamma,\mathrm{inc}}$ can be corrected using

$$v_2^{\gamma,\mathrm{inc}} = \frac{v_2^{\gamma,tot} - \sum_{i=0}^{n} v_2^{\gamma,bck,i} c^{\gamma,bck,i}}{1 - \sum_{i=0}^{n} c^{\gamma,bck,i}} \tag{7.3}$$

where i denotes all possible background sources ($1 \leq i \leq n$), which have to be estimated separately. If $c_i = 0$, there is no correction, as expected. However, if at least one $c_i > 0$, there will be a correction depending on the purity and the strength of the respective $v_2^{\gamma,bck,i}$. For photons reconstructed via conversion electrons, typical values for c at low p_T are about 5% [26] and 1% [6].

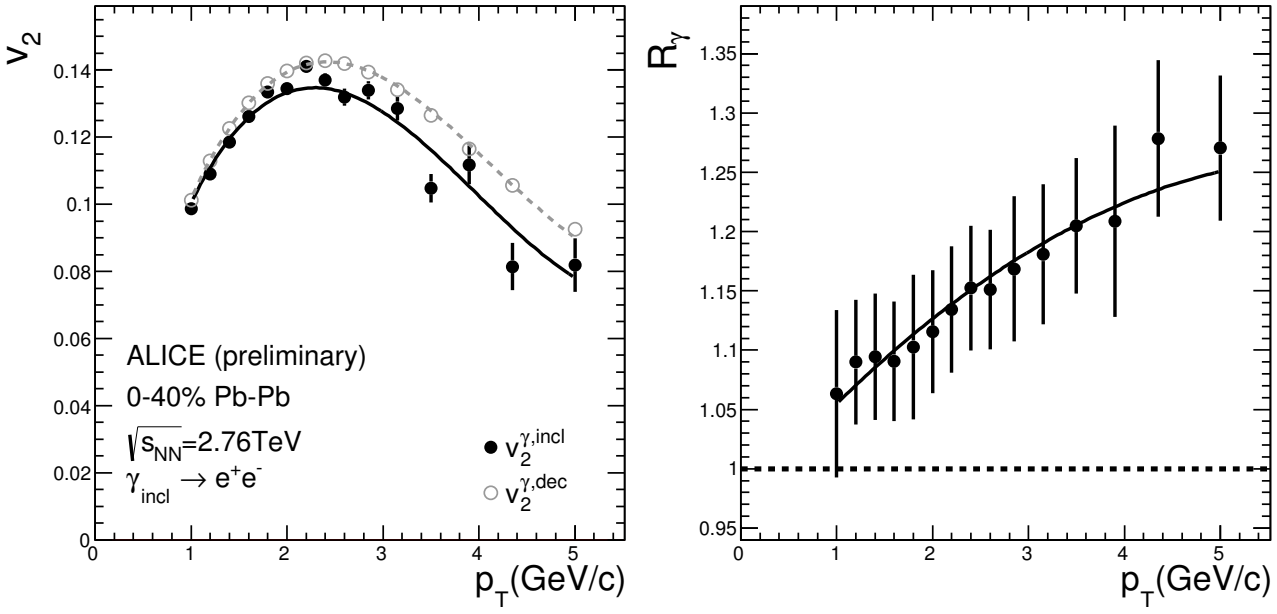

FIGURE 7.1: ALICE preliminary results for $v_2^{\gamma,\mathrm{inc}}$ and $v_2^{\gamma,\mathrm{dec}}$ (left panel) and R_γ (right panel) measured using the photon conversion method in 0–40% PbPb collisions at $\sqrt{s_{NN}} = 2.76$ TeV. The data are parametrized by a 3rd order polynomial for v_2 and 2nd order polynomial for R_γ to reduce the effect of fluctuations. The data points are from figure 4 in [11] and 5 in [25], respectively.

7.2 model of the inclusive photon background

In order to illustrate the effect that the purity correction from equation 7.3 may have on the inclusive and direct photon v_2, a toy model for $v_2^{\gamma,bck}$ has been constructed. It is assumed that $v_2^{\gamma,bck}$ gets a contribution

from charged pion flow, since in the photon conversion method the electrons are selected using $\mathrm{d}E/\mathrm{d}x$ information of the TPC. In particular at low p_{T} , the selection regions for electrons and pions overlap, and thus there are pions being misidentified as electrons. Since pions carry a v_2, a fake photon reconstructed from a $\pi^{\pm}$+$\mathrm{e}^{\mp}$ pair will do so as well. The same arguments holds for kaons and protons and their combinations. In addition, one also would expect a non-trivial effect from background e^{+}+e^{-} pairs. For the ALICE preliminary measurement the largest contribution to the combinatorial background are the e^{+}+e^{-}, closely followed by combinations of $\pi^{\pm}$+$\mathrm{e}^{\mp}$. These contributions only show a mild transverse momentum dependence, while others contribute mainly below 2 GeV/c, like p+$e^{\pm}$, $K^{\pm}$+$\mathrm{e}^{\mp}$, p+$\pi^{\pm}$. At high transverse momenta on the other hand charged pions are misidentified as electrons more often and thus the π^{+}+π^{-} contributions plays a larger role [27]. In reality, these contributions to the inclusive photon sample and their v_2 should be measured in data (or estimated using detector simulations) and subtracted.

Instead, here, the possible pair background is simulated using the event generator Therminator2 [28] in Pb-Pb collisions $\sqrt{s_{NN}}$ = 5.02 TeV for 0–40% centrality, employing (2+1)-dimensional boost-invariant hydrodynamics. The reaction plane is known from the generator output, and the particle v_2 can be calculated using the 3-momentum vectors. The single-particle v_2 results for π, K and p are shown in figure 7.2 and compared to the measured data [29] for 0–40% Pb-Pb collisions at $\sqrt{s_{NN}}$ = 2.76 TeV. The model reproduces the data reasonably well. Only for kaons at larger p_{T} substantial differences are observed.

Since without detector material the simulation does not contain converted electrons, the contributions from the pair v_2 for $\pi+\pi$, $K+\pi$ and $p+\pi$ systems is calculated by summing up the 3-vectors of the two particles. It can be assumed, that at least a fraction of the initial $v_2^{\pi^0}$, from which most electron will originate, will be carried by the electrons. Thus in order to obtain a first estimate on the possible final effects the $\pi+\pi$ serves as a decent description for the e^{+}+e^{-} contribution as well, though it will most likely underestimate the strength of the v_2 at low p_{T} . The pair v_2 results from the Therminator2 simulations are shown in figure 7.3, for pairs without any requirement on the opening angle ψ and with a cut of $\psi < \pi/16$. The latter cut is applied to mimic the conversion photon selection. As expected, a significant pair v_2 develops for both cases, and the values increase for the smaller opening angle. The effect observed resembles that caused by the coalescence mechanism [30, 31]. Stricter cuts on the opening angle select two particles, which are closer in phase space. In the construction of the pair the p_{T} of the single particles are combined. For small ψ this is equivalent to the sum. As a result, the pairs carry a stronger correlation at a higher p_{T} , similar to coalescence models.

The behaviour suggests that one might use the simple analytical scaling predicted by naïve coalescence models to calculate the pair v_2. Following this idea, the pair v_2 estimated from measured π, K and p v_2 data [29] is calculated as $v_2^{a+b}(p_{\mathrm{T}}) = v_2^{a}(p_{\mathrm{T}}/2) + v_2^{b}(p_{\mathrm{T}}/2)$ for particle species a and b. In addition, the same summation to the single particle v_2 generated by Therminator2 have been applied. For this purpose, the v_2 results were parameterized by a 3rd order polynomial for the experimental data and by a 5th order polynomial for Therminator2, as shown in figure 7.2.

The results for pair v_2 obtained by the two coalescence-like estimates are also shown in figure 7.3. All estimates of the pair v_2 are found to be qualitatively similar, with the coalescence estimates indicating rather a stronger effect. For the purpose of this study the Therminator2 model provides a reasonable description, despite the fact that the model does not perfectly describe the data. For the following study, the parameterization of pair v_2 coefficients from Therminator2 is used with an opening angle cut of $\psi < \pi/16$, when applying the purity correction in equation 7.3.

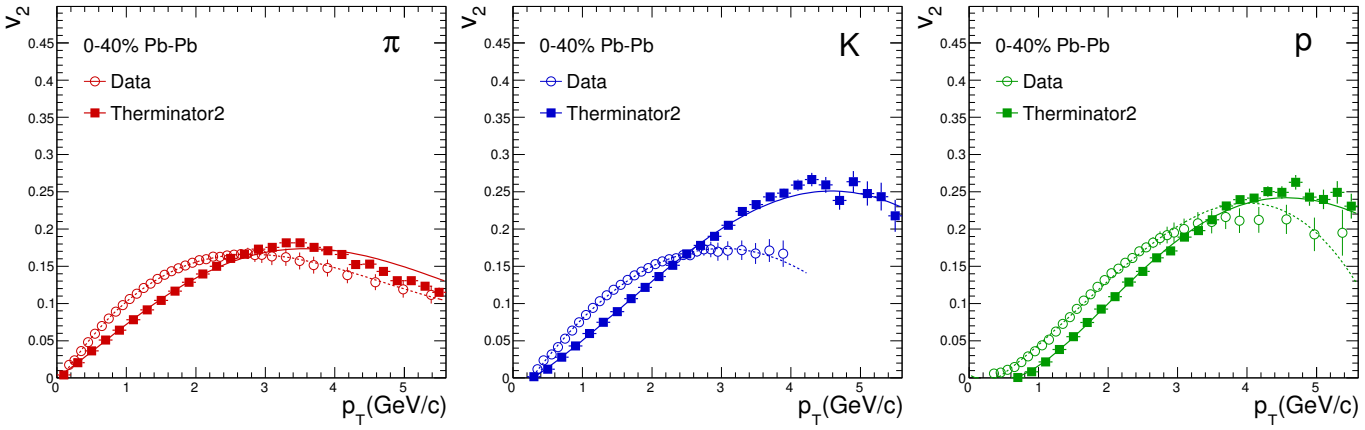

FIGURE 7.2: Single particle v_2 as a function of p_{T} for π, K and p calculated using Therminator2 [28] and compared to the measured data [29] for 0–40% Pb-Pb collisions at $\sqrt{s_{NN}} = 2.76$ TeV. Fits to both sets of results are also included. For the experimental data the fit uses a 3rd and for Therminator2 a 5th order polynomial.

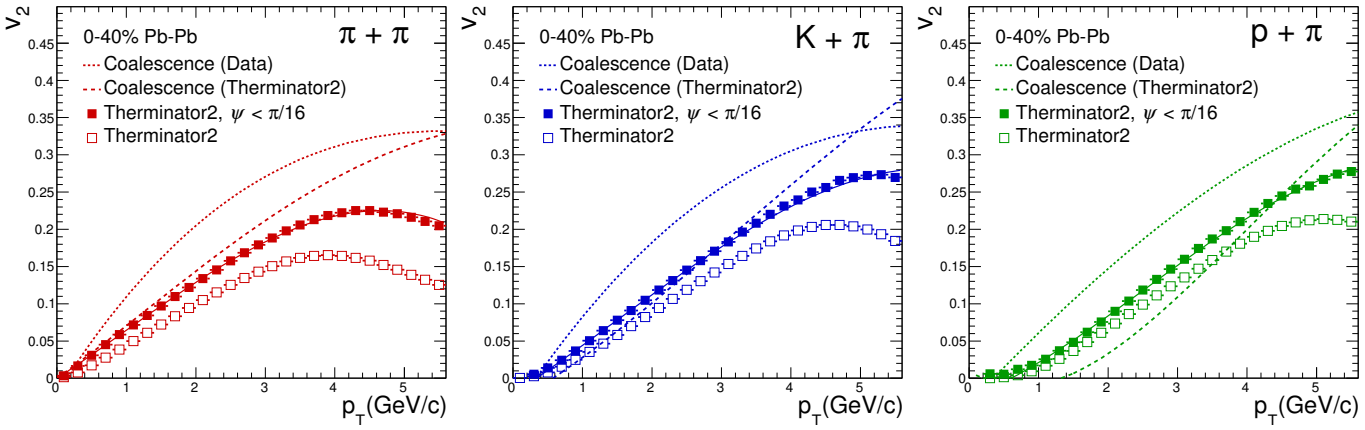

FIGURE 7.3: Pair v_2 as a function of p_{T} simulated with Therminator2 (symbols) and derived from single-particle v_2 using a simple coalescence model. The pair v_2 is calculated for $\pi+\pi$, $K+\pi$ and $p+p$ systems and parametrized by a 3rd order polynomial. The Therminator2 calculations are performed either without any opening angle cut (open symbols) or with a cut of $\pi/16$ (filled symbols). The coalescence type estimates use as input a parametrization of either the data (dotted line) or of the single particle results from Therminator2 (dashed line).

7.3 Toy model results

In this section, the inclusive photon flow $v_2^{\gamma,\mathrm{inc}}$ shown in figure 7.1 is corrected using equation 7.3 for different assumptions of $v_2^{\gamma,bck}$, shown in figure 7.3, and purity. The direct photon flow $v_2^{\gamma,\mathrm{dir}}$ is calculated

for the uncorrected and background corrected $v_2^{\gamma,\mathrm{inc}}$ using equation 7.2. Figure 7.4 illustrates the effect of background v_2 corrections on inclusive and direct photon flow for different assumptions on the type of background. A p_T independent inclusive photon sample purity of 97% is assumed, i.e. a contamination of $c = 3\%$ originating from $\pi+\pi$, $K+\pi$ and $p+\pi$ pair v_2, respectively, is considered. As may be expected, the effects on inclusive photon v_2 are moderate, between +2% and −8%. The effect on the direct photon flow, however, is considerable, between +60% and up to −90% depending on p_T and the type of background. The differences for the different particle species contributing to the background are again rather moderate, obviously because the differences between the assumed pair v_2 are also rather small. In our calculations the shift from the correction is positive at low p_T and becomes negative at high p_T .

A straightforward next step is the study of the dependence of the correction on the strength of the contamination, as shown in figure 7.5. Here, only the shape of the $\pi+\pi$ pair v_2 is used as $v_2^{\gamma,bck}$, but different levels of contamination of $c = 1$, 3 and 5%, respectively, are assumed. This leads to slightly stronger effects, in particular for $c = 5\%$. For inclusive photon v_2 effects are between +2% and −10%, for direct photons between +50% and up to −120%. For $c = 3\%$ and restricting to about 3 GeV/c the effect on $v_2^{\gamma,\mathrm{dir}}$ is about 50%.

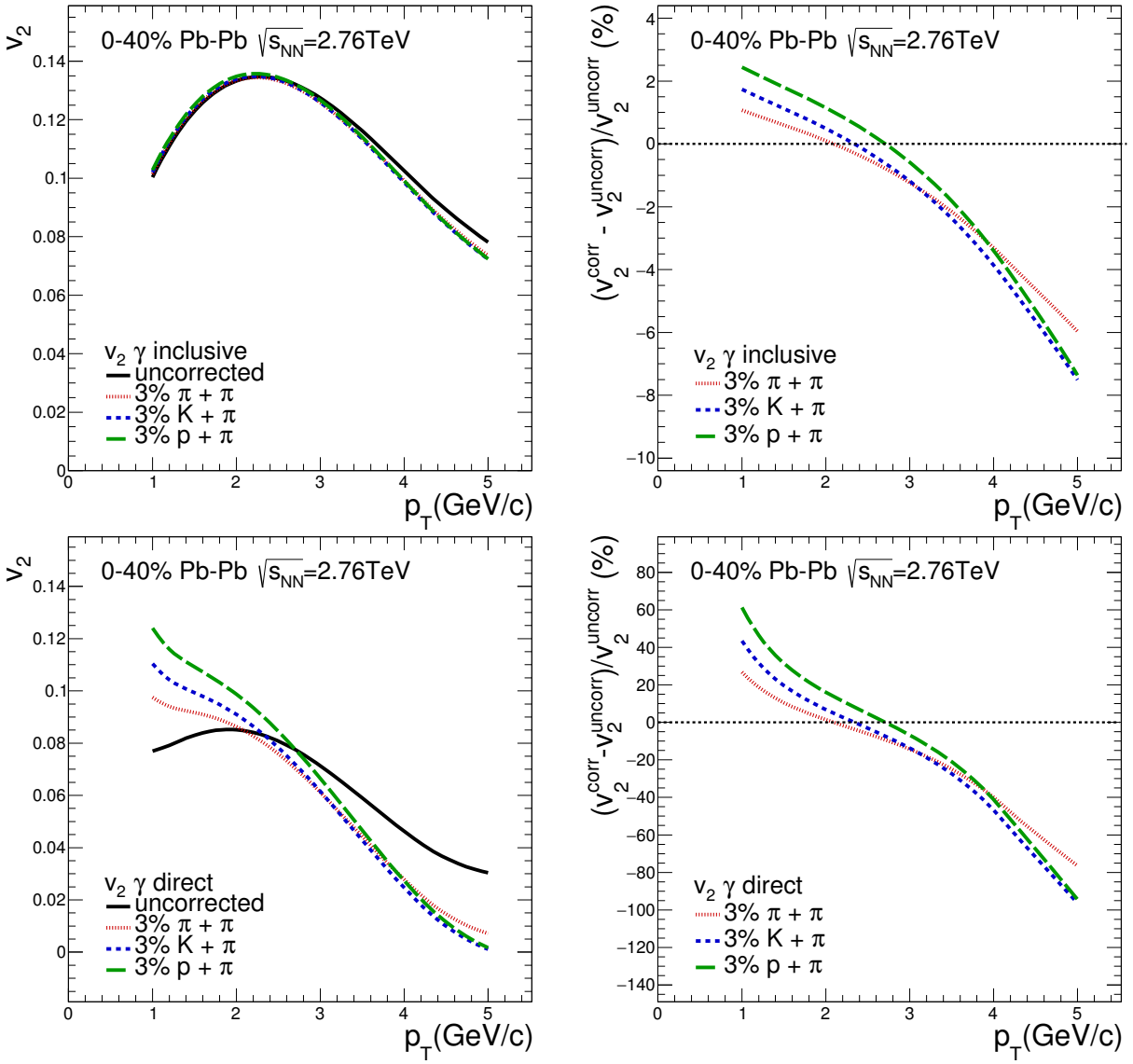

FIGURE 7.4: Results of $v_2^{\gamma,\mathrm{inc}}$ (top left panel) and $v_2^{\gamma,\mathrm{dir}}$ (bottom left panel) using equation 7.3 to correct for $\pi+\pi$, $K+\pi$ and $p+\pi$ contamination with $c = 3\%$. The deviations (in %) from the uncorrected $v_2^{\gamma,\mathrm{inc}}$ and $v_2^{\gamma,\mathrm{dir}}$ are shown in the corresponding panels on the right.

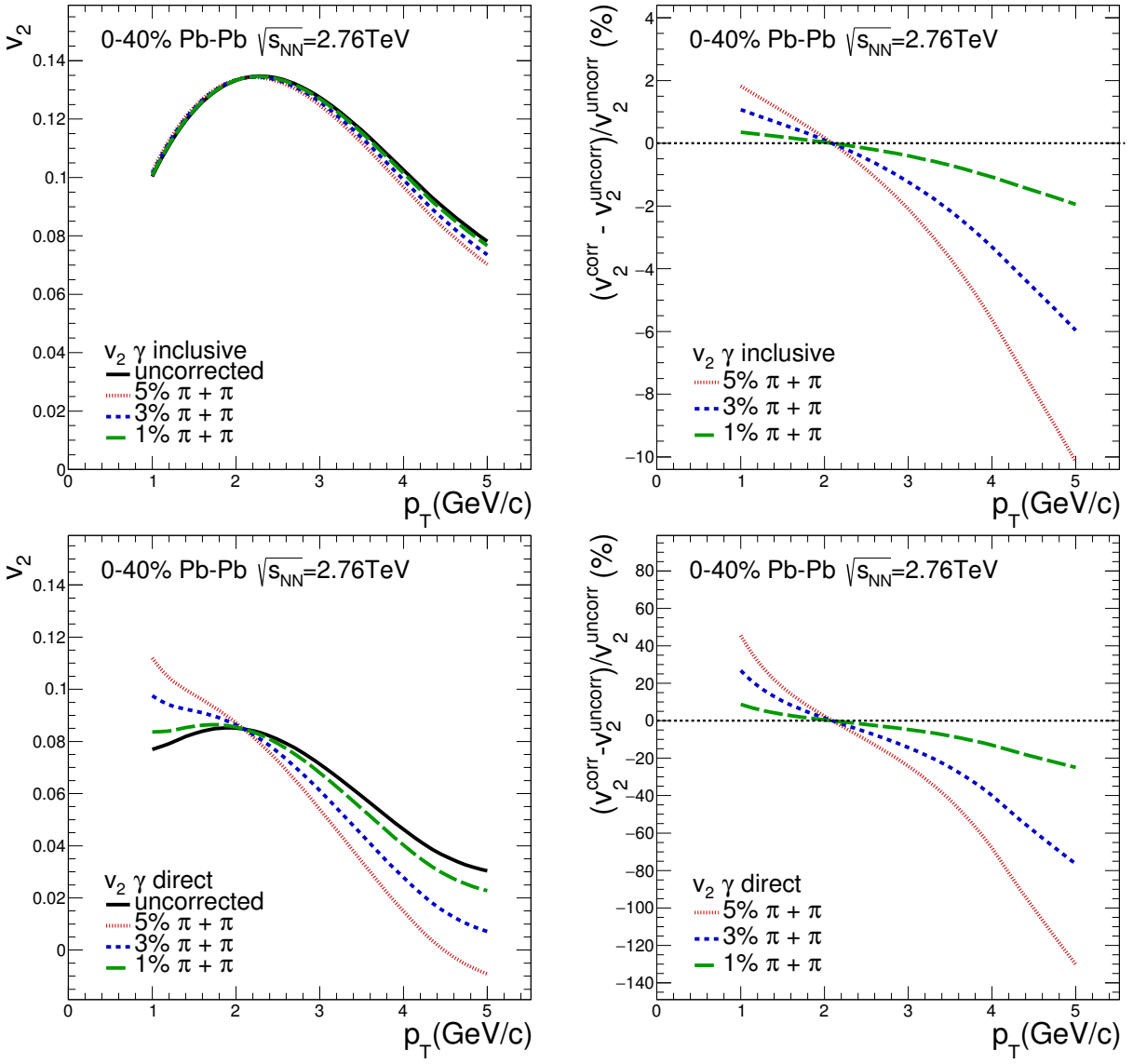

FIGURE 7.5: Results of $v_2^{\gamma,\mathrm{inc}}$ (top left panel) and $v_2^{\gamma,\mathrm{dir}}$ (bottom left panel) using equation 7.3 to correct for $\pi + \pi$ with $c = 1$, 3 and 5%. The deviations (in %) from the uncorrected $v_2^{\gamma,\mathrm{inc}}$ and $v_2^{\gamma,\mathrm{dir}}$ are shown in the corresponding panels on the right.

Chapter 8

Inclusive and decay photon flow

The inclusive photon flow, $v_2^{\gamma,\mathrm{inc}}$, is calculated for Pb-Pb collisions at $\sqrt{s_{NN}} = 2.76$ TeV using the photons of the inclusive photon sample, which are reconstructed using the photon conversion method. This chapter describes the correction to $v_2^{\gamma,\mathrm{inc}}$, using a detailed study of the purity of the photon sample. The results of the inclusive photon flow $v_2^{\gamma,\mathrm{inc}}$ is presented together with the decay photon flow $v_2^{\gamma,\mathrm{dec}}$.

8.1 Scalar Product method

One of the first experimental techniques to measure the elliptic flow in heavy ion collisions is the "event plane method", which involves the reconstruction of the reaction plane for each event. However, it has been shown that that there is an ambiguity in the measured v_2 using the event plane method due to the dependence on detector resolution.
With the "Scalar Product method"(SP method) it is possible to measure the elliptic flow without the reconstruction of the reaction plane angle Ψ_R and uses two-particle correlations. This has the advantage that there is no correction needed for the event plane resolution.
In this analysis the SP method with three sub-events is used. The sub-events have different pseudo-rapidity regions and are used to remove auto-correlations and suppresses non-flow contributions. The "Particles Of Interest"(POI's), belonging to sub-event A, are reconstructed in the TPC with $|\eta| < 0.9$. The "Reference Flow Particles"(RFP's), belonging to sub-events B and C, are measured with the VZERO-A and VZERO-C detectors, respectively. The pseudo-rapidity gap of $|\eta| > 0.9$ between the POI's and RFP's is large enough to suppress the non-flow contributions.

The flow vector $\overrightarrow{Q}_n$ is defined as:

$$\overrightarrow{Q}_n = \sum_{i=1}^{N} w_i e^{ni\varphi_i} \tag{8.1}$$

With w_i the weight assigned to particle i and φ_i the azimuthal angle of particle i. The elliptic flow coefficient v_n is calculated by:

$$v_n = \sqrt{\frac{\langle \overrightarrow{u}_n^A \cdot \frac{\overrightarrow{Q}_n^B}{M_B} \rangle \langle \overrightarrow{u}_n^A \cdot \frac{\overrightarrow{Q}_n^C}{M_C} \rangle}{\langle \frac{\overrightarrow{Q}_n^B}{M_B} \cdot \frac{\overrightarrow{Q}_n^C}{M_C} \rangle}} \tag{8.2}$$

Where $\overrightarrow{u}_n^A$ is the unit vector of the POI in sub-event A. M_B and M_C are the event multiplicities measured with the VZERO-A and VZERO-C detectors, respectively. as before, $\langle ... \rangle$ denotes the average over particles and events.

In addition, "Non-Uniformity and Acceptance"(NUA) corrections can be applied to the extracted v_2 of the inclusive photon sample. The result for $v_2^{\gamma,\text{inc}}$ (NUA-ON)/$v_2^{\gamma,\text{inc}}$ (NUA-OFF) is shown in figure 8.1. It shows that these corrections, for low transverse momentum, are of the order of 0.1% for central collisions and increase to about 0.2% for more peripheral collisions. This correction is much smaller than the statistical uncertainty and are thus neglected.

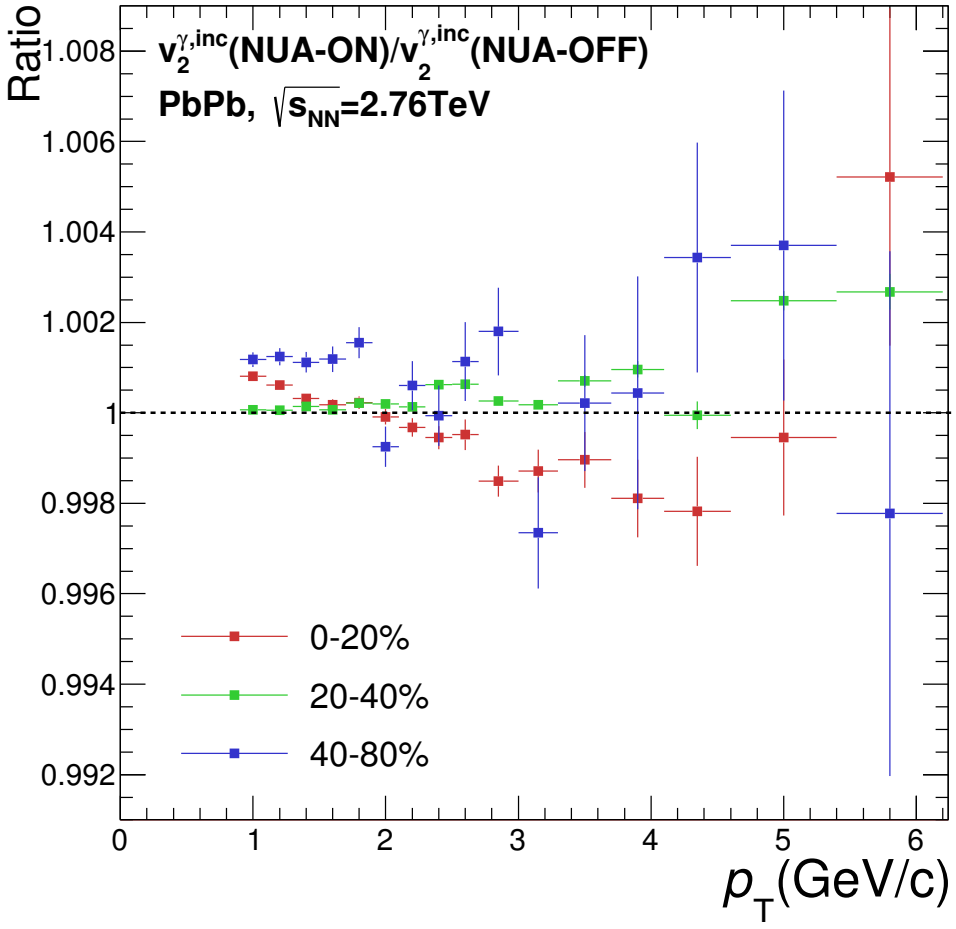

FIGURE 8.1: The effect of having non-uniformity and acceptance corrections for $v_2^{\gamma,\text{inc}}$ for the centrality classes $0-20\%$, $20-40\%$ and $40-80\%$.

8.2 Purity of the inclusive photon sample

Photons reconstructed with the photon conversion method are not necessarily real photons converting into an electron and positron pair. This is mainly due to the fact that the selection criteria for electrons and positrons are not perfect. It is possible that, for example, a $\pi^{\pm}$ is identified as an electron. This results in a fake photon in the inclusive photon sample.

A way to investigate the purity of the inclusive photon sample is by using the energy loss of the daughter particles in the TPC. Charged particles traversing the TPC have a characteristic energy loss dependent on momentum and type of particle, as shown in figure 8.2(left). This quantity can be related to the average response of the electron in the TPC, by calculating the number of standard deviations the response of the candidate is removed from the fitted electron response and is labelled as $n\sigma_{e^{\pm}}$. The $n\sigma_{e^{\pm}}$ for secondary particles is shown in figure 8.2(right). For certain momentum ranges the energy loss can become similar for different particles, which shows that there are background sources in the electron sample.

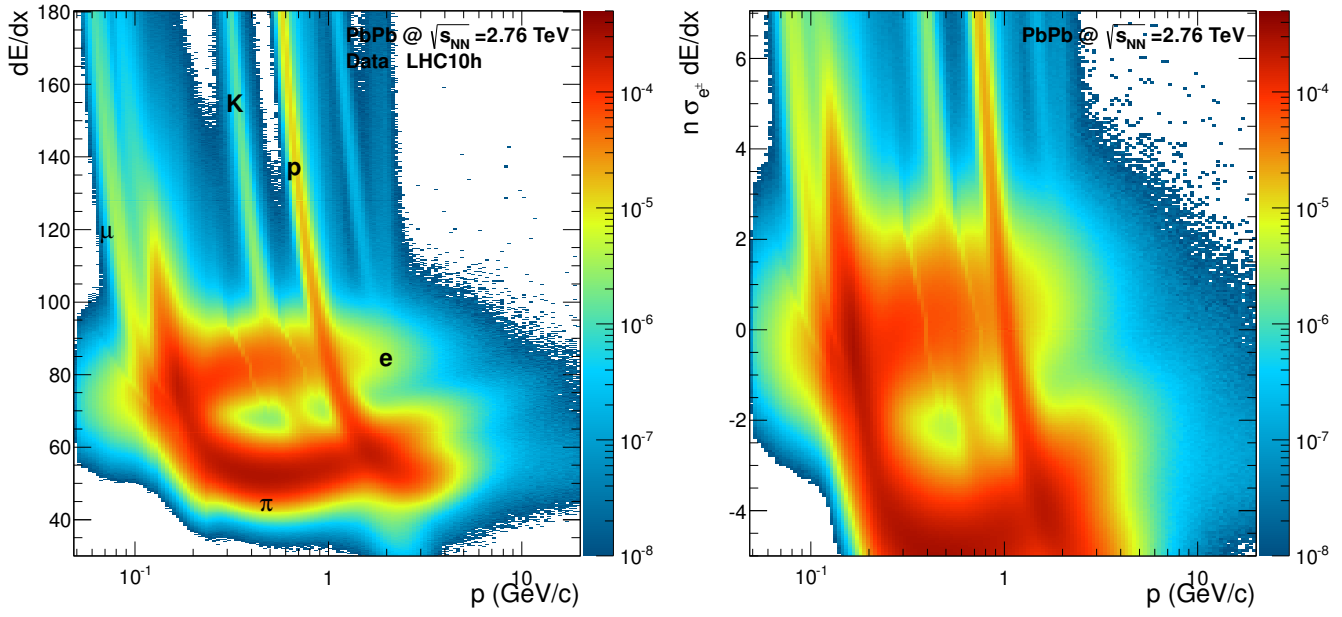

FIGURE 8.2: The energy loss per unit distance(left) and the number of standard deviations from the average electron response(right) of a particle traversing the TPC as function of transverse momentum.

To study the different background sources for conversions, first $n\sigma_{e^{\pm}}$ is relabelled to $\kappa^{\pm}$. It is defined as:

$$\kappa^{\pm} \equiv \frac{\frac{dE}{dx}\mid_{candidate} - \langle \frac{dE}{dx}\mid_{electron} \rangle}{\sigma_{\langle \frac{dE}{dx}\mid_{electron} \rangle}} \tag{8.3}$$

Where κ^{+} is for the positively charged conversion daughter and κ^{-} for the negatively charged conversion daughter. Real electrons and positrons will be centered around $\kappa^{\pm} \simeq 0$ with a width equal to the spread in $\frac{dE}{dx}\mid_{TPC}$. Fake photons reconstructed using a real pion and electron will have displaced peaks since the

response of a pion in the TPC is different, on average. An overview of the signal and background contributions to the inclusive photon sample is shown in figure 8.3 for a single p_{T} slice, where κ^+ is plotted versus κ^-. This is done to investigate which regions are signal or background dominated by each source. This result is p_{T} dependent because the TPC response is p_{T} dependent, but the general features remain the same.

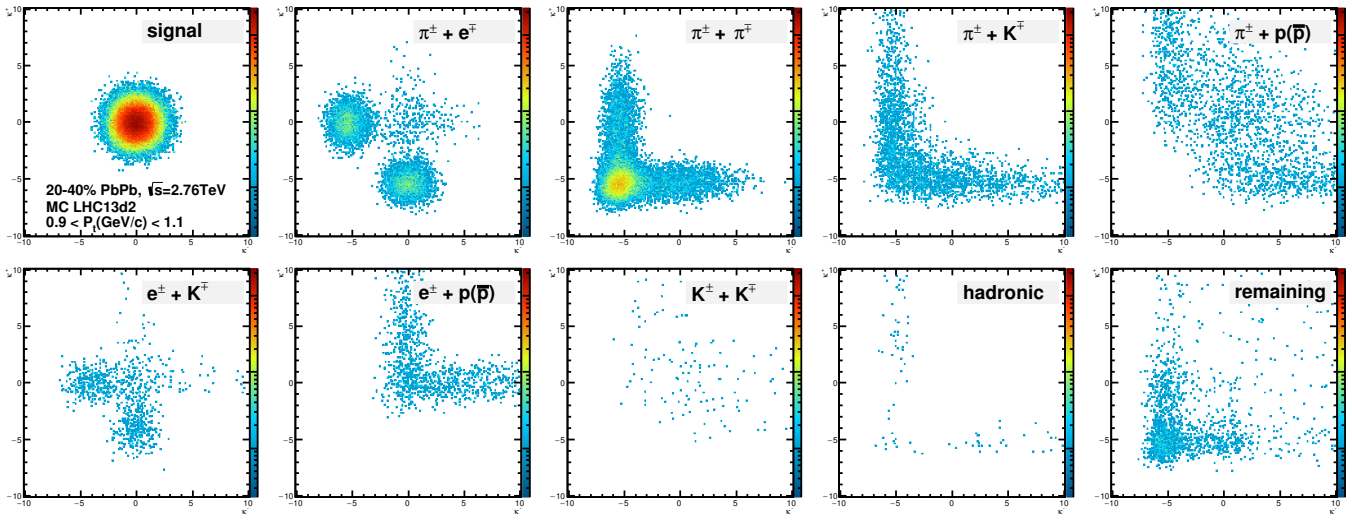

FIGURE 8.3: Signal and background contributions to the inclusive photon sample plotted with κ^+ versus κ^-.

From κ^+ and κ^- a single variable is constructed:

$$K = \frac{|\kappa^+| + |\kappa^-|}{2} + 2(\kappa^+ + \kappa^-) \tag{8.4}$$

The first term combines the absolute values of κ^+ and κ^-, giving both signal and background a characteristic average value. The second term exploits the asymmetric response of positively and negatively charged particles in the TPC. For example, $\gamma_{fake} \rightarrow \pi + e$ has a strong negative component from the pion for low p_{T} .

As can be seen in figure 8.4 and figure 8.5, each background source has a response that can be discriminated from the others. There are three main background sources; $\gamma_{fake} \rightarrow \pi^{\pm} + \pi^{\mp}$, $\gamma_{fake} \rightarrow \pi^{\pm} + e^{\mp}$ and γ_{fake} →remaining, where remaining is a collection of all other background sources. Real e^+e^- pairs are centered around $K \simeq 0$ with a slightly longer tail to positive values of K. $\gamma_{fake} \rightarrow \pi^{\pm} + e^{\mp}$ are centered around $K \simeq -8$ because of the average response of the pion. $\gamma_{fake} \rightarrow \pi^{\pm} + \pi^{\mp}$ are centered around $K \simeq -16$ because of the response of two pions. γ_{fake} →remaining is reasonably flat in K because it consists of many different particles with different TPC responses.

The purity of the inclusive photon sample is estimated by fitting the four MC templates(figure 8.4) on the total response of data and calculating:

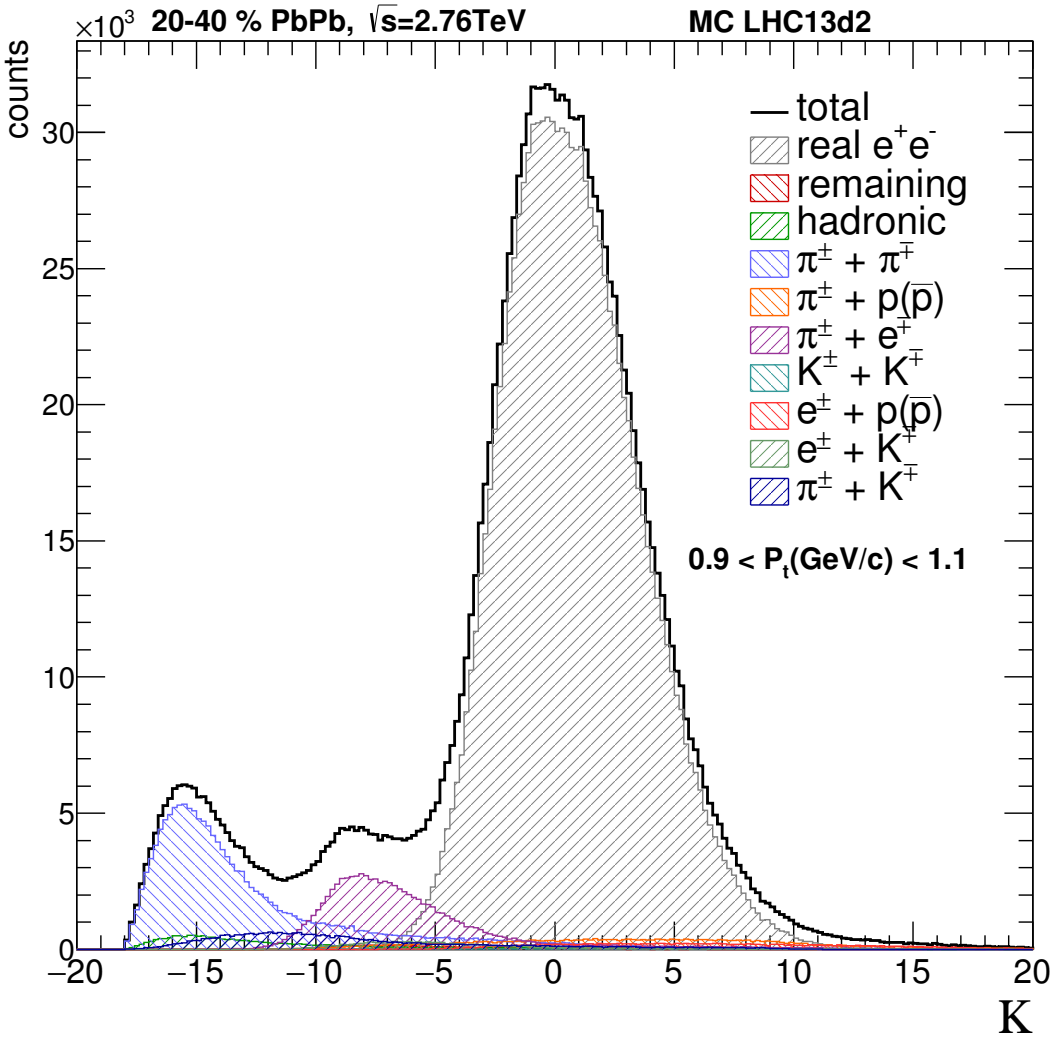

FIGURE 8.4: K distributions conversion photon candidates where MC information is used to classify the conversion daughters.

$$p = \frac{N_{signal}}{N_{signal} + N_{background}} \tag{8.5}$$

Where N_i is obtained by counting bins in a region in K. The purity can be enhanced by selecting regions in $\frac{dE}{dx}\,|_{TPC}$. $-3 < K < 5$ is optimal for selecting signal and has a purity of $p > 86\%$ for all centrality classes. The amount of contamination in the inclusive photon sample is calculated by $c = 1 - p$. The contamination for each background source separately is calculated by:

$$c_i = \frac{N_{background,i}}{N_{signal} + N_{background}} \tag{8.6}$$

The results for the purity and contaminations of the inclusive photon sample are shown in figure 8.6 and figure 8.7, respectively, for centralities $0 - 20\%$, $20 - 40\%$ and $40 - 80\%$.

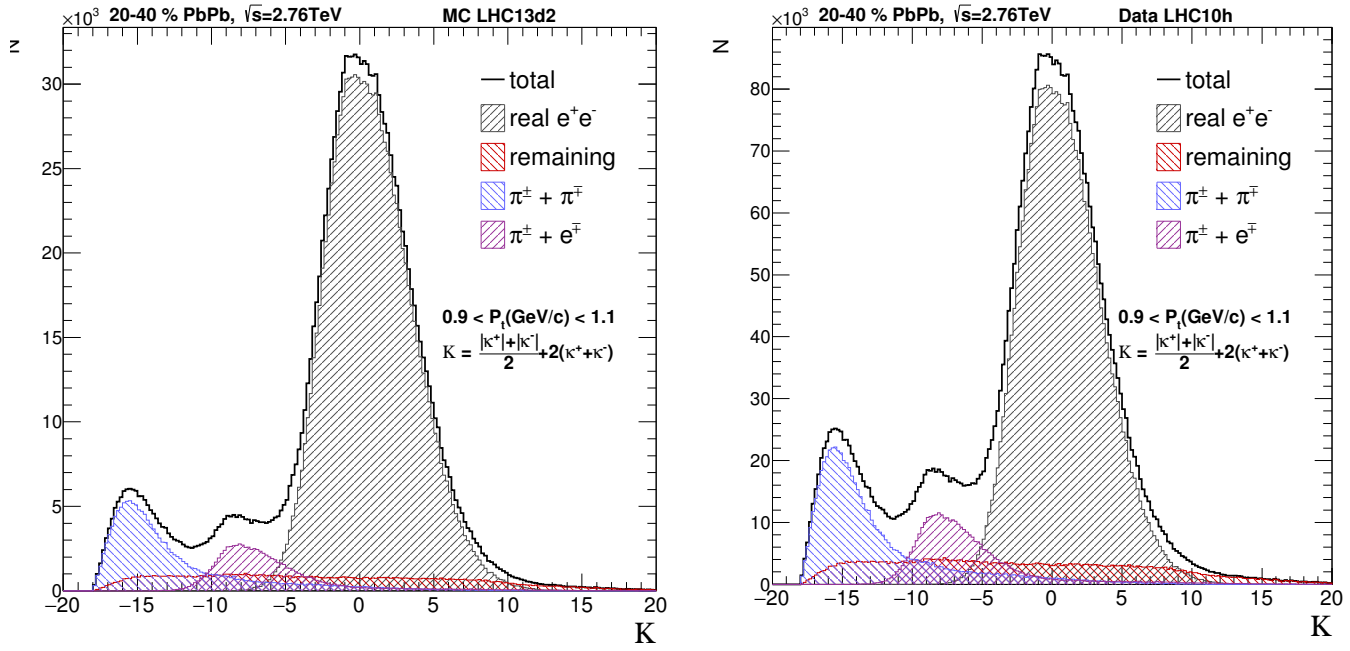

FIGURE 8.5: K distributions for signal and background sources for conversion photon candidates using 4 MC templates. The distributions in the left plot are obtained by using MC information to classify the source of the reconstructed photon. These distributions are the MC templates used for the fit on data and are different for each p_{T} bin. The distributions on the right are obtained by fitting the MC templates on data in which all templates are scaled to best fit the data.

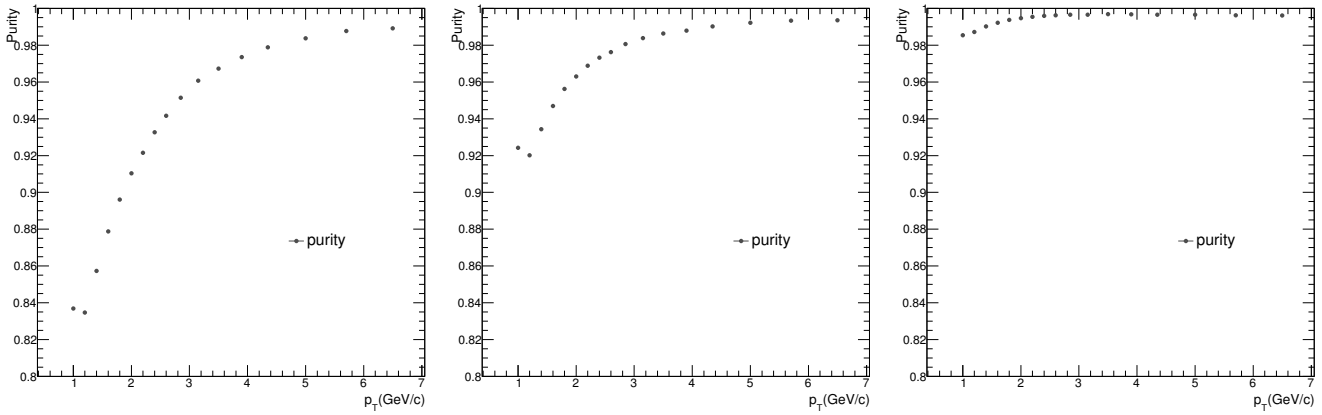

FIGURE 8.6: Purity of the inclusive photon sample for centralities $0-20\%$, $20-40\%$ and $40-80\%$. The purity is obtained by fitting MC templates of the K distributions on data and integrating the resulting distribution in the region $-3 < K < 5$.

Fake photons reconstructed from electron-positron combinatorics form a background source that is indistinguishable from real conversion photons. This background is reduced as much as possible by applying strict topological cuts. Since this background consists of electron positron combinations, the response in the TPC is the same as for real conversion electrons. This means that a selection in K does not supply any additional discriminating power. The fake photons from electron positron combinatorics can be studied using Monte-Carlo information and the results are shown in figure 8.8. It shows that for the momentum bin ($0.9 < p_{\mathrm{T}} < 1.1$) the contamination is at its maximum and is located under the main signal peak with

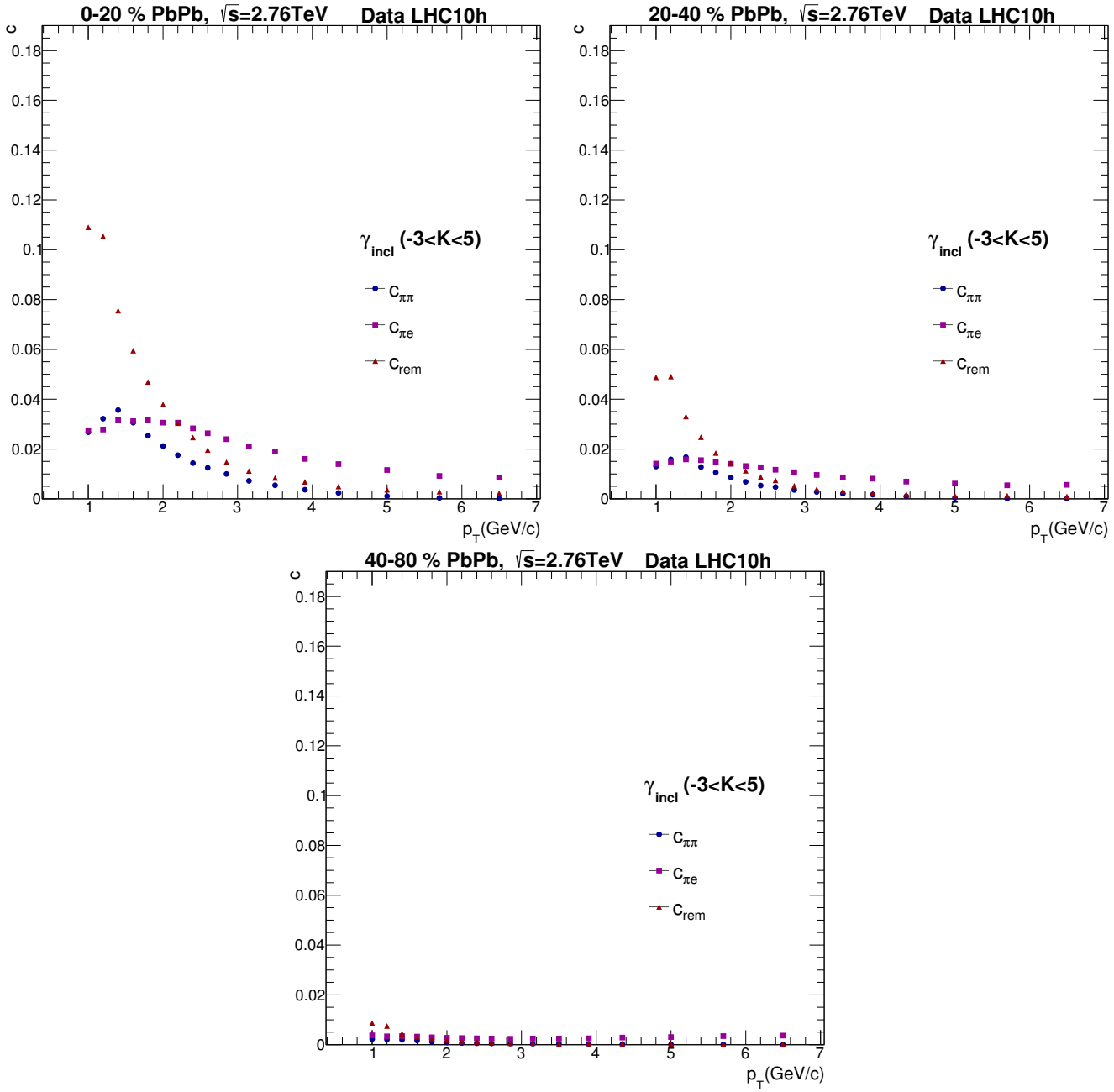

FIGURE 8.7: Contamination of the inclusive photon sample for centralities $0-20\%$, $20-40\%$ and $40-80\%$. The different contaminations are obtained by fitting MC templates of the K distributions on data and integrating the scaled MC templates in the region $-3 < K < 5$.

$c_{e^+e^-} \sim 1.9\%$ for centrality $0-20\%$. For centralities $20-40\%$ and $40-80\%$ the maximum contamination decreases to $c_{e^+e^-} \sim 1.2\%$ and $c_{e^+e^-} \sim 0.54\%$, respectively. This is mainly because the track multiplicities for low transverse momentum and central collisions is higher, and thus the amount of combinatorics increases. Because the track multiplicities are similar in data and MC, it is assumed that the background from electron-positron combinatorics is similar in data.

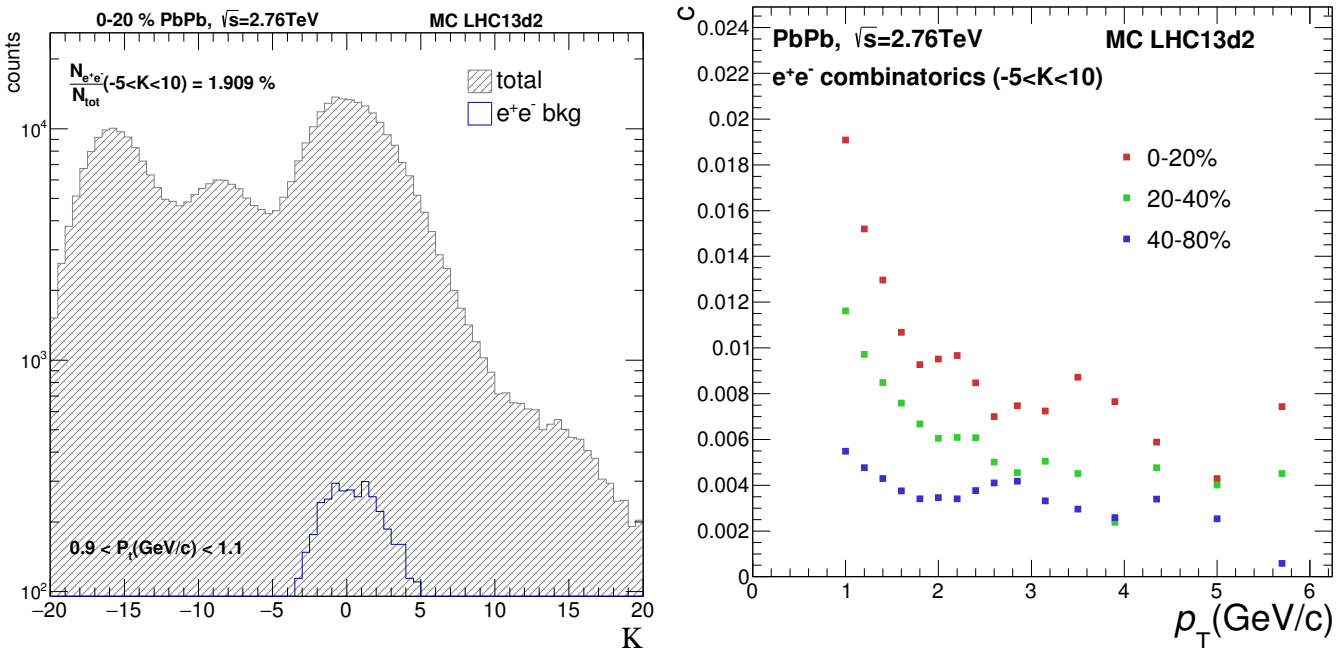

FIGURE 8.8: Contamination from electron-positron combinatorics for a single p_{T} slice as function of K(left) and as function of p_{T} for different centrality classes(right).

8.3 Inclusive photon flow correction method

The effect of background contaminating $v_2^{\gamma,\text{inc}}$ depends on the purity of the inclusive photon sample and the strength of the background flow $v_2^{\gamma,\text{bck}}$. The measured v_2 contains contributions from both signal and background sources and is given by:

$$N_\gamma^{candidate} v_2^{\gamma,candidate} = N_\gamma^{inc} v_2^{\gamma,inc} + N_\gamma^{bck} v_2^{\gamma,bck} \tag{8.7}$$

There is no direct way of measuring $v_2^{\gamma,\text{bck}}$ in the main signal region $(-3 < K < 5)$. However, as shown in figure 8.4, the background sources extent further in K and each dominate in a certain region. It is therefore possible to measure $v_2^{\gamma,\text{bck}}$ in different regions and calculate v_2^{rem}, $v_2^{\pi\pi}$ and $v_2^{\pi e}$, from which the $v_2^{\gamma,\text{bck}}$ can be reconstructed. This is under the assumption that v_2 is not K dependent for one given component. The three background regions are defined as:

- Region 1: $(-18 < K < -13)$
- Region 2: $(-11 < K < -6)$
- Region 3: $(11 < K < 20)$

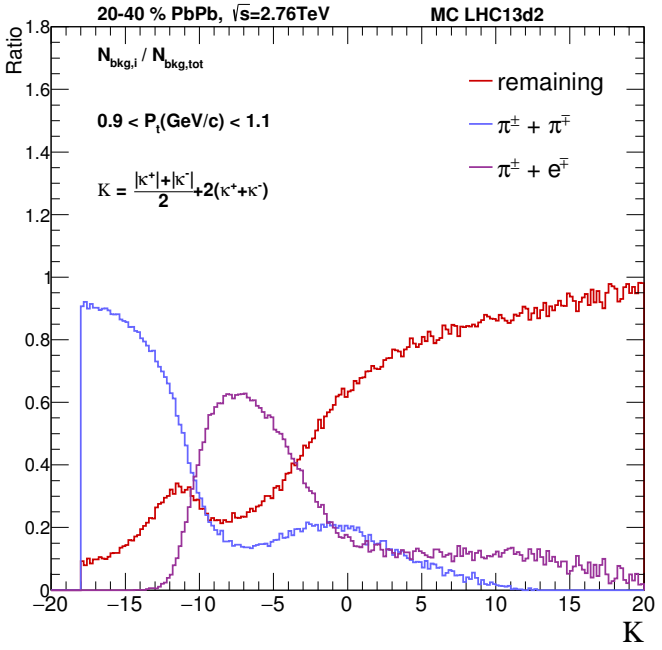

FIGURE 8.9: Ratio of background sources to the total background as function of K.

Which, as shown in figure 8.9, are each dominated by a different background source. Measurements of v_2 for region 1, 2 and 3 can be related to v_2^{rem}, $v_2^{\pi\pi}$ and $v_2^{\pi e}$ by knowing the relative contributions of all background

sources in each region. The relative contribution of a background source to the total background in a specific region is defined by:

$$n_i = \frac{N_i}{\sum_j N_j} \tag{8.8}$$

With $N_i = \{N_{rem}, N_{\pi\pi}, N_{\pi e}\}$. This also implies $\sum_i n_i = 1$ as required. The results for $v_2^{region1}$, $v_2^{region2}$ and $v_2^{region3}$ are shown in figure 8.10 for centralities $0-20\%$, $20-40\%$ and $40-80\%$.

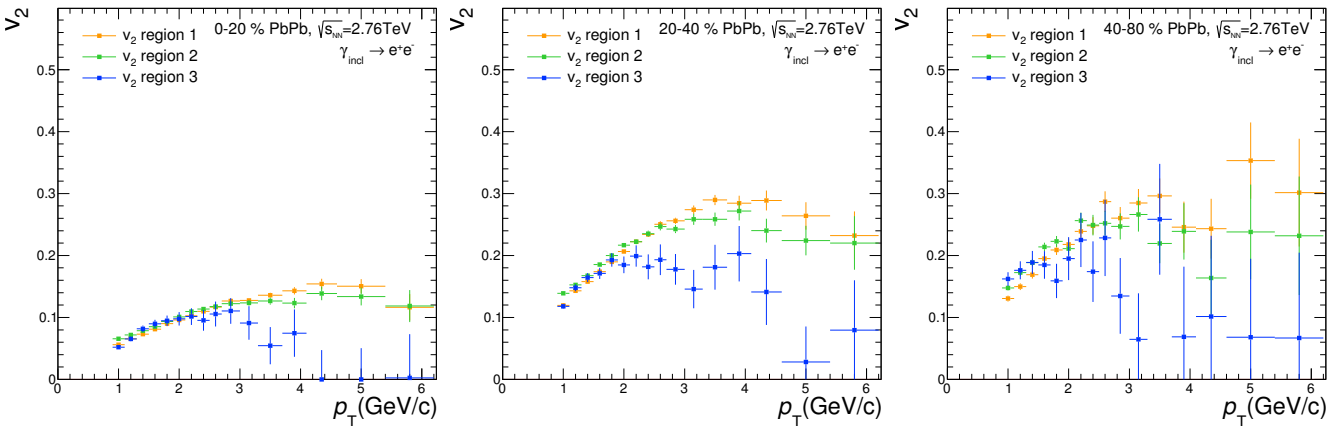

FIGURE 8.10: $v_2^{region1}$, $v_2^{region2}$ and $v_2^{region3}$ as function of p_{T} for centralities $0-20\%$, $20-40\%$ and $40-80\%$.

Region 3 is completely dominated by $\gamma_{fake} \to rem$. As shown in figure 8.9, it is reasonable to assume that:

$$v_2^{region3} = v_2^{rem}. \tag{8.9}$$

Region 1 is mostly dominated by $\gamma_{fake} \to \pi^{\pm}\pi^{\mp}$, and there is an additional background contribution from $\gamma_{fake} \to rem$. Therefore, the measured $v_2^{region1}$ consists of:

$$v_2^{region1} = n_{rem} v_2^{rem} + n_{\pi\pi} v_2^{\pi\pi} \tag{8.10}$$

The transverse momentum dependent n_{rem} and $n_{\pi\pi}$ results from MC template fits on data are shown in figure 8.11(left). Solving for $v_2^{\pi\pi}$ gives:

$$v_2^{\pi\pi} = \frac{v_2^{region1} - n_{rem} v_2^{rem}}{n_{\pi\pi}} \tag{8.11}$$

Region 2 contains contributions from all three background sources. Therefore, the measured $v_2^{region2}$ consists of:

$$v_2^{region2} = n_{rem} v_2^{rem} + n_{\pi\pi} v_2^{\pi\pi} + n_{\pi e} v_2^{\pi e} \tag{8.12}$$

The p_T dependent n_{rem}, $n_{\pi\pi}$ and $n_{\pi e}$ results obtained from MC template fits on data are shown in figure 8.11(middle). Solving for $v_2^{\pi e}$ gives:

$$v_2^{\pi e} = \frac{v_2^{region1} - n_{rem} v_2^{rem} - n_{\pi\pi} v_2^{\pi\pi}}{n_{\pi e}} \tag{8.13}$$

The n_{rem}, $n_{\pi\pi}$ and $n_{\pi e}$ values, as shown in figure 8.11(right), are calculated in the signal region ($-3 < K < 5$) to construct $v_2^{\gamma,\mathrm{bck}}$:

$$v_2^{\gamma,\mathrm{bck}} = n_{rem} v_2^{rem} + n_{\pi\pi} v_2^{\pi\pi} + n_{\pi e} v_2^{\pi e}. \tag{8.14}$$

The results for $v_2^{\pi\pi}$, $v_2^{\pi e}$, v_2^{rem} and $v_2^{\gamma,\mathrm{bck}}$ are shown in figure 8.12, for centralities $0-20\%$, $20-40\%$ and $40-80\%$.

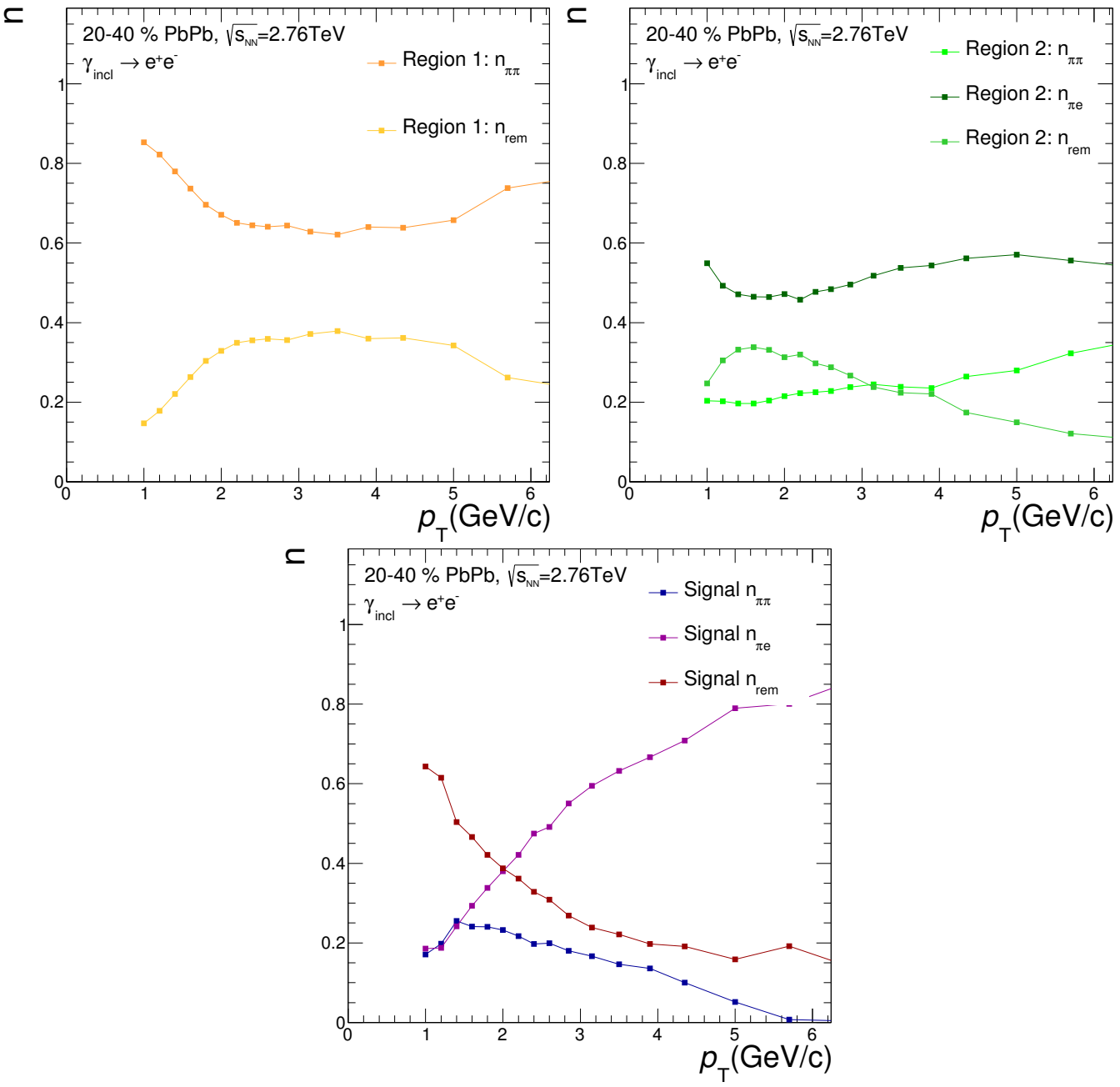

FIGURE 8.11: Relative contributions of the background source to the total background for region 1, region 2 and the signal region, obtained from MC template fits on data.

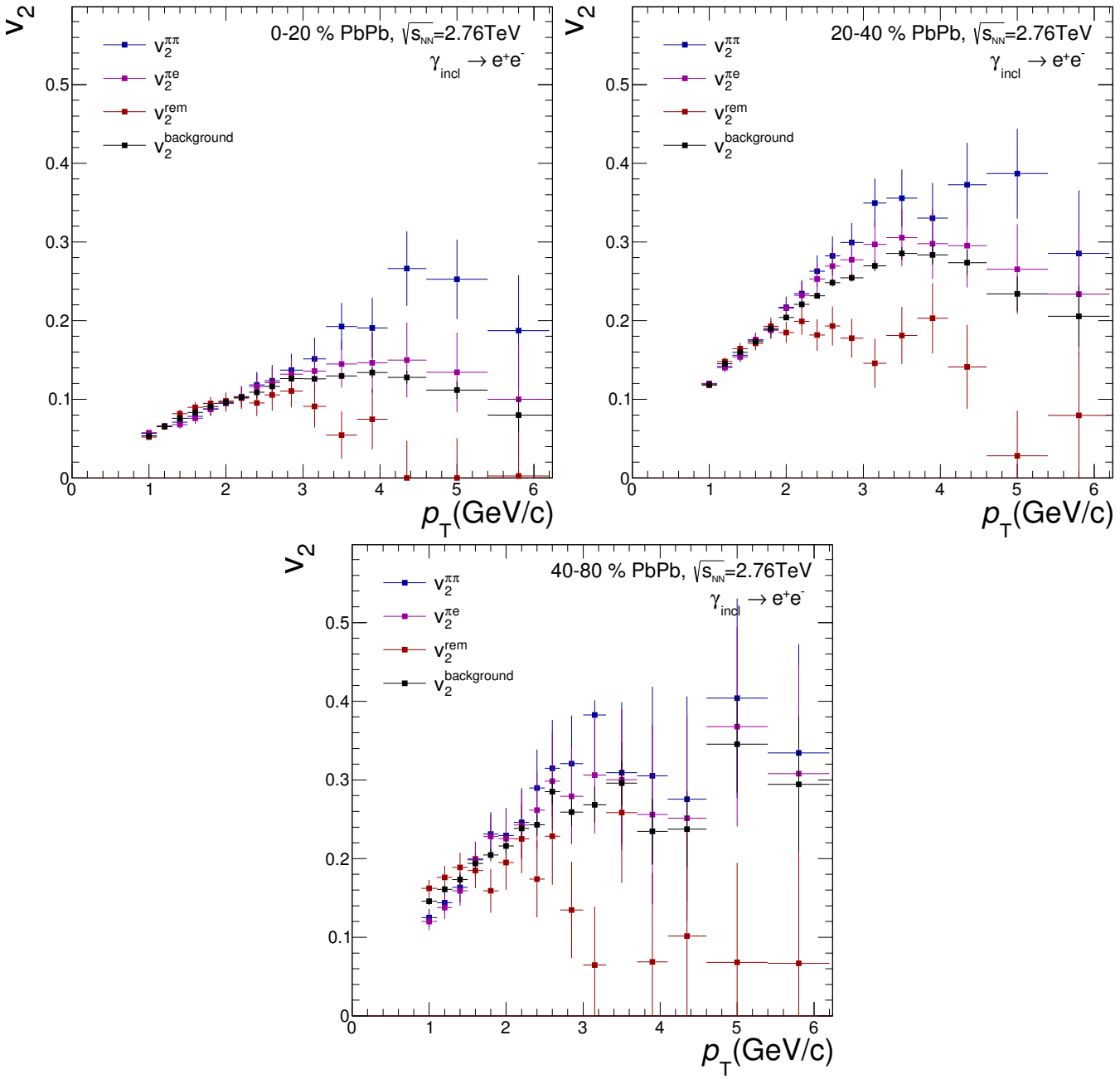

FIGURE 8.12: The v_2 of the different background sources with the resulting $v_2^{\gamma,\mathrm{bck}}$ in the signal region for the centrality classes $0-20\%$, $20-40\%$ and $40-80\%$.

8.4 Systematic uncertainty of inclusive photon flow

The conversion photon selection cuts are varied to study the effect on the inclusive photon flow. All variations are chosen such that a reasonable deviation is obtained. The variations are done one at a time with respect to the standard selection cuts. For each variation the following quantity is calculated:

$$\Delta(p_T) = \left(v_2^{\gamma,\mathrm{inc}}\right)_{modified}(p_\mathrm{T}) - \left(v_2^{\gamma,\mathrm{inc}}\right)_{standard}(p_\mathrm{T}) \tag{8.15}$$

Which quantifies the deviation from $v_2^{\gamma,\mathrm{inc}}$ with standard selection cuts for each p_T bin. If the photon selection cut is varied more than once, the assigned systematic is taken from the variation with the largest $\Delta(p_\mathrm{T})$. The total systematic error on $v_2^{\gamma,\mathrm{inc}}$ is assumed to be symmetrically distributed and is defined as:

$$\sigma_{syst}(p_\mathrm{T}) = \sqrt{\sum_i (\Delta_i(p_\mathrm{T}))^2} \tag{8.16}$$

With i representing all quantities that are varied. Table 8.1 shows the default cut values and the corresponding variations. The total systematic error and the different contributions are shown in figure 8.13 for the centrality classes $0-20\%$, $20-40\%$ and $40-80\%$. The systematic error increases for increasing p_T and is not very dependent on the centrality class. This is expected since the systematic error is not driven by the multiplicity of the event.

Quantity	**Standard**	**Cut variation 1**	**Cut variation 2**
$\lvert\eta\rvert$	< 0.9	< 0.75	
(R_{min}, R_{max})	$(5, 180)$ cm	$(5, 70)$ cm	$(10, 180)$ cm
min p_T	50 MeV/c	40 MeV/c	100 MeV/c
$q_{T,max}$	0.05 GeV/c	0.03 GeV/c	0.1 GeV/c
χ^2/ndf	< 30	< 20	< 50
Ψ_{pair}	< 0.1	< 0.05	< 0.2
$cos\,(\Theta_{P.A.})$	> 0.85	> 0.9	> 0.75

TABLE 8.1: Variations of the inclusive photon selection cuts to evaluate the systematic uncertainty of $v_2^{\gamma,\mathrm{inc}}$.

The background corrected inclusive photon flow using the standard photon selection cuts(table 8.1) for the centrality classes $0-20\%$, $20-40\%$ and $40-80\%$ is shown in figure 8.14. The statistical and systematic error are added in quadrature to calculate the total uncertainty on $v_2^{\gamma,\mathrm{inc}}$, which will be used for the non-Gaussian error propagation of $v_2^{\gamma,\mathrm{dir}}$.

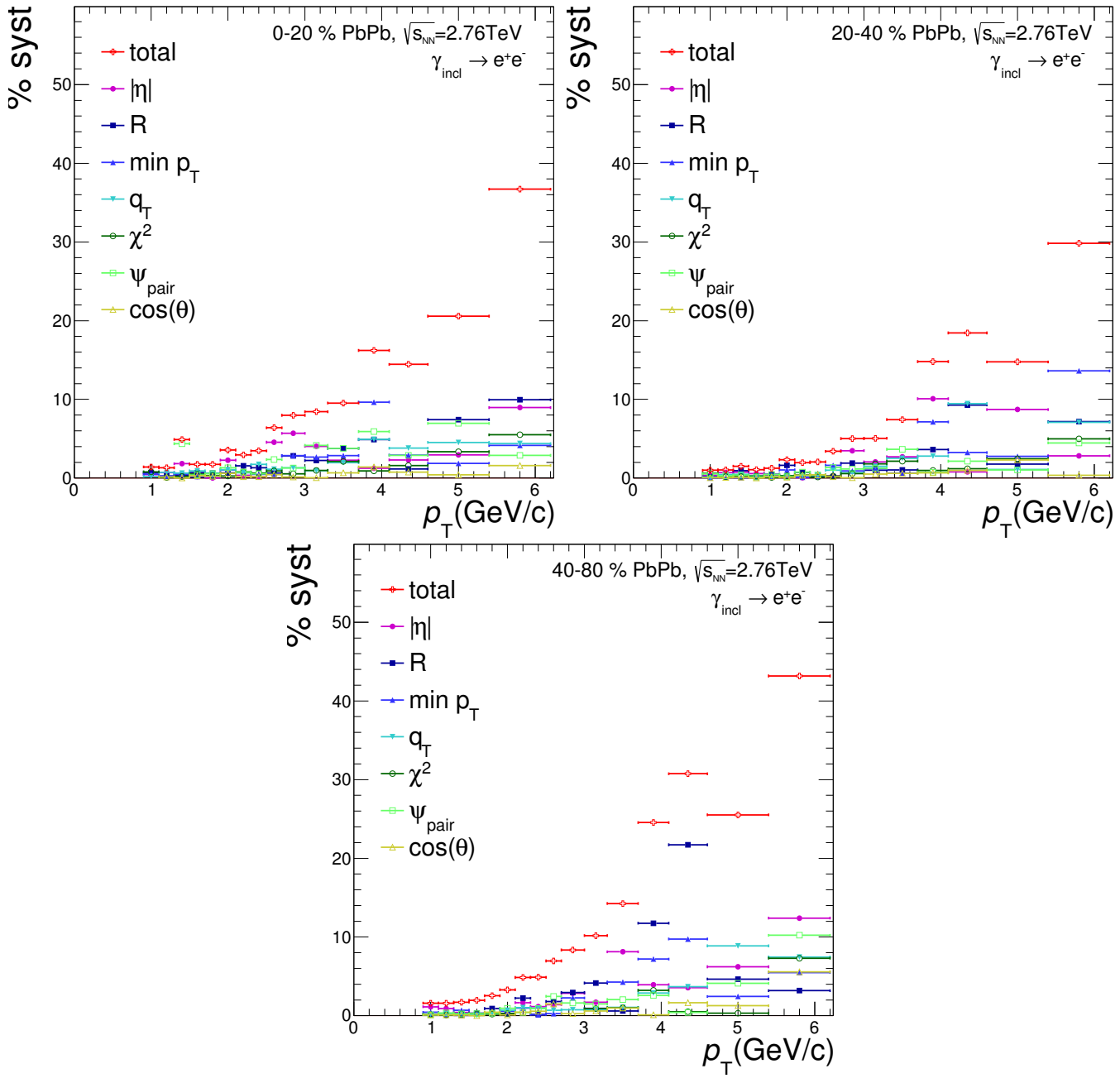

FIGURE 8.13: The total systematic error and the different contributions for the centrality classes $0-20\%$, $20-40\%$ and $40-80\%$, expressed in relative %.

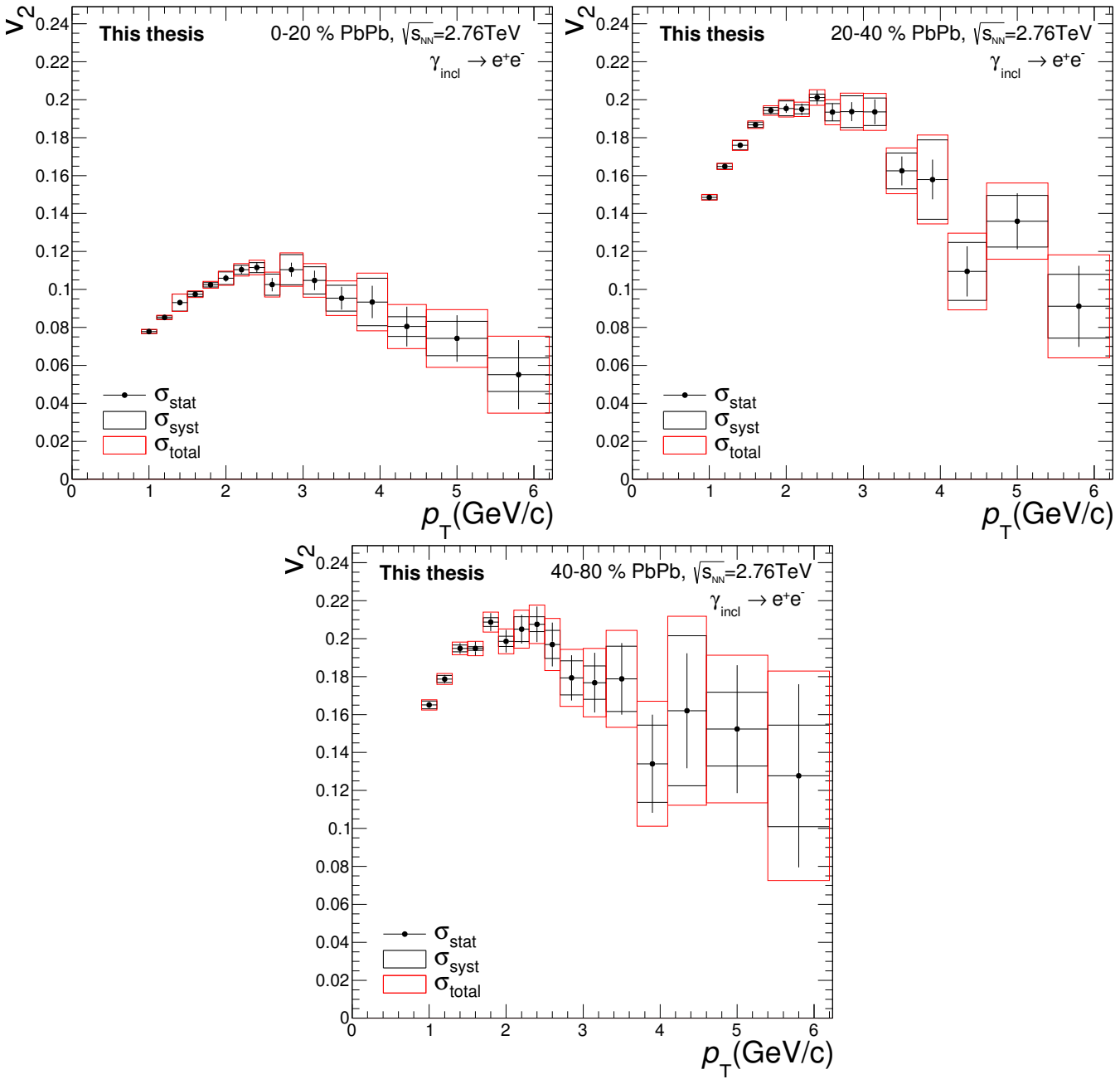

FIGURE 8.14: The background corrected inclusive photon flow for the centrality classes $0-20\%$, $20-40\%$ and $40-80\%$.

8.5 Decay photon flow

Inclusive photons are the sum of direct and decay photons. The direct photon yield is thus defined by the difference in inclusive and decay photon yields. A similar relation holds for the elliptic flow of direct photons, which means the decay photon flow needs to be calculated.
Both the yield and flow of decay photons are quantified by a "photon cocktail", which is based on simulations. In this cocktail all particles that decay into photons and that have a significant contribution to the total decay photon yield are included. A meson or baryon can be excluded if the branching ratio into photons is too small, the abundance is too low or a combination of both.
The biggest contribution to decay photons comes from the neutral pion decay: $\pi^0 \rightarrow \gamma\gamma$, which is the majority of all decay photons. In addition, there are contributions from other mesons and baryons; η, ρ, ω, η', ϕ and Σ^0. The masses, relevant decay channels and the ratios to charged pions of these particles are shown in table 8.2.

particle	**mass(MeV/c)**	**relevant decay channel**	**ratio**
π^0	134.98	$\pi^0 \rightarrow \gamma\gamma$ (BR= 98.798%)	$\pi^0/\pi = 1.0$
η	547.3	$\eta \rightarrow \gamma\gamma$ (BR= 39.43%)	$\eta/\pi = 0.46$
ρ	770.0	$\rho \rightarrow \pi^+\pi^-\gamma$ (BR= $9.9 \cdot 10^{-3}$)	$\rho/\pi = 1.0$
ω	781.9	$\omega \rightarrow \pi^0\gamma$ (BR= 8.92%)	$\omega/\pi = 0.9$
η'	957.8	η'$\rightarrow \rho\gamma$ (BR= 29.5%)	η'$/\pi = 0.25$
ϕ	1019.5	$\phi \rightarrow \eta\gamma$ (BR= 1.295%)	$\phi/\pi = 0.35$
Σ^0	1192.6	$\Sigma^0 \rightarrow \Lambda\gamma$ (BR= 100%)	$\Sigma^0/\pi = 0.49$

TABLE 8.2

Events are generated that include the π^0, η, K^0_S and ω. The K^0_S is included because it is subtracted from the direct photon spectrum. The transverse momentum dependent particle production is weighted using parametrizations of the invariant yields such that the relative abundancies are correct. The invariant yields are either measured independently or are obtained from m_T scaling. Furthermore, it has been shown that neutral and charged pions are similar in invariant yield, so either can be parametrized. m_T scaling assumes:

$$\frac{Y^1(m_T)}{Y^2(m_T)} = \text{constant.} \tag{8.17}$$

In the m_T scaling picture, the transverse component comes from particle production mechanisms which are equal up to a constant for all particles at the same transverse mass. This follows from the fact that the longitudinal components are present from the collision itself and that the transverse components have to be generated. Rewriting the formula as function of p_T for hadron h scaled from the π^0 gives:

$$Y^h(p_T) = A_{h/\pi^0} Y^{\pi^0}\left(\sqrt{p_T^2 + m_h^2 - m_{\pi^0}^2}\right). \tag{8.18}$$

Where $Y^h(p_T)$ is the invariant yield of the hadron, A_{h/π^0} the hadron to π^0 ratio and Y^{π^0} the invariant yield of the π^0. Neglecting the mass difference of neutral and charged pions, one can use $Y^{\pi^\pm}(p_T) = Y^{\pi^0}(p_T)$.

In parallel to the invariant yield, the elliptic flow coefficients of the cocktail particles are also included. In a similar way, the v_2 is parametrized by using either the measured v_2 or the KE_T scaled from the measured charged pion v_2 . KE_T scaling assumes:

$$\frac{v_n^1(\mathrm{KE}_T)}{v_n^2(\mathrm{KE}_T)} = \text{constant}, \tag{8.19}$$

using the same reasoning as for m_T scaling. Rewriting the formula as function of p_T for hadron h scaled from the π gives:

$$v_n^h(p_T) = v_n^\pi\left(\sqrt{(\mathrm{KE}_T^h + m_\pi)^2 - m_\pi^2}\right), \tag{8.20}$$

with:

$$\mathrm{KE}_T = \sqrt{p_T^2 + m^2} - m. \tag{8.21}$$

The v_2 of the cocktail particle translates into a dependence in the azimuthal angle φ.

Next, Pythia6 is used as a decayer to decay the hadrons according to their decay channels with the respective branching ratios. This completes the event generation. The decay photon yield can now be extracted. Also $v_2^{\gamma,\mathrm{dec}}$ can be calculated from the φ dependence of decay photons. The results are shown in figure 8.15 and figure 8.16.

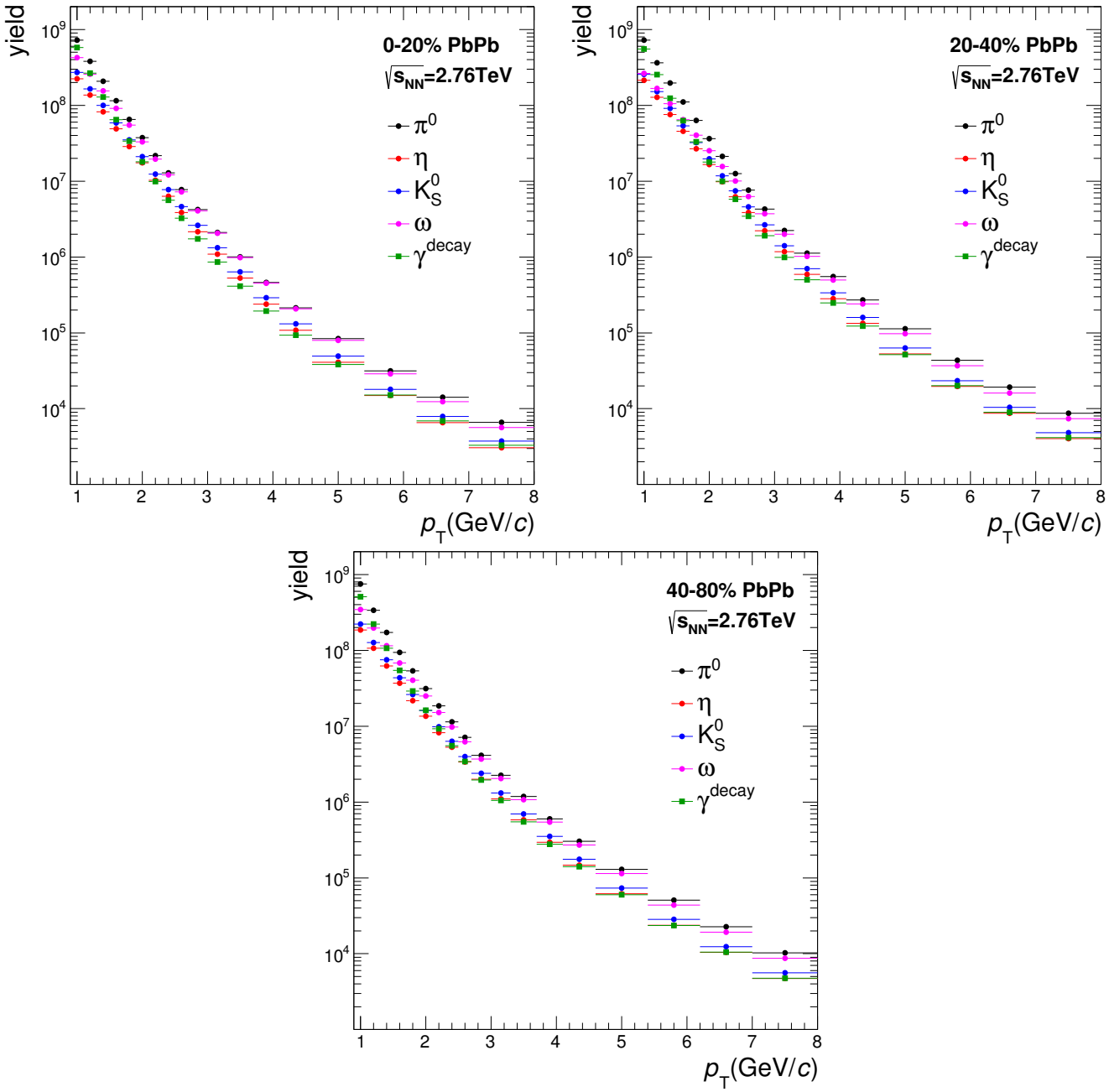

FIGURE 8.15: The invariant yields of the various photon cocktail ingredients with the yield of γ^{decay} for the centrality classes $0-20\%$, $20-40\%$ and $40-80\%$.

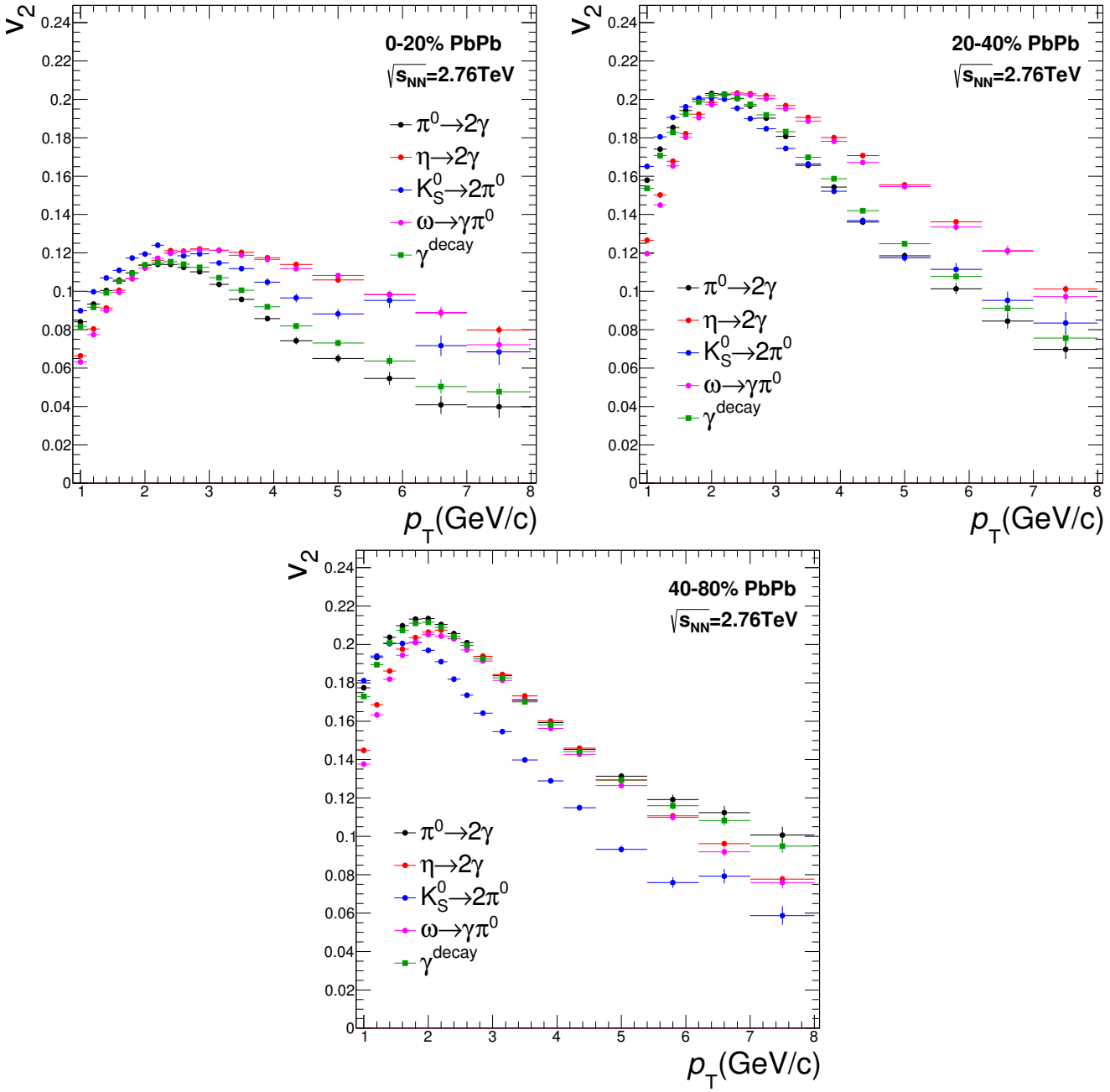

FIGURE 8.16: The v_2 of the various photon cocktail ingredients with the $v_2^{\gamma,\mathrm{dec}}$ for the centrality classes $0-20\%$, $20-40\%$ and $40-80\%$.

8.6 Results

The inclusive photons are selected using the photon conversion method with the default selection criteria in table 8.1. $v_2^{\gamma,\mathrm{inc}}$ is measured using the scalar product method, as described in section . Furthermore, $v_2^{\gamma,\mathrm{inc}}$ is corrected by the background flow as described in section 8.1. Figure 8.17 shows the result for $v_2^{\gamma,\mathrm{inc}}$ and $v_2^{\gamma,\mathrm{dec}}$ for the centrality classes $0-20\%$, $20-40\%$ and $40-80\%$. As expected, the elliptic flow increases for semi-central collisions compared to central collisions. The error on $v_2^{\gamma,\mathrm{inc}}$ is the total error ($\sigma_{total} = \sqrt{\sigma_{stat}^2 + \sigma_{syst}^2}$). The background flow corrected $v_2^{\gamma,\mathrm{inc}}$ and $v_2^{\gamma,\mathrm{dec}}$ will be used for calculating the direct photon flow coefficient $v_2^{\gamma,\mathrm{dir}}$.

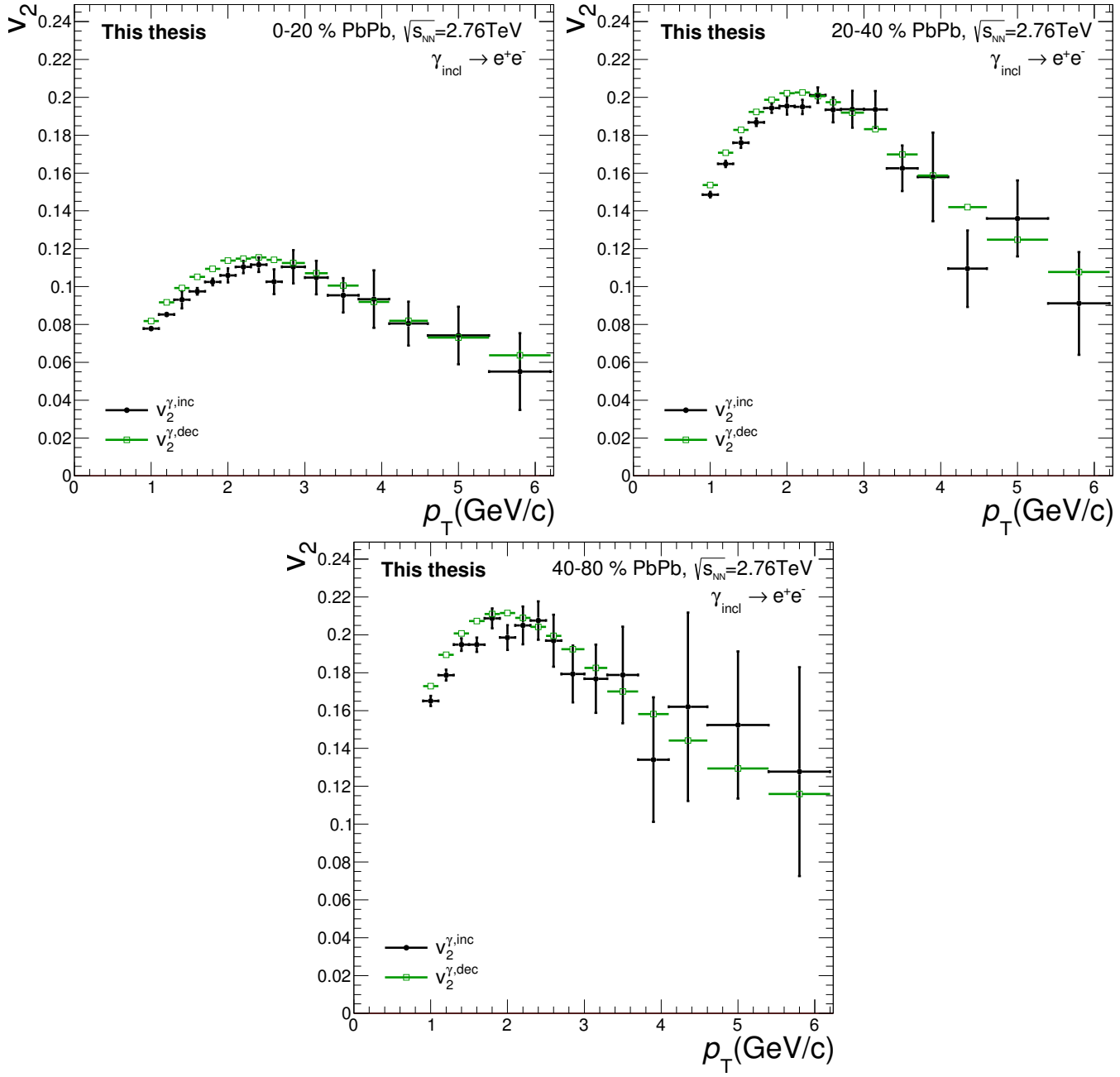

FIGURE 8.17: $v_2^{\gamma,\mathrm{inc}}$ and $v_2^{\gamma,\mathrm{dec}}$ for the centrality classes $0-20\%$, $20-40\%$ and $40-80\%$

Chapter 9

Direct photon flow

The inclusive photon sample consists out of decay and direct photons. The inclusive photon flow is therefore a combination of decay and direct photons flow. $v_2^{\gamma,\mathrm{dir}}$ is calculated by subtracting $v_2^{\gamma,\mathrm{dec}}$ from $v_2^{\gamma,\mathrm{inc}}$ using the excess of direct photons over the decay photons:

$$v_2^{\gamma,\mathrm{dir}}\ (p_\mathrm{T}\ ) = \frac{R_\gamma\ (p_\mathrm{T}\ ) v_2^{\gamma,\mathrm{inc}}\ (p_\mathrm{T}\ ) - v_2^{\gamma,\mathrm{dec}}\ (p_\mathrm{T}\ )}{R_\gamma\ (p_\mathrm{T}\ ) - 1}. \tag{9.1}$$

Recently, R_γ has been measured by PCM and PHOS for PbPb collisions at $\sqrt{s_{NN}}$ = 2.76TeV in the centralities $0-20\%$, $20-40\%$ and $40-80\%$. This analysis uses the R_γ from PCM and PHOS combined, as shown in figure 9.1.

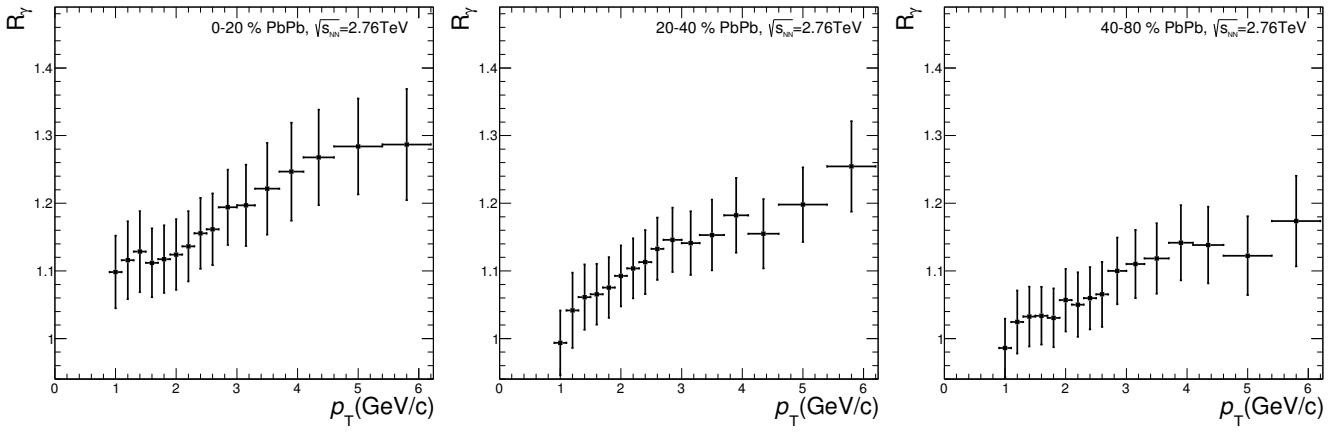

FIGURE 9.1: PCM and PHOS combined R_γ for the centrality classes $0-20\%$, $20-40\%$ and $40-80\%$.

9.1 Error propagation

The direct photon flow coefficient $v_2^{\gamma,\mathrm{dir}}$ is calculated by using the transverse momentum dependent quantities $v_2^{\gamma,\mathrm{inc}}$, $v_2^{\gamma,\mathrm{dec}}$ and R_γ . These quantities have Gaussian statistical and systematic uncertainties around

a central value for each momentum bin, except R_γ when $R_\gamma \approx 1$. However, the uncertainty in $v_2^{\gamma,\mathrm{dir}}$ is not Gaussian around its central value. This is because the double ratio R_γ assumes values such that $R_\gamma - 1 \sim 0$. Two approaches to calculate the uncertainty of $v_2^{\gamma,\mathrm{dir}}$ have been studied.

9.1.1 Gaussian error propagation

In first approximation, the uncertainty on $v_2^{\gamma,\mathrm{dir}}$ can be assumed to be Gaussian without any correlation between the variables $v_2^{\gamma,\mathrm{inc}}$, $v_2^{\gamma,\mathrm{dec}}$ and R_γ. In this case the uncertainty on $v_2^{\gamma,\mathrm{dir}}$ is calculated by

$$\sigma_{v_2^{\gamma,\mathrm{dir}}} = \sqrt{\left(\frac{\partial v_2^{\gamma,\mathrm{dir}}}{\partial v_2^{\gamma,\mathrm{inc}}}\right)^2 \left(\sigma_{v_2^{\gamma,\mathrm{inc}}}\right)^2 + \left(\frac{\partial v_2^{\gamma,\mathrm{dir}}}{\partial R_\gamma}\right)^2 \left(\sigma_{R_\gamma}\right)^2 + \left(\frac{\partial v_2^{\gamma,\mathrm{dir}}}{\partial v_2^{\gamma,\mathrm{dec}}}\right)^2 \left(\sigma_{v_2^{\gamma,\mathrm{dec}}}\right)^2} \tag{9.2}$$

with

$$\left(\frac{\partial v_2^{\gamma,\mathrm{dir}}}{\partial v_2^{\gamma,\mathrm{inc}}}\right) = \frac{R_\gamma}{R_\gamma - 1}, \left(\frac{\partial v_2^{\gamma,\mathrm{dir}}}{\partial R_\gamma}\right) = \frac{v_2^{\gamma,\mathrm{dec}} - v_2^{\gamma,\mathrm{inc}}}{(R_\gamma - 1)^2}, \left(\frac{\partial v_2^{\gamma,\mathrm{dir}}}{\partial v_2^{\gamma,\mathrm{dec}}}\right) = \frac{1}{1 - R_\gamma}. \tag{9.3}$$

However, Gaussian error propagation is not valid for R_γ values close to unity. This approximation will only be used as comparison to the non-Gaussian error propagation approach.

9.1.2 Non-Gaussian error propagation

Non-Gaussian error propagation is done by performing pseudo-experiments. In the pseudo-experiment, $v_2^{\gamma,\mathrm{inc}}$ is recalculated $N = 10^6$ times for slightly changed values of $v_2^{\gamma,\mathrm{inc}}$, $v_2^{\gamma,\mathrm{dec}}$ and R_γ. The randomised values are calculated as follows:

$$\left(v_2^{\gamma,\mathrm{inc}}\right)_{rand} = v_2^{\gamma,\mathrm{inc}} + R\left(\sigma_{v_2^{\gamma,\mathrm{inc}}}\right) \tag{9.4}$$

$$\left(v_2^{\gamma,\mathrm{dec}}\right)_{rand} = v_2^{\gamma,\mathrm{dec}} + R\left(\sigma_{v_2^{\gamma,\mathrm{dec}}}\right) \tag{9.5}$$

$$\left(R_\gamma\right)_{rand} = R_\gamma + R\left(\sigma_{R_\gamma}\right) \tag{9.6}$$

where $R(\sigma_x)$ is a random number generated from a Gaussian with $\mu = 0$ and standard deviation $\sigma = \sigma_x$. Figure 9.2 shows the $v_2^{\gamma,\mathrm{inc}}$, $v_2^{\gamma,\mathrm{dec}}$ and R_γ distributions for one transverse momentum bin that is used for the non-Gaussian error propagation. R_γ has been restricted to values greater than unity, and leads to a Gaussian cut off for some transverse momentum bins. This has been chosen to reflect the knowledge that R_γ must be greater or equal to unity, even if the measurement R_γ via the double ratio can fluctuate below unity.

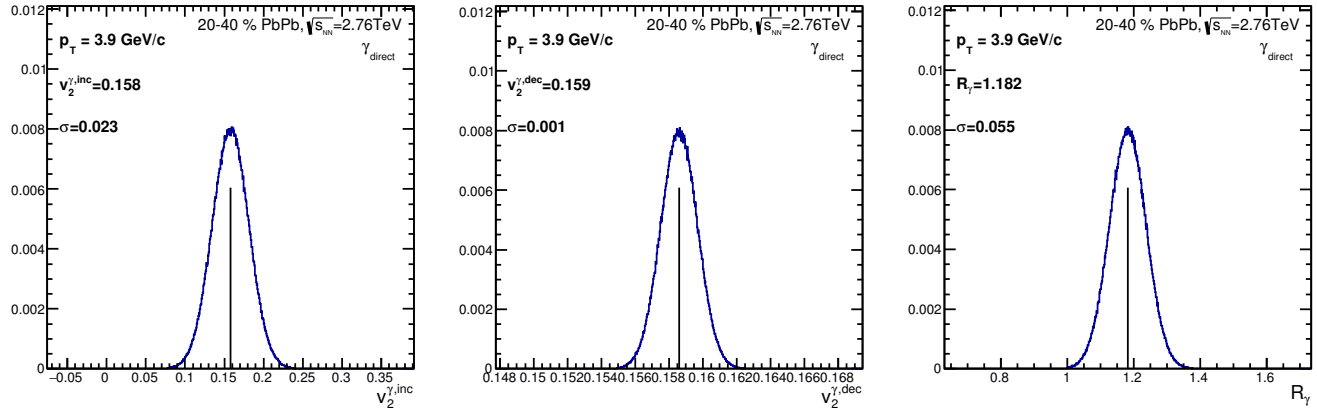

FIGURE 9.2: Distributions for $v_2^{\gamma,\mathrm{inc}}$, $v_2^{\gamma,\mathrm{dec}}$ and R_γ for one transverse momentum bin.

The collection of recalculated $v_2^{\gamma,\mathrm{dir}}$ values form a distribution from which the mean, median, lower and upper confidence intervals can be obtained. The normalized distribution of $v_2^{\gamma,\mathrm{dir}}$ values is integrated iteratively to calculate the following values:

- central value : $\int_{-\infty}^{x} pdf(v_2)dv_2 = 0.5$
- lower confidence interval : $\int_{-\infty}^{a} pdf(v_2)dv_2 = 0.15865$
- upper confidence interval : $\int_{-\infty}^{b} pdf(v_2)dv_2 = 0.84135$

The resulting distributions of $v_2^{\gamma,\mathrm{dir}}$ values for three transverse momentum bins1.6 GeV/c and 3.9 GeV/c are shown in figure 9.3. The dashed lines indicate the central value and the lower and upper confidence intervals when assuming Gaussian error propagation. The red solid line indicates the median and the lower and upper confidence intervals which will be used as central value and lower and upper error of the $v_2^{\gamma,\mathrm{dir}}$ measurement. It can be seen that for some p_T bins the distribution of $v_2^{\gamma,\mathrm{dir}}$ values is approximately Gaussian, while for others it is clearly non-Gaussian and the error becomes asymmetric. Therefore, the non-Gaussian error propagation approach, using pseudo-experiments, is used to obtain the error on $v_2^{\gamma,\mathrm{dir}}$ for all p_T bins and all centrality classes. In addition, the total error ($\sigma_{total} = \sqrt{\sigma_{stat}^2 + \sigma_{syst}^2}$) on $v_2^{\gamma,\mathrm{inc}}$, $v_2^{\gamma,\mathrm{dec}}$ and R_γ is used for the propagation, such that a single well defined total error is obtained for $v_2^{\gamma,\mathrm{dir}}$.

9.2 Direct photon flow results

The direct photon flow coefficient $v_2^{\gamma,\mathrm{dir}}$ has been measured using the photon conversion method for Pb-Pb collisions at $\sqrt{s_{NN}}$ = 2.76TeV in the centralities $0-20\%$, $20-40\%$ and $40-80\%$. The results are shown in figure 9.4, 9.5 and 9.6. It uses the background corrected inclusive photon flow, the combined PCM and PHOS R_γ result and the decay photon flow extracted from a photon cocktail. The uncertainty on the measured $v_2^{\gamma,\mathrm{dir}}$ is obtained by performing pseudo-experiments where all statistical and systematic

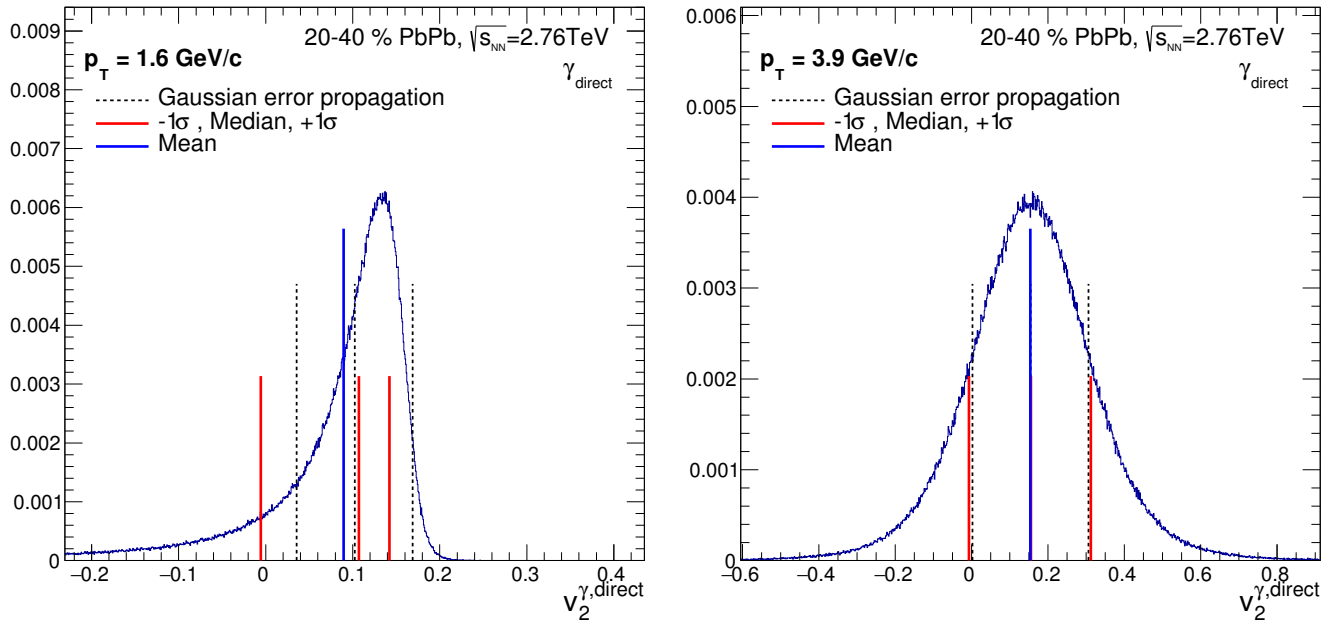

FIGURE 9.3: Distribution of $v_2^{\gamma,\mathrm{dir}}$ values, propagated with pseudo-experiments, for three transverse momentum bins(1.2 GeV/c, 1.6 GeV/c and 3.9 GeV/c).

uncertainties on $v_2^{\gamma,\mathrm{inc}}$, R_γ and $v_2^{\gamma,\mathrm{dec}}$ are combined into a total error for the propagation. The result for centrality $0-20\%$ shows to be slightly above zero with no clear transverse momentum dependence. In the $20-40\%$ centrality class the direct photon flow has an increasing v_2 for $1.0\mathrm{GeV/c} < p_T < 3.0\mathrm{GeV/c}$ and possibly goes down for higher transverse momentum. The measurement for $40-80\%$ centrality is heavily dominated by the statistical and systematic errors of $v_2^{\gamma,\mathrm{inc}}$, R_γ and $v_2^{\gamma,\mathrm{dec}}$ and is therefore easily consistent with zero.

9.3 Outlook

The inclusive, decay and direct photon flow results presented in this thesis are not fully finalized because it is possible to do a few additional checks. It is not expected that this can lead to significantly different $v_2^{\gamma,\mathrm{dir}}$, although it is important to aim for the best possible measurement.

For the inclusive photon flow the effect from electron-positron combinatorics is currently assumed to be negligible, as they contaminate the inclusive photon sample for less than 2%. However, since the v_2 of this background source can be significantly different from $v_2^{\gamma,\mathrm{inc}}$, the correction to $v_2^{\gamma,\mathrm{inc}}$ can be of the order of a few %. One way of investigating the contamination is by isolating the background source using a combination of photon selection variables, like Ψ_{pair} and q_T. First attempts to isolate this background have been made but were unsuccessful.
In addition, a more detailed evaluation of the $v_2^{\gamma,\mathrm{inc}}$ error fluctuations can be done. With this information the errors are better understood and can be smoothed out further.

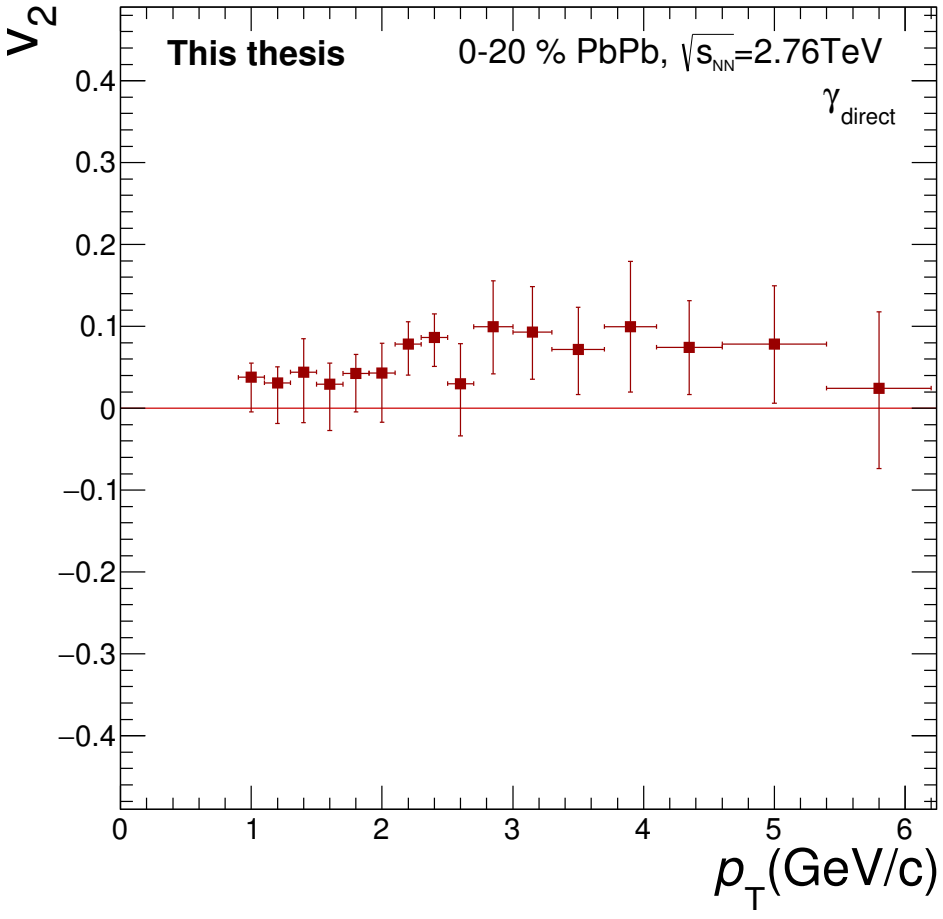

FIGURE 9.4: The direct photon flow coefficient $v_2^{\gamma,\mathrm{dir}}$ measured with the photon conversion method for Pb-Pb collisions at $\sqrt{s_{NN}}$ = 2.76TeV in the centrality class $0-20\%$.

The decay photon flow is currently estimated by a photon cocktail simulation using the π^0, η and ω. Additional particles, like the ρ, η', ϕ and Σ^0 can be added to increase the precision of $v_2^{\gamma,\mathrm{dec}}$. Most of these particles do not have their spectrum or flow measured and need to be scaled from the charged pion results.

The results for $v_2^{\gamma,\mathrm{dir}}$ are directly affected by any change in the inclusive and decay photon result. Another important check is the purity estimate used in the calculation of the R_γ measurement. The purity study presented in this thesis, using the fits of MC templates on data, revealed that the purity is a few % smaller than the MC result. This could also affect the R_γ measurement by a few %, and change the result for $v_2^{\gamma,\mathrm{dir}}$ accordingly.
It is expected that $v_2^{\gamma,\mathrm{dir}}$ is correct within its uncertainty but it remains important to put it through a lot of scrutiny because the measurement is sensitive to small effects. If the $v_2^{\gamma,\mathrm{dir}}$ measurement is proven to be solid it is straightforward to measure the triangular flow coefficient $v_3^{\gamma,dir}$, adding more constraints to theoretical models.

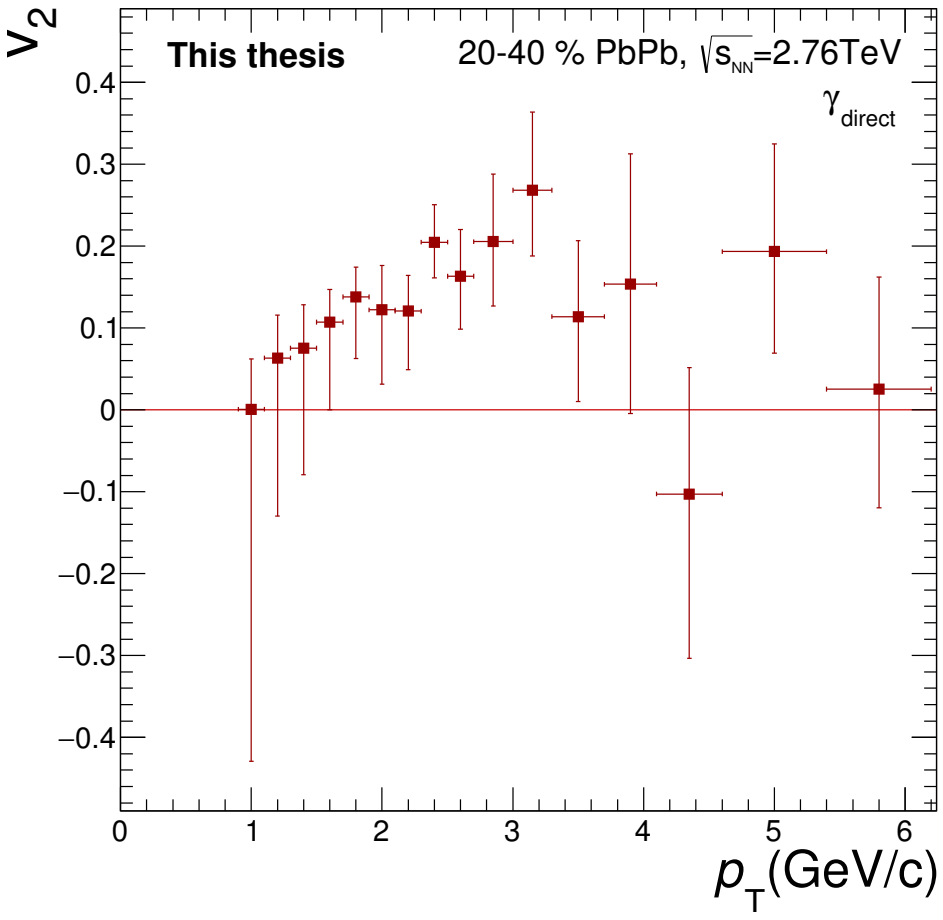

FIGURE 9.5: The direct photon flow coefficient $v_2^{\gamma,\mathrm{dir}}$ measured with the photon conversion method for Pb-Pb collisions at $\sqrt{s_{NN}} = 2.76$TeV in the centrality class $20-40\%$.

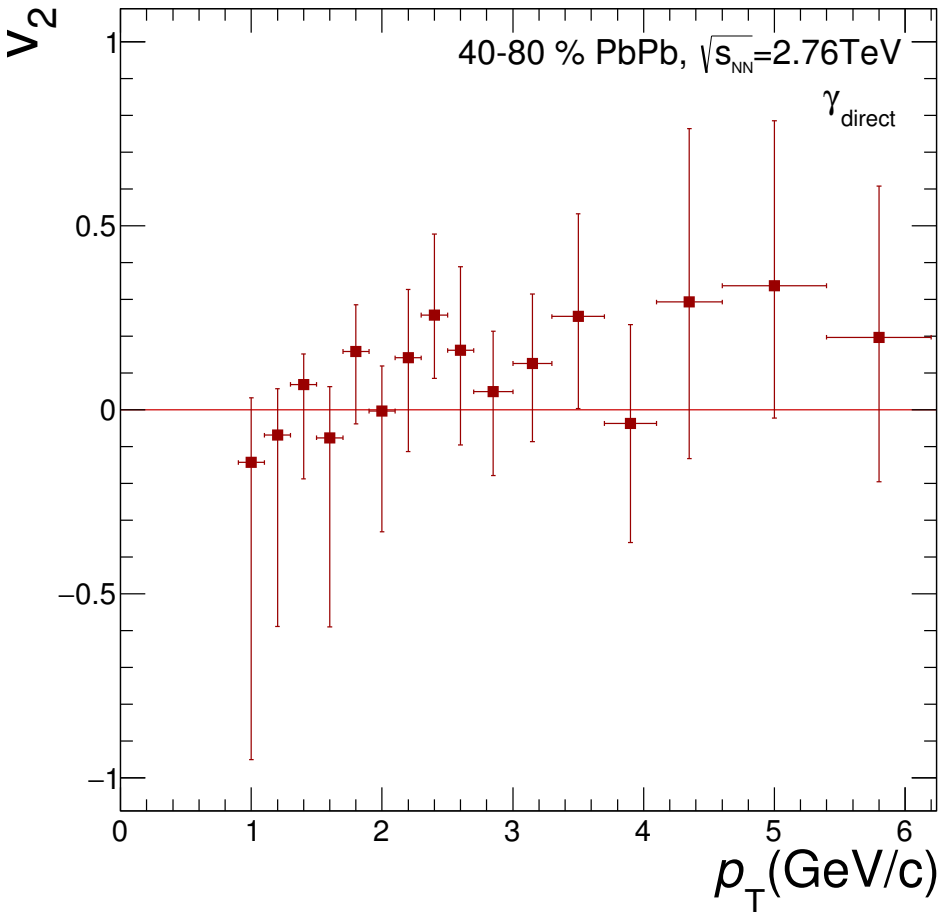

FIGURE 9.6: The direct photon flow coefficient $v_2^{\gamma,\mathrm{dir}}$ measured with the photon conversion method for Pb-Pb collisions at $\sqrt{s_{NN}}$ = 2.76TeV in the centrality class $40-80\%$.

Appendix A

Neutral meson systematic variations

	π^0	η
Normalization window		
Right side [GeV/c^2]	(0.19, 0.3)	(0.65, 0.75)
Left side [GeV/c^2]	(0.03, 0.05)	(0.35, 0.42)
Integration range		
standard [GeV/c^2]	$(M_{\pi^0} - 0.032,\ M_{\pi^0} + 0.022)$	$(M_\eta - 0.060,\ M_\eta + 0.050)$
narrow [GeV/c^2]	$(M_{\pi^0} - 0.016,\ M_{\pi^0} + 0.016)$	$(M_\eta - 0.040,\ M_\eta + 0.030)$
wide [GeV/c^2]	$(M_{\pi^0} - 0.048,\ M_{\pi^0} + 0.028)$	$(M_\eta - 0.080,\ M_\eta + 0.060)$

TABLE A.1: Variations of the integration and normalization windows for the estimate of the systematic error from the signal extraction.

Quantity	Standard	Cut variation 1	Cut variation 2	Cut variation 3
Material	full EMCal	TRD	no TRD	
Energy corrections	Conv-Calo mass fit	Calo mass fit	Conv-Calo test beam fit	Calo test beam fit
Cell timing $\lvert t_{cell}\rvert$	$<$ 500ns	$<$ 100ns	$<$ 200ns	
Trackmatching	TM1*	OFF	TM5*	
min $E_{\mathbf{clus}}$	0.7 GeV/c	0.6 GeV/c	0.8 GeV/c	0.9 GeV/c
min $N_{\mathbf{cells}}$	2	1		
M_{02}	$0.10 < M_{02} < 0.50$	$0 < M_{02} < 0.50$	$0.10 < M_{02} < 100$	
opening angle $\theta_{\gamma\gamma}$	$>$ 2.02 mrad (1 cell diagonal)	$>$ 1.52 mrad (0.75 cell diagonal)	$>$ 4.04 mrad (2 cell diagonal)	
$\lvert y\rvert$ **meson**	$<$ 0.5	$<$ 0.6	$<$ 0.8	

TABLE A.2: Variations for the systematic error evaluation are listed in this table. The column with the title "Standard" reflects the standard cut for each cut respectively, while the columns titled with "Cut variation" show the variations, which were done for the respective cut (row). Only one cut is varied at a time to estimate the systematic error.

Bibliography

[1] Tanmoy Bhattacharya et al. QCD phase transition with chiral quarks and physical quark masses. *Phys. Rev. Lett.*, 113(8):082001, 2014. doi: 10.1103/PhysRevLett.113.082001.

[2] Joseph I. Kapusta, P. Lichard, and D. Seibert. High-energy photons from quark-gluon plasma versus hot hadronic gas. *Phys. Rev.*, D44:2774–2788, 1991. doi: 10.1103/PhysRevD.47.4171,10.1103/PhysRevD.44.2774. [Erratum: Phys. Rev.D47,4171(1993)].

[3] M. M. Aggarwal et al. Observation of direct photons in central 158A GeV PbPb collisions. *Phys. Rev. Lett.*, 85:3595–3599, 2000. doi: 10.1103/PhysRevLett.85.3595.

[4] A. Adare et al. Enhanced production of direct photons in AuAu collisions at $\sqrt{s_{NN}} = 200$ GeV and implications for the initial temperature. *Phys. Rev. Lett.*, 104:132301, 2010. doi: 10.1103/PhysRevLett.104.132301.

[5] A. Adare et al. Detailed measurement of the e^+e^- pair continuum in pp and AuAu collisions at $\sqrt{s_{NN}} = 200$ GeV and implications for direct photon production. *Phys. Rev.*, C81:034911, 2010. doi: 10.1103/PhysRevC.81.034911.

[6] A. Adare et al. Centrality dependence of low-momentum direct-photon production in AuAu collisions at $\sqrt{s_{NN}} = 200$ GeV. *Phys. Rev.*, C91(6):064904, 2015. doi: 10.1103/PhysRevC.91.064904.

[7] STAR Collaboration. Direct virtual photon production in Au+Au collisions at $\sqrt{s_{NN}} = 200$ GeV.

[8] Jaroslav Adam et al. Direct photon production in PbPb collisions at $\sqrt{s_{NN}} = 2.76$ TeV. *Phys. Lett.*, B754:235–248, 2016. doi: 10.1016/j.physletb.2016.01.020.

[9] A. Adare et al. Observation of direct-photon collective flow in $\sqrt{s_{NN}} = 200$ GeV AuAu collisions. *Phys. Rev. Lett.*, 109:122302, 2012. doi: 10.1103/PhysRevLett.109.122302.

[10] A. Adare et al. Azimuthally anisotropic emission of low-momentum direct photons in AuAu collisions at $\sqrt{s_{NN}} = 200$ GeV. 2015.

[11] Daniel Lohner (for the ALICE collaboration). Measurement of direct-photon elliptic flow in PbPb collisions at $\sqrt{s_{NN}} = 2.76$ TeV. *J. Phys. Conf. Ser.*, 446:012028, 2013. doi: 10.1088/1742-6596/446/1/012028.

[12] Chun Shen, Ulrich W Heinz, Jean-Francois Paquet, and Charles Gale. Thermal photons as a quark-gluon plasma thermometer reexamined. *Phys. Rev.*, C89(4):044910, 2014. doi: 10.1103/PhysRevC.89.044910.

[13] Chun Shen, Ulrich W. Heinz, Jean-Francois Paquet, Igor Kozlov, and Charles Gale. Anisotropic flow of thermal photons as a quark-gluon plasma viscometer. *Phys. Rev.*, C91(2):024908, 2015. doi: 10.1103/PhysRevC.91.024908.

[14] Rupa Chatterjee, Hannu Holopainen, Ilkka Helenius, Thorsten Renk, and Kari J. Eskola. Elliptic flow of thermal photons from event-by-event hydrodynamic model. *Phys. Rev.*, C88:034901, 2013. doi: 10.1103/PhysRevC.88.034901.

[15] O. Linnyk, W. Cassing, and E. L. Bratkovskaya. Centrality dependence of the direct photon yield and elliptic flow in heavy-ion collisions at $\sqrt{s_{NN}} = 200$ GeV. *Phys. Rev.*, C89(3):034908, 2014. doi: 10.1103/PhysRevC.89.034908.

[16] Hendrik van Hees, Min He, and Ralf Rapp. Pseudo-critical enhancement of thermal photons in relativistic heavy-ion collisions? *Nucl. Phys.*, A933:256–271, 2015. doi: 10.1016/j.nuclphysa.2014.09.009.

[17] Akihiko Monnai. Thermal photon v_2 with slow quark chemical equilibration. *Phys. Rev.*, C90(2):021901, 2014. doi: 10.1103/PhysRevC.90.021901.

[18] Larry McLerran and Bjoern Schenke. The Glasma, Photons and the Implications of Anisotropy. *Nucl. Phys.*, A929:71–82, 2014. doi: 10.1016/j.nuclphysa.2014.06.004.

[19] Sarah Campbell. Photon production from gluon-mediated quarkanti-quark annihilation at confinement. *Phys. Rev.*, C92(1):014907, 2015. doi: 10.1103/PhysRevC.92.014907.

[20] Larry McLerran and Bjrn Schenke. A Tale of tails: Photon rates and flow in ultra-relativistic heavy ion collisions. *Nucl. Phys.*, A946:158–170, 2016. doi: 10.1016/j.nuclphysa.2015.11.008.

[21] Jean-Franois Paquet, Chun Shen, Gabriel S. Denicol, Matthew Luzum, Bjrn Schenke, Sangyong Jeon, and Charles Gale. Production of photons in relativistic heavy-ion collisions. *Phys. Rev.*, C93(4):044906, 2016. doi: 10.1103/PhysRevC.93.044906.

[22] Nathan P. M. Holt, Paul M. Hohler, and Ralf Rapp. Thermal photon emission from the system. *Nucl. Phys.*, A945:1–20, 2016. doi: 10.1016/j.nuclphysa.2015.09.008.

[23] V. Vovchenko, Iu. A. Karpenko, M. I. Gorenstein, L. M. Satarov, I. N. Mishustin, B. Kmpfer, and H. Stoecker. Electromagnetic probes of a pure-glue initial state in nucleus-nucleus collisions at LHC. 2016.

[24] F. Bock. *Neutral Pion and Eta Meson Production in pp and Pb–Pb Collisions at the LHC with the ALICE Detector*. PhD thesis, University Heidelberg, 2012. URL http://www.physi.uni-heidelberg.de//Publications/Bock-Masterthesis.pdf.

[25] Martin Wilde (for the ALICE collaboration). Measurement of Direct Photons in pp and Pb-Pb Collisions with ALICE. *Nucl. Phys.*, A904-905:573c–576c, 2013. doi: 10.1016/j.nuclphysa.2013.02.079.

[26] Daniel Lohner. *Anisotropic flow of direct photons in Pb-Pb collisions at 2.76 TeV per nucleon*. PhD thesis, Heidelberg U., 2013-09-16. URL http://inspirehep.net/record/1296412/files/245328385_CERN-THESIS-2013-158.pdf.

[27] Martin Wilde. *Measurement of Direct Photons in pp and PbPb Collisions with Conversion Pairs*. PhD thesis, Munster U., 2015. URL http://cds.cern.ch/record/2154827.

[28] Mikolaj Chojnacki, Adam Kisiel, Wojciech Florkowski, and Wojciech Broniowski. THERMINATOR 2: THERMal heavy IoN generATOR 2. *Comput. Phys. Commun.*, 183:746–773, 2012. doi: 10.1016/j.cpc.2011.11.018.

[29] Betty Bezverkhny Abelev et al. Elliptic flow of identified hadrons in PbPb collisions at $\sqrt{s_{NN}} = 2.76$ TeV. *JHEP*, 06:190, 2015. doi: 10.1007/JHEP06(2015)190.

[30] S. A. Voloshin. Anisotropic flow. *Nucl. Phys.*, A715:379–388, 2003. doi: 10.1016/S0375-9474(02)01450-1.

[31] Denes Molnar and Sergei A. Voloshin. Elliptic flow at large transverse momenta from quark coalescence. *Phys. Rev. Lett.*, 91:092301, 2003. doi: 10.1103/PhysRevLett.91.092301.